

Geological Fluid Mechanics Models at Various Scales

by

Martin Oliver Saar

M.S. (University of Oregon) 1998

A dissertation submitted in partial satisfaction
of the requirements for the degree of

Doctor of Philosophy

in

Earth and Planetary Science

in the

GRADUATE DIVISION

of the

UNIVERSITY OF CALIFORNIA, BERKELEY

Committee in charge:

Professor Michael Manga, Chair
Professor James Rector
Professor Steven Glaser

Fall 2003

The dissertation of Martin Oliver Saar is approved.

Chair

Date

Date

Date

University of California, Berkeley

Fall 2003

Geological Fluid Mechanics Models at Various Scales

Copyright © 2003

by

Martin Oliver Saar

Abstract

Geological Fluid Mechanics Models at Various Scales

by

Martin Oliver Saar

Doctor of Philosophy in Earth and Planetary Science

University of California, Berkeley

Professor Michael Manga, Chair

In this dissertation, I employ concepts from fluid mechanics to quantitatively investigate geological processes in hydrogeology and volcanology. These research topics are addressed by utilizing numerical and analytical models but also by conducting field and lab work.

Percolation theory is of interest to a wide range of physical sciences and thus warrants research in itself. Therefore, I developed a computer code to study percolation thresholds of soft-core polyhedra. Results from this research are applied to study the onset of yield strength in crystal-melt suspensions such as magmas. Implications of yield strength development in suspensions, marking the transition from Newtonian to Bingham fluid, include the pahoehoe-’a’a transition and the occurrence of effusive versus explosive eruptions.

I also study interactions between volcanic processes and groundwater as well as between groundwater and seismicity (hydroseismicity). In the former case, I develop numerical and analytical models of coupled groundwater and heat transfer. Here, per-

turbations from a linear temperature-depth profile are used to determine groundwater flow patterns and rates. For the hydroseismicity project I investigate if seasonal elevated levels of seismicity at Mt. Hood, Oregon, are triggered by groundwater recharge. Both hydroseismicity and hydrothermal springs occur on the southern flanks of Mt. Hood. This suggests that both phenomena are related while also providing a connection between the research projects involving groundwater, heat flow, and seismicity. Indeed, seismicity may be necessary to keep faults from clogging thus allowing for sustained activity of hydrothermal springs.

Finally, I present research on hydrologically induced volcanism, where a process similar to the one suggested for hydroseismicity is invoked. Here, melting of glaciers, or draining of lakes, during interglacial periods reduce the confining pressure in the subsurface which may promote dike formation and result in increased rates of volcanism.

In general, problems discussed in this dissertation involve interactions among processes that are traditionally associated with separate research disciplines. However, numerous problems in the geosciences require a multidisciplinary approach, as demonstrated here. In addition, employing several analytical and numerical methods, such as signal processing, inverse theory, computer modeling, and percolation theory, allows me to study such diverse processes in a quantitative way.

Professor Michael Manga
Dissertation Committee Chair

Contents

Contents	i
List of Figures	iv
List of Tables	vii
1 Introduction	1
2 Continuum percolation theory	5
2.1 Introduction	5
2.2 Method	8
2.3 Average number of bonds per object, B_c	11
2.4 Normalized average excluded volume, $\langle \overline{v_{ex}} \rangle$	12
2.5 Critical total average excluded volume, $\langle V_{ex} \rangle$	14
2.6 Critical volume fraction, ϕ_c	16
2.7 Conclusions	19
3 Yield strength development in crystal-melt suspensions	21
3.1 Introduction	21
3.2 Rheology of magmatic suspensions	23
3.2.1 Fluid behavior - region A	23
3.2.2 Onset and development of yield strength - region A''	25
3.3 Methods	26
3.4 Results	30

3.5	Discussion	33
3.5.1	Onset of yield strength	34
3.5.2	Scaling relation for $\tau_y(\phi)$ curves of differing particle shapes, and other generalizations	38
3.5.3	Implications	42
3.6	Conclusions	44
4	Hydroseismicity	46
4.1	Introduction	46
4.2	Data and analysis	48
4.3	Discussion	55
4.3.1	Causes of hydroseismicity	56
4.3.2	Analytic model	60
4.3.3	Hydraulic diffusivity	62
4.3.4	Critical pore-fluid pressure change	64
4.3.5	Hydraulic conductivity and permeability	67
4.4	Conclusions	69
5	Permeability-depth curve	70
5.1	Introduction	70
5.2	Four depth scales of \mathbf{k}	72
5.2.1	Spring discharge model: $k(z < 0.1 \text{ km})$	74
5.2.2	Coupled heat and groundwater transfer model: $k(z < 1 \text{ km})$	76
5.2.3	Groundwater-recharge-induced seismicity model: $k(z < 5 \text{ km})$	88
5.2.4	Magma intrusion and degassing model: $k(z < 15 \text{ km})$	90
5.3	Conversions between κ , K , and k	93
5.4	Discussion	95
5.4.1	Heterogeneity and anisotropy of permeability	95
5.4.2	Basal heat-flow, H_b	106
5.5	Conclusions	107

6	Glacier-induced volcanism	109
6.1	Introduction	109
6.2	Data analysis	111
6.3	Discussion	115
6.4	Conclusions	121
7	Conclusions	122
7.1	Continuum percolation theory	122
7.2	Yield strength development in crystal-melt suspensions	123
7.3	Hydroseismicity	124
7.4	Permeability-depth curve	125
7.5	Glacier-induced volcanism	126
A	Appendix to Chapter 4: Hydroseismicity	128
A.1	Seismometer information	128
A.2	Box-Jenkins method	129
A.3	Moving polynomial interpolation	129
A.4	Correlation coefficients	130
B	Appendix to Chapter 5: Permeability-depth curve	131
B.1	Definition of symbols	131
B.2	Derivation of the equation for a $T(z)$ -profile with an exponential decrease in permeability	132
B.3	Derivation of the equation for a $T(z)$ -profile with constant hydraulic conductivity	133
B.4	Finite difference method	134
B.5	Axisymmetric flow	136
	Bibliography	153

List of Figures

2.1	Visualization of a <i>simplified</i> simulation of large biaxial oblate and prolate prisms	10
2.2	Illustration of the overlap of two objects in a 2D system with parallel-aligned objects	11
2.3	Normalized average excluded volume as a function of object aspect ratio and shape anisotropy	13
2.4	Critical total average excluded volume and critical volume fraction at the percolation threshold	17
3.1	Sketch of the development of effective shear viscosity and yield strength as a function of crystal fraction	24
3.2	Simulation of crystal intergrowth	27
3.3	Resolution requirements	28
3.4	Visualizations of a simulation of randomly oriented elongated rectangular biaxial soft-core prisms	30
3.5	Simulation results of the critical volume fraction for randomly oriented soft-core prisms and ellipsoids	31
3.6	Simulation results of critical volume fraction versus aspect ratio for randomly oriented triaxial soft-core prisms	32
3.7	Size effects on critical crystal volume fraction	33
3.8	Image of a pahoehoe sample close to the percolation threshold	37
3.9	“Quasi” invariant for scaling purposes	41
3.10	Scaling of yield strength curves from prisms to spheres	43
4.1	Seismicity at Mt. Hood, Oregon	48

4.2	Gutenberg-Richter plot	49
4.3	Stream discharge of Salmon River, Oregon	50
4.4	Histograms of seismicity and stream discharge	51
4.5	Period content of time series	52
4.6	Original and interpolated time series	54
4.7	Interpolated time series	55
4.8	Time lag versus cross-correlation coefficients	56
4.9	Time lag versus mean moving cross-correlation coefficients	57
4.10	Relationship between stresses (Mohr-circle)	58
4.11	Periodic pore-fluid pressure fluctuations	61
4.12	Hydrostatic pressure with superimposed periodic pore-fluid pressure fluctuations	63
5.1	Study region	73
5.2	Spring discharge model	76
5.3	Schematic illustration of 1D groundwater recharge area	78
5.4	Radius of curvature of the Earth's surface near Santiam Pass, Oregon	80
5.5	Groundwater flow streamlines at a (mostly vertical 1D-flow) recharge region	81
5.6	Shaded relief map of Mt. Hood, Oregon, and subsurface temperature distribution	84
5.7	Temperature, vertical groundwater flow velocity, and hydraulic con- ductivity versus depth in a 1D-flow recharge region	86
5.8	Geotherm measurements and models for Mt. Hood	89
5.9	Magma intrusion underneath the Cascades range volcanic arc.	91
5.10	Near-surface heat-flow map	97
5.11	Permeability, k , as a function of depth, z	101
6.1	Shaded relief map with locations of basaltic and silicic eruptions in Long Valley and Owens Valley volcanic fields, eastern California . . .	110
6.2	Original, binned, interpolated, differentiated, and cross-correlated data for basaltic and silicic volcanic eruptions, as well as for glaciation . .	112
6.3	Mean cross-correlation coefficients from Figure 6.2c,d	113

6.4	Power spectra for $\delta^{18}\text{O}$ and volcanic eruptions	114
6.5	Conceptual model of a magmatic system in the Sierras	119
6.6	Phase lag and amplitude of the transfer function relating glacial unloading to volcanisms	120
B.1	Schematic illustration of the computational grid in cylindrical coordinates used for heat and groundwater transfer modeling	137

List of Tables

5.1	Spring model input and results	77
5.2	Parameters for coupled groundwater and heat-flow models	88
5.3	Conversions from hydraulic conductivity, K , to permeability, k	96

Acknowledgements

Numerous people have contributed in various ways to my completion of this dissertation. I would like to thank my adviser, Michael Manga, for his continuous support, motivation, and encouragement during my Ph.D. studies and for introducing me to research. I am also very grateful to have had the opportunity to discuss science, and work with researchers from the University of Oregon, University of California - Berkeley, Lawrence Berkeley National Laboratory, and the U.S. Geological Survey. Some of these colleagues, friends, and mentors include Kathy Cashman, Dana Johnston, Eugene Humphreys, Steve Ingebritsen, Jamie Rector, and Chi-Yuen Wang. In addition, I would like to thank fellow graduate and undergraduate students as well as postdocs with whom I shared lab and office spaces, had many stimulating research discussions, and participated in inspiring field trips. Here, I would like to thank Dayanthie Weeraratne, Chad Dorsey, Adam Soule, Rebecca and Cliff Ambers, Alison Rust, Jason Crosswhite, Derek Schutt, Helge Gonnermann, Dave Stegman, David Schmidt, Ingrid Johanson, Mark Wenzel, Mark Jellinek, Emily Brodsky, and Mike Singer. Funding for the research presented in this dissertation was generously provided by the National Science Foundation, the American Chemical Society (Petroleum Research Fund), the Sloan Foundation, and Lawrence Berkeley National Laboratory. I am grateful to my parents, Karin and Rüdiger Saar, and my brother, Bernd Saar, for their belief in me and their support and encouragement in all my endeavours. Diane, Cap, Amy, and Rob Tibbitts are thanked for making me feel at home and being part of their family. Finally, I am very thankful to my wife, Amy Saar, for her love, companionship, support, and encouragement without which this dissertation would not have been possible.

Chapter 1

Introduction

In this dissertation, I investigate processes in hydrogeology and volcanology, as well as in rheology of suspensions in general. These investigations have in common the application of fluid mechanics and the use of numerical and analytical modeling techniques. The importance of applying concepts from fluid mechanics to geological problems is nicely summarized by H.E. Huppert [74] in his classic paper entitled “The intrusion of fluid mechanics into geology.” The objective in this dissertation is to gain quantitative insight into processes governing the flow of subsurface water on the one hand, and magma and lava flow on the other hand. For the latter two (hereafter collectively referred to as magma), an understanding of the complex and time-dependent rheology of crystal-melt suspensions is critical. Thus, I also conduct research investigating the rheology of suspensions, employing a percolation theory approach.

Percolation theory describes the transport properties of random, multiphase systems and materials and can thus be applied to numerous problems in the physical sciences, warranting research in itself. As a result, I first present a more general

study of continuum percolation theory in Chapter 2. In Chapter 3 I then apply results from percolation theory to magma rheology. Results from the study of magma rheology provide new insights into the transition from pahoehoe to 'a'a flows. Other volcanological phenomena, including the dynamics of eruptions (effusive versus explosive), may also be investigated using this approach but are not specifically addressed here.

Within the subject of hydrogeology I focus on the interactions between groundwater flow and other geological processes such as seismicity (Chapter 4) and heat-flow (Chapter 5). Of particular interest are tectonically active regions that show both frequent earthquakes and high heat-flow. However, the techniques employed are not restricted to such geologic settings. Even in intraplate regions, perturbations from a linear, conductive temperature-depth profile, as well as recognition of spatial and temporal patterns in the occurrence of micro-earthquakes, may allow deduction of hydrogeologic processes and parameters. Nonetheless, convergent plate boundaries, such as the subduction zone between the Juan-de-Fuca and the North-American plate, serve as ideal study regions because they have relatively high rates of magma intrusion, heat-flow, volcanic eruptions, and seismicity. As a result, in Chapter 4 I study the Oregon Cascades in the Pacific Northwest of the USA and investigate groundwater-recharge induced seismicity, hereafter referred to as hydroseismicity. In Chapter 5 I study the more general problems of coupled heat- and groundwater transfer. In addition, I employ spring-discharge and magma intrusion models in order to infer the characteristics of the decrease in permeability as a function of depth. Such permeability-depth curves are important for developing large-scale regional groundwater flow models.

Finally, there may also be a connection between hydrological processes and vol-

canic eruptions. In Chapter 6 I show that similar to the effects of reservoirs on hydroseismicity, stress changes, caused by variations in the load exerted by surface water or ice, can affect the frequency of eruptions.

Large-scale flow models in porous media are generally underconstrained. It is thus desirable to use multiple direct and indirect observations, such as standard hydrogeologic boundary conditions and parameters as well as temperature distributions, heat-flow, and hydroseismicity data to improve such simulations. Other implications of utilizing multiple processes and constraints, as well as developing large-scale models of mass and energy transfer, lie in the areas of water management, geothermal energy resources, and assessment of volcanic and (hydro-) seismic hazards. Further implications include basic geological and geophysical research concerning water and magma transport, interactions between fluids, heat, and earthquakes, and the effects of a material's rheology on transport processes. The latter subject also has implications in material science.

To investigate geological processes quantitatively, I employ numerical and analytical methods at various temporal and spatial scales. Scales considered range from particle interactions in suspensions to flow phenomena in mountain ranges. Methods employed include percolation theory, signal processing, inverse theory, statistics, and fluid flow simulations. Data used for calculations and models are obtained from field work (e.g., on Hawai'i and in the Oregon Cascades), laboratory measurements (e.g., permeability of rock cores), and from third parties (e.g., temperature-depth profiles from the US Geological Survey, Menlo Park).

Because of the wide range of topics covered, each following chapter includes a separate introduction and conclusion section and is largely based either on previous

publications (Saar and Manga [158]¹ for Chapter 2, Saar et al. [160]² for Chapter 3, and Saar and Manga [159]³ for Chapter 4) or on manuscripts that are in review at the time this dissertation is being written (Chapters 5 and 6). Some details not provided in these publications and manuscripts have been included in the chapters or are provided in additional appendices. Definitions of symbols are unique to each chapter. A conclusion chapter summarizes the main findings of this dissertation.

¹Saar, M. O., and M. Manga, Physical Review E, Vol. 65, Art. No. 056131, 2002. Copyright (2002) by the American Physical Society.

²Reprinted from Earth and Planetary Science Letters, Vol. 187, Saar, M. O., M. Manga, K. V. Cashman, and S. Fremouw, Numerical models of the onset of yield strength in crystal-melt suspensions, 367-379, Copyright (2001), with permission from Elsevier.

³Reprinted from Earth and Planetary Science Letters, Vol. 214, Saar, M. O., and M. Manga, Seismicity induced by seasonal groundwater recharge at Mt. Hood, Oregon, 605-618, Copyright (2003), with permission from Elsevier.

Chapter 2

Continuum percolation theory

This chapter is largely based on Saar and Manga [158]¹.

2.1 Introduction

The transport properties of multiphase materials may either reflect the deformation of the material as a whole under applied stress (rheology) or the transfer of some medium, such as electrons or fluids, within the material (conductivity). Both types of transport are fundamentally different and depend on the relevant material properties in different ways. However, rheology and conductivity of composite materials are both determined in part by the interconnectivity of their individual elements (objects) that constitute their phases.

Percolation theory describes interconnectivity of objects in a random multiphase system as a function of the geometry, distribution, volume fraction, and orientation

¹Saar, M. O., and M. Manga, Physical Review E, Vol. 65, Art. No. 056131, 2002. Copyright (2002) by the American Physical Society.

of the objects. The structure of the composite material may evolve with time due to chemical reactions or temperature changes. A critical threshold may be passed during the structural evolution and as a result some material properties such as yield strength or conductivity can change abruptly and may exhibit a power-law behavior above, and close to, the so-called percolation threshold.

Examples of composite materials that show time-dependent rheology include cements [15], gels [20], and magmas [160] (see also Chapter 3). Similarly, the conductivity of a medium for fluids (permeability) or electrons may change with time. For example the permeability of a material changes with the formation or closure of pores and fractures in solids [78] or with growth and coalescence or degassing of bubbles in liquids [156, 157]. Similarly, electrical conductivity depends on the amount, geometry, and interconnectivity of the conductor [44, 176, 209]. In general, multiple processes [191] in the Physical, Chemical, Biological, and Earth Sciences appear to show power-law, i.e., fractal, properties above a certain threshold and may thus be described by percolation theory.

Several soft-core (interpenetrating objects) continuum (randomly positioned) percolation studies have been conducted in three-dimensional (3D) systems. Investigated 3D percolating objects include spheres [61, 105, 141, 167], parallel-aligned [176] or randomly oriented [50] ellipsoids, parallel-aligned cubes [176], and randomly oriented hemispherically capped cylinders [8, 9]. In some studies randomly oriented 2D ellipses [31] and 2D polygons [78] are placed in a 3D system to simulate fractures where the third object dimension may be neglected.

In this chapter I investigate continuum percolation for randomly oriented 3D soft-core prisms. The objective is to point out similarities between prisms and other percolation systems studied previously, to expand on explanations for differences using

the excluded volume concept [135] as introduced by Balberg [5, 8], and to compare the number of bonds per object to the total average excluded volume [8]. The latter two parameters may serve as “quasi”-invariants [5, 8, 41]. I investigate prisms because in a 3D system, results can be compared in the extreme oblate limit with 2D polygons and 2D ellipses, in the extreme prolate limit with hemispherically capped cylinders or rods, and for all aspect ratios with ellipsoids. Furthermore, this study is motivated by the observation that some media, such as suspensions containing prismatic particles that can intergrow (e.g., crystal-melt suspensions, such as some magmas [160]) may best be described by interpenetrating 3D polyhedra.

Parameters of interest at the percolation threshold are the critical number density of prisms, n_c , the critical prism volume fraction, ϕ_c , and the critical total average excluded volume $\langle V_{ex} \rangle$. The latter parameter is given by $\langle V_{ex} \rangle \equiv n_c \langle v_{ex} \rangle$ [8], where the excluded volume, v_{ex} , is the volume around an object in which the center of another such object cannot be placed without overlap [135]. The brackets, $\langle \rangle$, denote spatial averaging over all orientation (and size) distributions. I determine numerically the average excluded volume, $\langle v_{ex} \rangle$, for some prism shapes. Finally, the critical average number of bonds per object, B_c , is determined numerically and compared with $\langle V_{ex} \rangle$. All parameters are investigated for possible contributions to an invariant allowing predictions of percolation thresholds. Because of the sometimes misleading nomenclature, especially concerning B_c , I review some percolation theory concepts throughout this chapter.

2.2 Method

In a soft-core system the percolation threshold is reached when a continuous pathway of overlapping objects exists connecting opposing sides of a bounding box. The computer code developed determines the percolation threshold and related parameters for convex 3D soft-core polyhedra of any shape, size, and orientation distribution that are randomly positioned (continuum percolation). Here, I focus on randomly oriented biaxial and triaxial soft-core prisms of uniform size. In soft-core continuum percolation, size distribution of objects does not appear to affect ϕ_c [160] and results for parallel-aligned objects are independent of object shape [5].

Overlap of objects is determined analytically. The volume fraction of a phase is determined by the number density of objects, n , that constitute the phase and the object's unit volume, V , by [51]

$$\phi = 1 - \exp(-nV). \quad (2.1)$$

Results for ϕ using Eq. (2.1) can be verified through comparison with numerical volume fraction calculations using a space discretization method [160]. In order to reduce finite size effects and the possibility of imposing large-scale structure I place objects within a large unit bounding box whose volume typically is 8 to 64 times larger than the volume of an inner bounding box used to determine connection between opposing sides (Fig. 2.1). The more common approach is to perform calculations with periodic boundary conditions [31, 50, 78]. In all simulations, the largest object side length is one tenth or less of the side length of the inner bounding box. Fig. 2.1 shows visualizations of simplified simulations for randomly oriented biaxial oblate and prolate prisms.

The computational method is tested by comparing results with well-established

values, such as ϕ_c and $\langle v_{ex} \rangle$ for spheres and parallel-aligned objects [8, 176], and by visualizations of simulations at low n_c . Moreover, the critical number density of clusters per unit volume, n_{sc} , at percolation scales as $n_{sc} \propto s^{-\tau}$ over more than 4 orders of magnitude of s , where s is the number of objects in a cluster and $\tau \approx 2.2$. Thus, the cluster size distribution follows the power-law relationship expected between n_{sc} and s close to the percolation threshold [7, 181], suggesting that finite size effects are minimal.

For two continuous convex objects the average excluded volume $\langle v_{ex} \rangle$ can be determined analytically by

$$\langle v_{ex} \rangle = V_a + V_b + (A_a R_a + A_b R_b)/4\pi, \quad (2.2)$$

where V is the volume, A the area, and R the mean radius of curvature of the objects a and b [86]. The prisms in this study, however, have corners so that R , and thus $\langle v_{ex} \rangle$, cannot be determined analytically using Eq. (2.2). Instead I employ a method analogous to Garboczi et al. [50] and de la Torre et al. [32], and determine $\langle v_{ex} \rangle$ numerically by randomly placing two objects of random orientation within a box and testing for overlap. This is repeated typically 10^6 times and the ratio of the number of overlaps over the total number of trials times the volume of the box is $\langle v_{ex} \rangle$. To obtain a mean and a standard error, I repeat the above procedure ten times. I test this method for the case of parallel-aligned objects of volume V , where in 3D for any convex object shape $\langle v_{ex} \rangle = 8 \times V$. This is also a test of the contact function for objects [50].

All simulations are repeated 10 times to calculate a mean and its standard error for ϕ_c , n_c , and B_c . Error bars in all figures indicate 95 % confidence intervals. Biaxial object aspect ratios are given as small over large and as large over small axis length for oblate and prolate objects, respectively. The shape anisotropy, ξ , of an object is

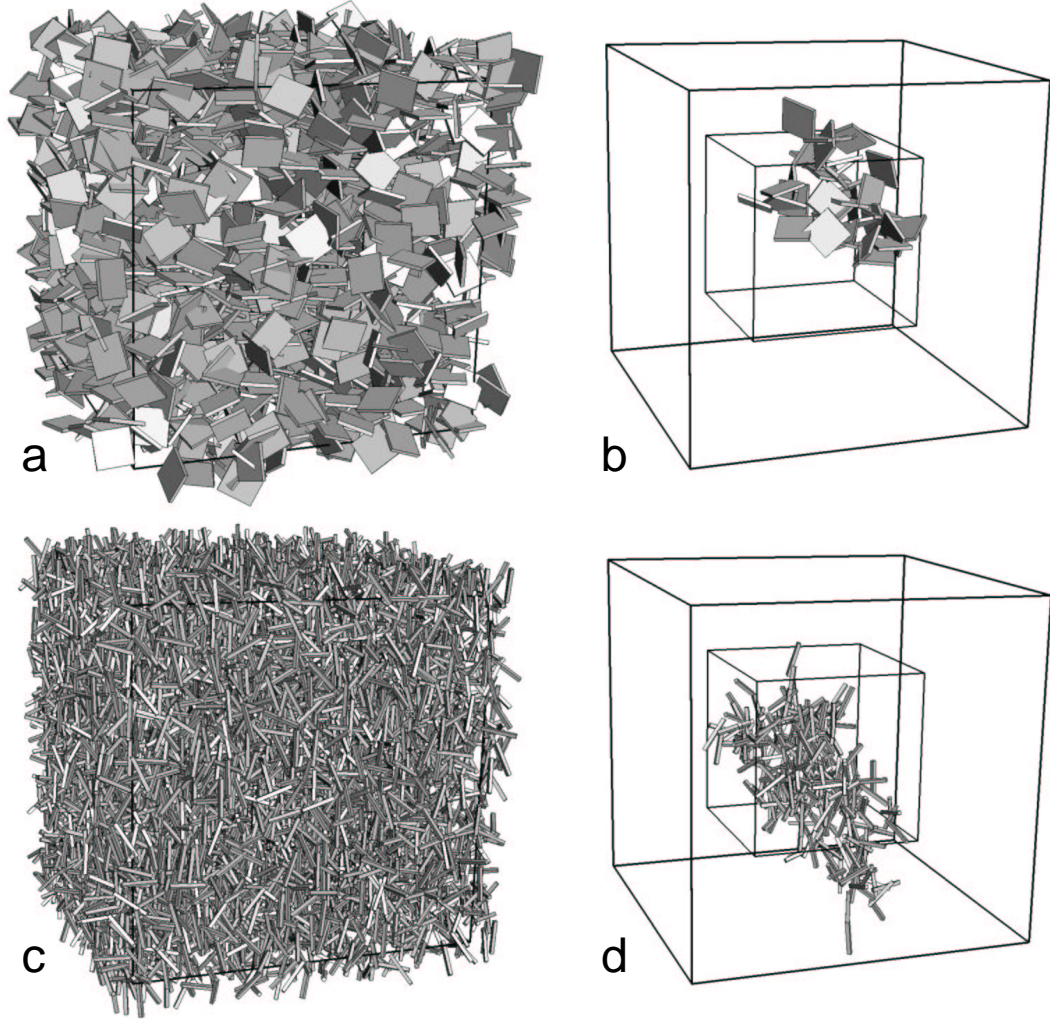


Figure 2.1. Visualization of a *simplified* simulation of large biaxial oblate (a, b) and prolate (c, d) prisms with aspect ratios 1:10 (short over long axis) and 10:1 (long over short axis), respectively. The critical number densities are $n_c = 1060$ and $n_c = 7025$ for the oblate and prolate prism simulations, respectively. In *actual* simulations object side lengths are about 1/10 or less than the side length of the inner bounding box. n_c increases with object elongation up to $n_c = 7 \times 10^5$ for prolate prisms of aspect ratio 1000:1. The inner bounding box is used to determine if a continuous phase, or backbone (b, d) exists (percolation threshold). Objects are placed throughout the inner and outer bounding box and within a fringe around the outer box so that objects can protrude into the box (a, c). The average number of bonds per object, B_c , and the number density, n_c , are determined using all object overlaps and object centers, respectively, that fall within the large bounding box.

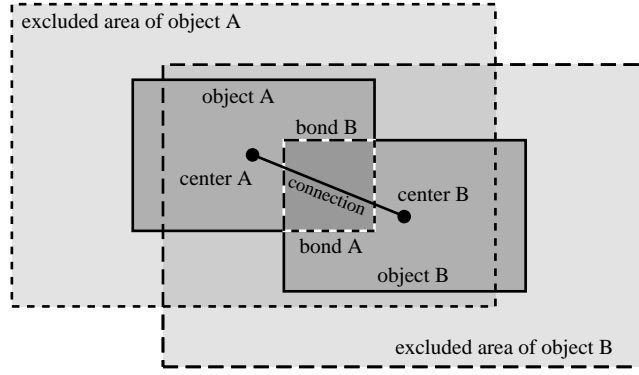


Figure 2.2. Illustration of the overlap of two objects in a 2D parallel-aligned system (for easier visualization). The center of each object A and B falls within the other object's excluded area, each resulting in an overlap, or bond. The number of bonds is 2. In contrast, the number of connections per object is the total number of bonds (2) divided by the total number of objects (2), here resulting in one connection. In 3D-systems, randomly oriented objects have average excluded volumes, rather than excluded areas.

defined here as the ratio of large over short axis length for both oblate and prolate objects.

2.3 Average number of bonds per object, B_c

Objects in soft-core continuum percolation can interpenetrate each other. The average excluded volume, $\langle v_{ex} \rangle$, is always defined for 2 objects (A and B). When placed within a unit volume $\langle v_{ex} \rangle$ describes the probability of each center, A and B, being within the other object's excluded volume, each causing an overlap, or bond (Fig. 2.2).

Therefore, in a unit volume, $n \langle v_{ex} \rangle$ describes the probability of n object centers being within n excluded volumes each causing an overlap, or bond, for each individual object, or two bonds per connection (Fig. 2.2). This method of counting each bond is

commonly referred to as counting “bonds per object,” which has to be distinguished from the more intuitive average number of connections per object,

$$C = \frac{\text{total number of bonds}}{\text{total number of objects}}, \quad (2.3)$$

denoted C_c at percolation. The critical average number of bonds per object at percolation is given by [8]

$$B_c = n_c \langle v_{ex} \rangle \quad (2.4)$$

and thus [137]

$$C_c = \frac{n_c \langle v_{ex} \rangle}{2} = \frac{B_c}{2}. \quad (2.5)$$

For example $B_c = 1.4$ indicates a 140 % probability per object to have a bond, or on average each object has 1.4 bonds, or 0.70 connections.

I determine B_c (and thus C_c), n_c , and $\langle v_{ex} \rangle$ numerically and can thus confirm Eqs. (2.4, 2.5) for randomly oriented prisms. For example, for an aspect ratio of 3:1 I obtain $\langle \overline{v_{ex}} \rangle = \langle v_{ex} \rangle / V = 13.1$ and $\langle \overline{v_{ex}} \rangle = B_c / (n_c V) = 13.3$. Hereafter, I use Eq. (2.4) to calculate $\langle v_{ex} \rangle$ from B_c and n_c for randomly oriented prisms. In general, the larger number of overlaps in my simulation results in a more rapid and accurate estimate of $\langle v_{ex} \rangle$ using Eq. (2.4) than the method described in Section 2.2.

2.4 Normalized average excluded volume, $\langle \overline{v_{ex}} \rangle$

The normalized average excluded volume,

$$\langle \overline{v_{ex}} \rangle = \langle v_{ex} \rangle / V, \quad (2.6)$$

is the factor by which the excluded volume is larger than the actual volume, V , of an object. Fig. 2.3 shows $\langle \overline{v_{ex}} \rangle$ as a function of aspect ratio for randomly oriented (solid

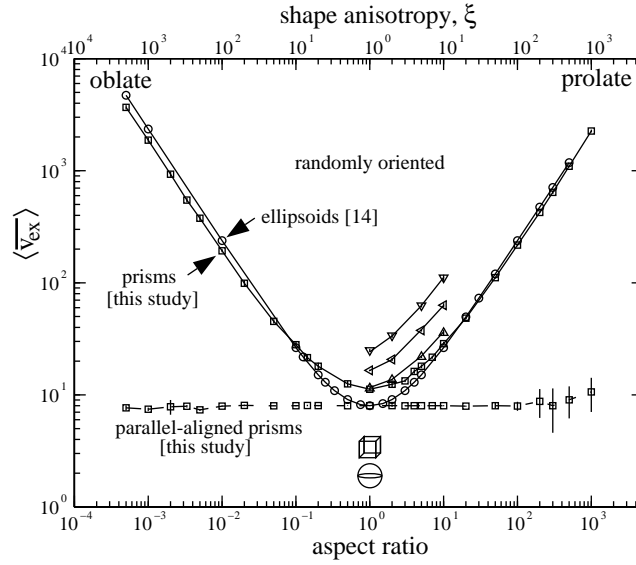


Figure 2.3. Normalized average excluded volume $\langle \overline{v_{ex}} \rangle$ as a function of object aspect ratio (and shape anisotropy, ξ) for biaxial (squares) and triaxial (triangles) prisms (this study) and rotational (biaxial) ellipsoids (circles, from [50]). Solid and dashed lines indicate random and parallel orientation, respectively. Error bars for prisms indicate 95 % confidence intervals. Short over medium axis aspect ratios for triaxial prisms are 1/2 (upward pointing triangle), 1/5 (leftward pointing triangle), and 1/10 (downward pointing triangle). Long over medium axis aspect ratios are as indicated by the figure axis. $\langle \overline{v_{ex}} \rangle$ is calculated using B_c and n_c in Eq. (2.4) for randomly oriented prisms (squares along solid line). Squares along the dashed line show $\langle \overline{v_{ex}} \rangle$ for parallel-aligned biaxial prisms, determined using the method described in Section 2.2.

line) biaxial (squares) and triaxial (triangles) prisms and for parallel-aligned biaxial prisms (squares along dashed line).

As indicated in Section 2.2, $\langle \overline{v_{ex}} \rangle = 8$ for any parallel-aligned convex 3D object. In contrast, randomly oriented biaxial prisms exhibit an increase in $\langle \overline{v_{ex}} \rangle$ with increasing shape anisotropy, ξ , due to flattening or elongation. The combined effect of 3 different axis lengths of randomly oriented triaxial prisms increases $\langle \overline{v_{ex}} \rangle$ further. This dependency of $\langle \overline{v_{ex}} \rangle$ on shape anisotropy is expected because randomly oriented objects with eccentric shapes have a higher probability to overlap than objects of

more equant shapes. In the extreme oblate and prolate limits the exponents in the power-law between aspect ratio and $\langle \overline{v_{ex}} \rangle$ are close to ± 1 (Fig. 2.3) indicating a linear relationship.

Also shown in Fig. 2.3 (circles) is the normalized average excluded volume, $\langle \overline{v_{ex}} \rangle_e$, for rotational ellipsoids from [50] recalculated from their data and Eq. (11) in [50]. Identical values are obtained for $\langle \overline{v_{ex}} \rangle_e$ when using data from [50] and employing Isihara's [86] original equation as formulated by Nichol et al. [129] and given here in the notation adopted for this chapter and with volume normalization as

$$\langle \overline{v_{ex}} \rangle_e = 2 + \frac{3}{2} \left(1 + \frac{\sin^{-1} \epsilon}{\epsilon \sqrt{1 - \epsilon^2}} \right) \left(1 + \frac{1 - \epsilon^2}{2\epsilon} \ln \frac{1 + \epsilon}{1 - \epsilon} \right), \quad (2.7)$$

where the eccentricity $\epsilon^2 = 1 - b^2/a^2$ is given for prolate and oblate ellipsoids with long axis, a , and short axis, b .

2.5 Critical total average excluded volume, $\langle V_{ex} \rangle$

At the percolation threshold, the product in Equation (2.4) is also called the critical total average excluded volume [8],

$$\langle V_{ex} \rangle \equiv n_c \langle v_{ex} \rangle = B_c. \quad (2.8)$$

Fig. 2.4a shows $\langle V_{ex} \rangle$ as a function of prism aspect ratio for all biaxial and some triaxial prisms investigated. Balberg [5] and others [9, 61] show that in 3D soft-core percolation $\langle V_{ex} \rangle = 2.8$ for spheres and parallel-aligned objects of any convex shape, $\langle V_{ex} \rangle = 0.7$ for orthogonally aligned (macroscopically isotropic) widthless sticks, and intermediate, $\langle V_{ex} \rangle \approx 1.4$ for highly-elongated randomly oriented cylinders with hemispherical caps. My results of $1.3 < \langle V_{ex} \rangle < 2.79$, for randomly oriented biaxial prisms, fall within Balberg's [5] bounds.

In the extreme oblate biaxial prism limit my simulations yield

$$\langle V_{ex} \rangle \approx 2.3 \quad (\text{extreme oblate prism limit}). \quad (2.9)$$

This result is in close agreement with studies of similar object shapes (Fig. 2.4a) such as 2D polygons [78] and 2D ellipses [31] placed in a 3D system where $2.22 \leq \langle V_{ex} \rangle \leq 2.30$ and $\langle V_{ex} \rangle = 2.2$, respectively (my definition of $\langle V_{ex} \rangle$ is based on a unit volume bounding box and thus already normalized). The 2D shapes may be viewed as the extreme oblate limit of 3D objects. Garboczi et al. [50] report $\langle V_{ex} \rangle = 3.0$ for randomly oriented oblate rotational (biaxial) ellipsoids, a value higher than the one introduced here and above the upper bound of 2.8 suggested by Balberg [5]. This discrepancy has been noted by Garboczi et al. [50] and others [31, 78]. Results presented in Section 2.6 also suggest that for rotational ellipsoids values of $\langle V_{ex} \rangle$ are lower and possibly equal to values for biaxial prisms.

For an extreme prolate biaxial prism of aspect ratio 1000:1 I observe

$$\langle V_{ex} \rangle \approx 1.3 \quad (\text{extreme prolate prism limit}) \quad (2.10)$$

(Fig. 2.4a). Balberg [5] finds $\langle V_{ex} \rangle \approx 1.4$ for extremely elongated randomly oriented cylinders with hemispherical caps.

In general, maximum values of $\langle V_{ex} \rangle = 2.8$ occur for parallel-aligned objects of any convex shape [9, 176], where the most equant shape possible, a sphere, is always aligned. Therefore, it may be expected that I find a maximum of

$$\langle V_{ex} \rangle \approx 2.79 \quad (\text{cubes}) \quad (2.11)$$

for the most equant prism shape, a cube (Fig. 2.4a), where the effect of randomness in orientation is at a minimum.

It has been argued [5, 39, 41, 50] that the total average excluded volume $\langle V_{ex} \rangle$ is not a true invariant but may be viewed as an approximate invariant that is less

sensitive to object shapes than ϕ_c . My results confirm this reduced variability of $\langle V_{ex} \rangle$ as a function of shape aspect ratio (Fig. 2.4). At the same time $\langle V_{ex} \rangle \approx 2.3$ shows good agreement between extremely oblate prisms, 2D polygons, and 2D ellipses, where the 2D-shapes are the extreme oblate 3D limits. Similarly, $\langle V_{ex} \rangle \approx 1.3$ applies to extremely prolate prisms, ellipsoids, and rods (hemispherically capped cylinders).

2.6 Critical volume fraction, ϕ_c

Fig. 2.4b shows ϕ_c as a function of aspect ratio for randomly oriented soft-core biaxial (squares) and triaxial (triangles) prisms. The maximum value of ϕ_c is reached for the most equant prism shape (cube with aspect ratio 1:1:1). Increasing shape anisotropies due to flattening or elongation decrease ϕ_c for biaxial prisms. The combined effect of flattening and elongation of triaxial prisms decreases ϕ_c further (Fig. 2.4b). The larger the shape anisotropy of an object the greater its normalized excluded volume, $\langle \overline{v_{ex}} \rangle$ (Fig. 2.3) and probability of overlap. As a result, percolation occurs at lower number densities, n_c . Lower n_c values for different object shapes result in reduced ϕ_c in Eq. (2.1), where differences in object volume have already been accounted for by the volume normalization in $\langle \overline{v_{ex}} \rangle$.

The circles in Fig. 2.4b are results from Garboczi et al. [50] for randomly oriented soft-core rotational (biaxial) ellipsoids. Curves of ϕ_c , as a function of aspect ratio, for ellipsoids and prisms have similar shapes but are offset for the most equant shapes and converge in the extreme oblate and prolate limits. The offset between the curves for prisms and ellipsoids may be a function of the ratio

$$R = \frac{\langle \overline{v_{ex}} \rangle_e}{\langle \overline{v_{ex}} \rangle_p} \quad (2.12)$$

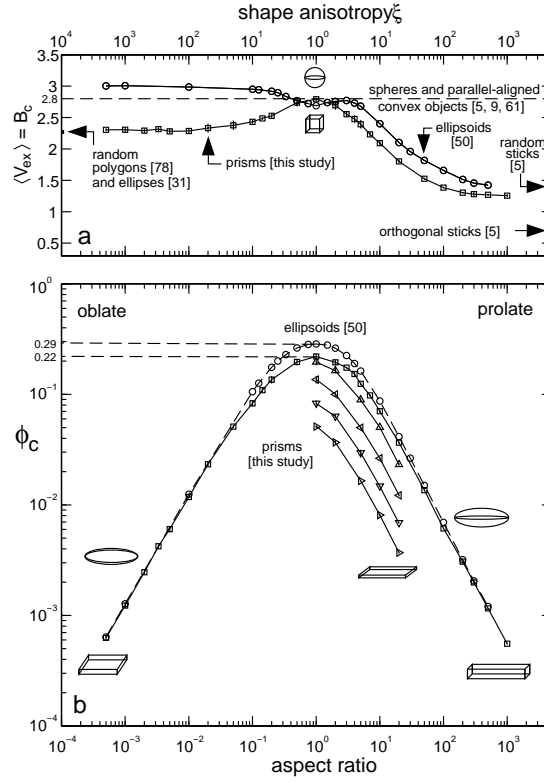


Figure 2.4. Critical total average excluded volume, $\langle V_{ex} \rangle$ (panel a), and critical volume fraction, ϕ_c (panel b), at the percolation threshold versus aspect ratio (and shape anisotropy, ξ) for biaxial (squares) and triaxial (triangles) prisms (this study) and rotational (biaxial) ellipsoids (circles, from [50]). Short over medium axis aspect ratios for triaxial prisms are 1/2 (upward pointing triangle), 1/5 (leftward pointing triangle), 1/10 (downward pointing triangle), and 1/20 (rightward pointing triangle). Long over medium axis aspect ratios are as indicated by the figure axis. Error bars for prisms indicate 95 % confidence intervals.

for a given aspect ratio. If I assume that for a given aspect ratio

$$\langle V_{ex} \rangle_p \cong \langle V_{ex} \rangle_e \quad (2.13)$$

then by Eq. (2.8)

$$n_p \langle v_{ex} \rangle_p = n_e \langle v_{ex} \rangle_e, \quad (2.14)$$

where here and in all following equations the subscripts e and p denote parameters

for ellipsoids and prisms, respectively. All parameters are defined as before with n_p , n_e , $\langle V_{ex} \rangle_p$, $\langle V_{ex} \rangle_e$, ϕ_p , and ϕ_e being critical values at the percolation threshold. Substituting Eq. (2.1) into Eq. (2.14) yields

$$\frac{\langle v_{ex} \rangle_p}{V_p} \ln(1 - \phi_p) = \frac{\langle v_{ex} \rangle_e}{V_e} \ln(1 - \phi_e). \quad (2.15)$$

Applying Eq. (2.6) to the appropriate terms for prisms and ellipsoids in Eq. (2.15), then substituting Eq. (2.12), and rearranging yields the critical prism volume fraction,

$$\phi_p = 1 - (1 - \phi_e)^R. \quad (2.16)$$

In the extreme oblate and prolate limits, the ratio in the exponent, R , approaches one (Fig. 2.3) and thus Eq. (2.16) reduces to $\phi_p = \phi_e$ as expected from Fig. 2.4b. For the most equant shape (cube and sphere) the ratio is at its minimum of

$$R = \frac{8.00}{10.56} = 0.758, \quad (2.17)$$

indicating that the normalized average excluded volume for a sphere is 75.8 % of the one for a cube. The larger excluded volume of a cube with respect to a sphere causes percolation at a lower volume fraction for cubes than for spheres. With the result from Eq. (2.17) and $\phi_e = 0.2896$ [50, 105, 141, 167] for spheres Eq. (2.16) yields $\phi_p = 0.23$ for cubes, agreeing, to within the uncertainty, with my numerical results of $\phi_p = 0.22$. The agreement between results from Eq. (2.16) and numerical results (Fig. 2.4b) for the most equant shapes as well as for the extreme aspect ratio limits suggest that $\langle V_{ex} \rangle$ may be invariant for a given aspect ratio as postulated by Eq. (2.13). Thus, the curves in Fig. 2.4a are expected to converge for a given aspect ratio, possibly to $\langle V_{ex} \rangle_p$ for prisms which agrees with results for 2D objects (Fig. 2.4a).

In the extreme oblate and prolate limits, the exponents of the power-law relating aspect ratio (or shape anisotropy, ξ) to ϕ_c are close to ± 1 (line of slope ± 1 in

Fig. 2.4b), indicating a linear relationship. Indeed, because ϕ_c is comparable for ellipsoids and prisms for $\xi > 50$, in this limit, the linear relationships

$$\phi_c = \begin{cases} 0.6/\xi & \text{(prolate)} \\ 1.27/\xi & \text{(oblate)} \end{cases} \quad (2.18)$$

hold true for both biaxial prisms (this study) and rotational ellipsoids [50], where the shape anisotropy, ξ , is the ratio of large over small axis for both prolate and oblate objects.

2.7 Conclusions

The percolation system of randomly oriented 3D soft-core prisms serves as a link combining characteristics between other systems such as 3D ellipsoids, 3D cylinders with hemispherical caps (rods), 2D polygons, and 2D ellipses. All objects are randomly oriented and randomly placed in the 3D continuum. The 2D shapes are the extreme oblate limit of 3D objects.

Percolation parameters such as the critical volume fraction, ϕ_c , the critical total average excluded volume, $\langle V_{ex} \rangle \equiv n_c \langle v_{ex} \rangle$, or equivalently the average number of bonds per object, $B_c = n_c \langle v_{ex} \rangle$, can be related in most of the above mentioned systems. Here, in the extreme oblate and prolate limits $B_c \approx 2.3$ and $B_c \approx 1.3$, respectively. The minimum shape anisotropy of prisms is matched for cubes where $B_c = 2.79$ reaches the prism maximum, close to $B_c = 2.8$ for spheres.

With respect to biaxial prisms, triaxial prisms have increased normalized average excluded volumes, $\langle \overline{v_{ex}} \rangle$, due to increased shape anisotropies. As a result, ϕ_c for triaxial prisms is lower than ϕ_c for biaxial prisms.

An offset in the critical object volume fraction, ϕ_c , occurs between prisms and el-

lipsoids with low shape anisotropy. This offset appears to be a function of the ratio of the normalized average excluded volume for ellipsoids, $\langle \overline{v_{ex}} \rangle_e$, over $\langle \overline{v_{ex}} \rangle_p$ for prisms. Prisms and ellipsoids yield converging values for $\langle \overline{v_{ex}} \rangle$, and thus also for ϕ_c , in the extreme oblate and prolate limits. In these limits both parameters exhibit a linear relationship with respect to aspect ratio.

Chapter 3

Yield strength development in crystal-melt suspensions

This chapter is largely based on Saar et al. [160]¹.

3.1 Introduction

Magmas and lavas typically contain crystals, and often bubbles, suspended in a liquid. These crystal-melt suspensions vary considerably in crystal volume fraction, ϕ , and range from crystal-free in some volcanic eruptions, to melt-free in portions of the Earth's mantle. Moreover, the concentration of suspended crystals often changes with time due to cooling or degassing, which causes crystallization, or due to heating, adiabatic decompression, or hydration, which causes melting. Such variations in ϕ can cause continuous or abrupt modifications in rheological properties such as yield

¹Reprinted from Earth and Planetary Science Letters, Vol. 187, Saar, M. O., M. Manga, K. V. Cashman, and S. Fremouw, Numerical models of the onset of yield strength in crystal-melt suspensions, 367-379, Copyright (2001), with permission from Elsevier.

strength, viscosity, and fluid-solid transitions. Thus the mechanical properties of geologic materials vary as a result of the large range of crystal fractions present in geologic systems. The rheology of crystal-melt suspensions affects geological processes, such as ascent of magma through volcanic conduits, flow of lava across the Earth’s surface, convection in magmatic reservoirs, and shear wave propagation through zones of partial melting.

One example of a change in rheological properties that may influence a number of magmatic processes is the onset of yield strength in a suspension once ϕ exceeds some critical value, ϕ_c . The onset of yield strength has been proposed as a possible cause for morphological transitions in surface textures of basaltic lava flows [26]. Yield strength development may also be a necessary condition for melt extraction from crystal mushes under compression, as in flood basalts, or in the partial melting zone beneath mid ocean ridges [140]. Furthermore, increase of viscosity and development of yield strength in magmatic suspensions may cause volcanic conduit plug formation and the transition from effusive to explosive volcanism [35]. Indeed, Philpotts et al. [140] state that the development of a load-bearing crystalline network is “one of the most important steps in the solidification of magma.”

In this chapter I employ three-dimensional numerical percolation theory models of crystal-melt suspensions to investigate the onset of yield strength, τ_y . The simulations are based on results from Chapter 2 and the corresponding publication (Saar and Manga [158]), where the occurrence of a percolation threshold is investigated for 3D soft-core prisms in the continuum. Yield strength development due to vesicles [155, 182] is not considered in this study. The objective is to understand the geometrical properties of the crystals in suspension that determine the critical crystal volume fraction, ϕ_c , at which a crystal network first forms. My simulations suggest that the

onset of yield strength in crystal-melt suspensions may occur at crystal fractions that are lower than the 0.35-0.5 commonly assumed [95, 103, 142] in static (zero-shear) environments. I demonstrate that yield strength can develop at significantly lower ϕ when crystals have high shape anisotropy and are randomly oriented, and that an upper bound should be given by $\phi_c = 0.29$ for parallel-aligned objects. Because particle orientation is a function of the stress tensor, I expect increasing particle alignment with increasing shear stress and perfect alignment in pure shear only [110]. Furthermore, I suggest a scaling relation between τ_y and ϕ for suspensions of different particle shapes. The numerical models complement the experimental studies presented in a paper by Hoover et al. [70].

3.2 Rheology of magmatic suspensions

In this section I provide an overview of the conceptual framework in which I interpret results later. Fig. 3.1 illustrates schematically the relationship between effective shear viscosity, μ_{eff} , yield strength, τ_y , and particle volume fraction, ϕ . I make a distinction between fluid and solid (regions A and B respectively in Fig. 3.1). The subcategories A' and A'' are used for suspensions with $\tau_y = 0$ (Newtonian) and $\tau_y > 0$ (Bingham), respectively. I assume here that the suspensions are not influenced by non-hydrodynamic (e.g., colloidal) forces, Brownian motion, or bubbles. First I discuss viscosity (region A) then yield strength (subregion A'').

3.2.1 Fluid behavior - region A

Einstein [42] found an analytical solution,

$$\mu_{\text{eff}} = \mu_s(1 + 2.5\phi), \quad (3.1)$$

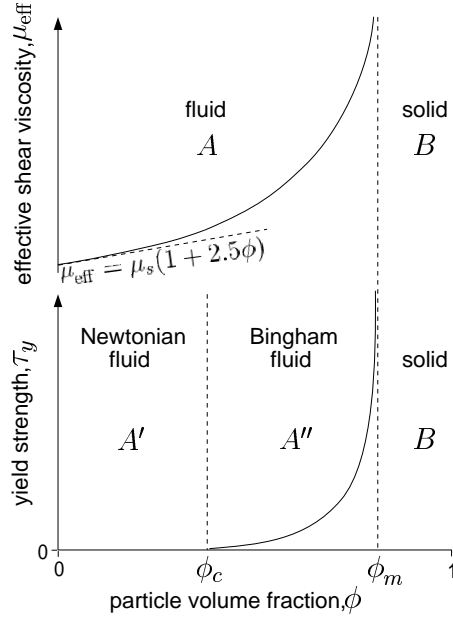


Figure 3.1. Sketch of the development of effective shear viscosity, μ_{eff} , and yield strength, τ_y , as a function of crystal fraction, ϕ . The critical crystal fractions ϕ_c and ϕ_m depend on the total shear stress, τ , and particle attributes, ξ , such as particle shape, size, and orientation distribution. A first minimum yield strength develops at $\phi_c \equiv \phi_c(\xi, \tau_y = 0)$ and increases with increasing ϕ . The fields A, A', A'', and B are explained in the text.

describing the effective shear viscosity, μ_{eff} , of a dilute ($\phi \leq 0.03$) suspension (left hand side of field A) of spheres for very low Reynolds numbers (Stokes flow). The viscosity of the suspending liquid is μ_s . The particle concentration, ϕ , has to be sufficiently low that hydrodynamic interactions of the particles can be neglected.

At higher ϕ (right hand side of field A) the so-called Einstein-Roscoe equation [88, 152, 168] is often employed to incorporate effects of hydrodynamically interacting, non-colloidal particles,

$$\mu_r = \mu_{\text{eff}}/\mu_s = (1 - \phi/\phi_m)^{-2.5}, \quad (3.2)$$

where ϕ_m is the maximum packing fraction. The form of Eq. (3.2) allows the relative

viscosity μ_r to diverge as $\phi \rightarrow \phi_m$. Eq. (3.2) is commonly used to calculate the viscosity of magmas [142]. However, the value of ϕ_m , which determines the transition to a solid, is uncertain; suggested values range from $\phi_m = 0.74$ [168] to $\phi_m = 0.60$ [115]. $\phi_m = 0.74$ corresponds to the maximum packing fraction of uniform spheres, so ϕ_m might be expected to be different if non-spherical particles are considered [115, 142]. An additional complication is the tendency of crystals to form aggregates or networks. Jeffrey and Acrivos [88] argue that a suspension that forms aggregates can be viewed as a suspension of single particles of new shapes (and sizes) and thus possessing different rheological properties.

3.2.2 Onset and development of yield strength - region A''

Suspensions may have a range of yield strengths τ_y (subregion A'') [210]. At ϕ_c a first sample-spanning crystal network forms to provide some minimum yield strength ($\tau_y \rightarrow 0$). For $\phi \geq \phi_c$ yield strength increases with increasing ϕ . The fluid-solid transition occurs at the maximum packing fraction, ϕ_m .

In general I expect ϕ_c and ϕ_m to depend on particle attributes (denoted ξ), such as particle shape, size, and orientation distribution, as well as on total applied stress, τ , i.e., $\phi_c \equiv \phi_c(\xi, \tau = 0)$ and $\phi_m = \phi_m(\xi, \tau)$. The dependence of ϕ_c and ϕ_m on τ results from hydrodynamic forces that can break and orient the crystal network and transform it into a more ordered state of denser packing. As τ_y approaches zero, the minimum critical crystal fraction, ϕ_c , is obtained for a given ξ . The development of yield strength, τ_y , may thus be described by

$$\tau_y(\phi) = [(\phi/\phi_c - 1) / (1 - \phi/\phi_m)]^{1/p} \tau_{co}, \quad (3.3)$$

where τ_{co} reflects the total interparticulate cohesion resisting hydrodynamic forces

and p may reflect the response of the aggregate state to shearing [202, 203, 210].

In this study I investigate the influence of ξ on ϕ_c as $\tau \rightarrow 0$, with the implication that the onset of zero-shear yield strength is a lower bound for the onset of yield strength in shear environments. Thus, ϕ_c may be viewed as the lowest crystal volume fraction at which τ_y could possibly form under the given assumptions (e.g., no non-hydrodynamic forces, bubbles, or Brownian motion).

3.3 Methods

In contrast to natural and analog experiments, computer models permit investigation of the formation of a continuous crystal network at low ϕ under static conditions (zero strain rate). As experimental and in situ measurements of yield strength may disrupt the fragile network that first forms at ϕ_c , it has been argued [10, 95] that incorrect extrapolation of stress versus strain rate measurements towards zero strain rate can lead to fictitious yield strength values when in actuality the suspension is shear-thinning. Moreover, simulations allow intergrowth of crystals, which is important for systems where crystal growth rate, G , is significantly larger than shear rate, $\dot{\gamma}$, as is the case in some natural systems [139, 140]. In this study I assume a zero-shear environment, thus

$$\frac{\dot{\gamma}}{G} \rightarrow 0. \quad (3.4)$$

I employ continuum percolation models (Chapter 2 and Saar and Manga [158]) to study the possible development of τ_y as a function of ϕ and ξ . Percolation theory describes the interconnectivity of individual elements in disordered (random) systems

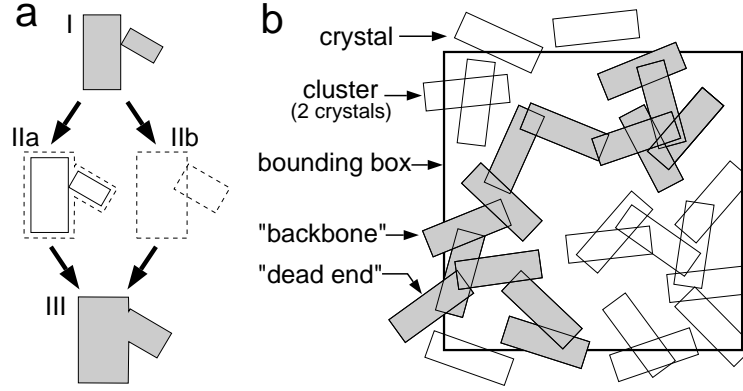


Figure 3.2. a) Simulation of crystal intergrowth. I) crystals touch; IIa) in natural systems under high growth rate to shear rate ratios, touching crystals grow together; IIb) in the computer model crystals overlap; III) same end result. b) Schematic 2-dimensional illustration of crystals forming clusters. One cluster connects opposite sides of the bounding box and forms the backbone. It is necessary that some crystals are positioned outside the bounding box, so that they can protrude into it. Actual simulations are 3-dimensional (Fig. 3.4).

and suggests a power law relationship of the form [181]

$$\tau_y \sim \begin{cases} 0 & \phi < \phi_c \\ (\phi - \phi_c)^\eta & \phi \geq \phi_c, \end{cases} \quad (3.5)$$

where ϕ_c is the percolation threshold which is reached when crystals first form a continuous phase across the suspending fluid. The exponent η describes the development of τ_y for $\phi \geq \phi_c$ close to ϕ_c . Although phenomenological, I determine a geometrical percolation threshold, p_c , and assume that it is related to ϕ_c [50]. With this approach, I can investigate the dependence of p_c on crystal shape, size, and orientation distribution and draw conclusions about the effects of these geometric properties on the development of yield strength.

The crystals in the simulations can be approximated as convex polyhedra of any shape, size, and orientation distribution in 3-dimensional space. Crystals are posi-

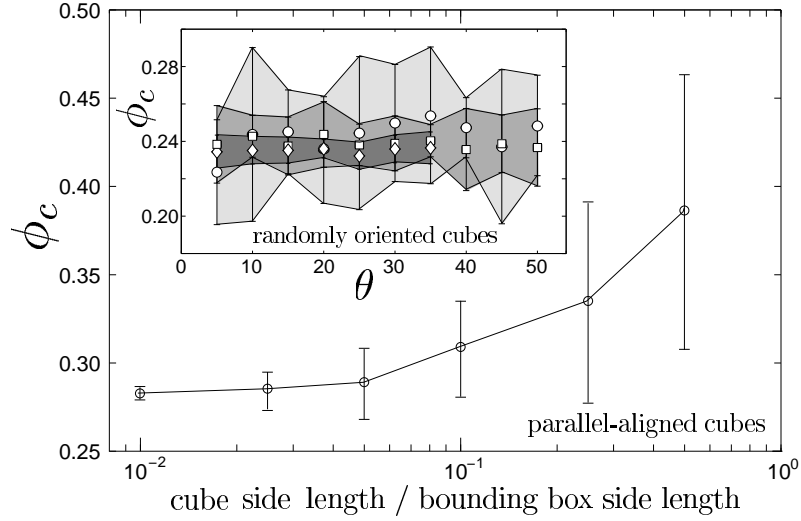


Figure 3.3. Critical crystal volume fraction, ϕ_c , versus ratio of cube side length, l_c , over bounding box side length, $l_b = 1$, for parallel-aligned cubes. Inset: ϕ_c versus number of resolution grains, θ , per distance from the crystal center to the farthest vertex, d , for randomly oriented cubes. Symbols are the mean and shaded areas indicate standard deviations. Circle (light gray area): $l_c/l_b = 0.1$; square (medium gray area): $l_c/l_b = 0.05$; diamond (dark gray area): $l_c/l_b = 0.025$. The total number of grains is $\theta_t \approx (\theta/d)^3$, where for a cube $d = (3l_c^2)^{1/2}$.

tioned randomly and interpenetrate each other (soft-core continuum percolation). In soft-core percolation the concept of maximum packing fraction, ϕ_m , does not apply. Fig. 3.2a shows that overlapping crystals of finite size may simulate crystal intergrowth in a zero-shear environment. Crystal orientation distribution is pre-assigned so that, for example, parallel-aligned or randomly oriented distributions can be simulated. Crystals are positioned inside and outside a bounding unit cube (Fig. 3.2b). To avoid finite size effects, the maximum length of the largest crystal in a given simulation is never longer than $1/10$, and typically $1/20$ to $1/40$, of the bounding cube side length. Fig. 3.3 shows the decrease in standard deviation and mean of ϕ_c for decreasing particle side length for parallel-aligned cubes.

I determine crystal overlaps analytically. Volume fractions, ϕ , are determined numerically by discretizing the bounding cube into subcubes (grains). The inset of Fig. 3.3 illustrates, that while crystal size influences the standard deviation of ϕ_c (gray shaded areas), “grain resolution,” θ , is relatively uncritical for calculations of ϕ . This insensitivity could be due to the angular crystal shapes that may be approximated well by a few angular grains. I also determine ϕ by using the number of crystals per unit volume, n , and the volume of a crystal, v , in $\phi = 1 - \exp(-nv)$ [6, 51] as previously introduced in Chapter 2 [Eq. (2.1)].

Crystals that overlap are part of a “cluster.” Overlapping crystals of different clusters cause the two clusters to merge into one. The percolation threshold is reached when a continuous crystal chain (hereafter referred to as the “backbone”) exists, connecting one face of the bounding cube with the opposing face (Figs. 3.2b, 3.4a). A backbone in this study includes the “dead-end branches” which may not be considered part of the backbone in other studies [181] (Fig. 3.2b).

All simulations are repeated at least 10 times to determine a mean and a standard deviation of ϕ_c . Standard deviations of ϕ_c are about 0.01. The typical number of crystals in each simulation ranges from 10^3 to 3×10^5 , depending on particle attributes ξ .

I test the computational method by running simulations for which percolation theory results are well-established [61, 141, 167, 176], such as for parallel-aligned cubes, where $\phi_c = 0.29$. Furthermore, I use visualizations of crystal configurations at low crystal numbers to confirm calculations of simulation parameters (Fig. 3.4).

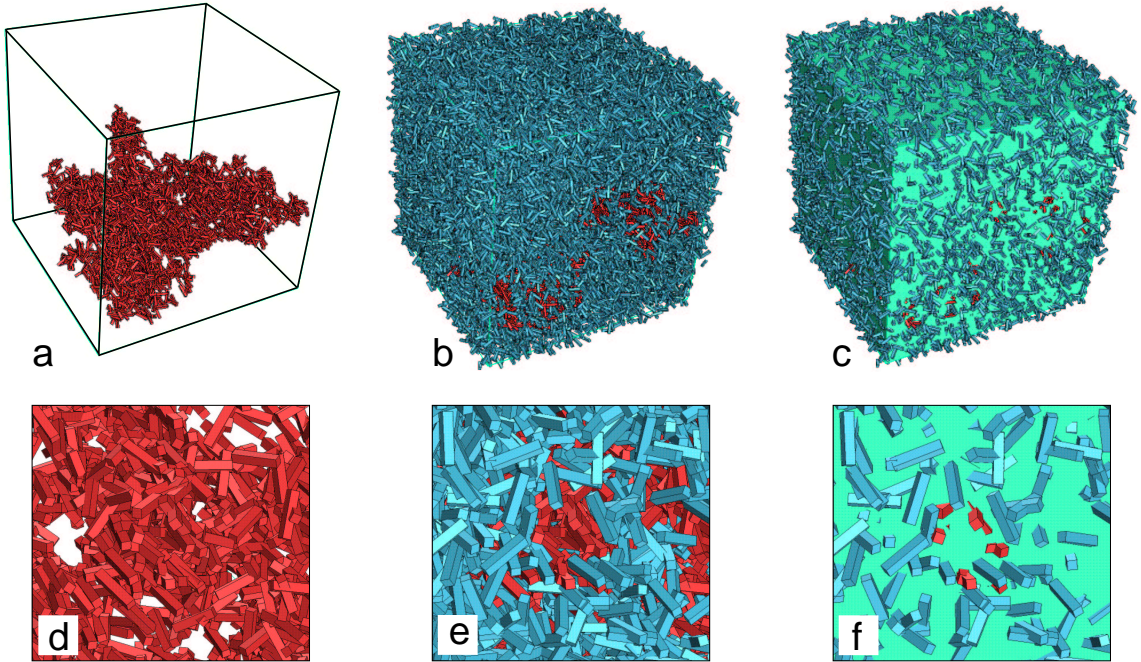


Figure 3.4. Visualizations of a simulation of randomly oriented elongated rectangular biaxial soft-core prisms of aspect ratio 5:1, at the percolation threshold; (a) only backbone crystals, connecting 4 of the 6 cube faces, (b) all crystals, (c) all crystals that protrude out of the bounding cube. Visualizations (d), (e), and (f) are magnifications of a region in visualizations (a), (b), and (c), respectively. The total crystal volume fraction in this simulation is $\phi_c = 0.132$ (backbone volume fraction: 0.016). The total number of crystals is 28373 of which 3400 are part of the backbone.

3.4 Results

Fig. 3.5 shows ϕ_c for biaxial rectangular prisms with aspect ratios ranging from 10^{-2} to 10^2 , where 10^0 indicates a cube, and negative and positive exponents indicate oblate and prolate prisms, respectively. All crystals are soft-core objects of uniform size and are oriented randomly. Standard deviations for ϕ_c are shown with vertical bars. A maximum $\phi_c = 0.22 \pm 0.01$ is reached for cubes with decreasing values of ϕ_c for less equant shapes. The dashed curve in Fig. 3.5 shows results from Garboczi et

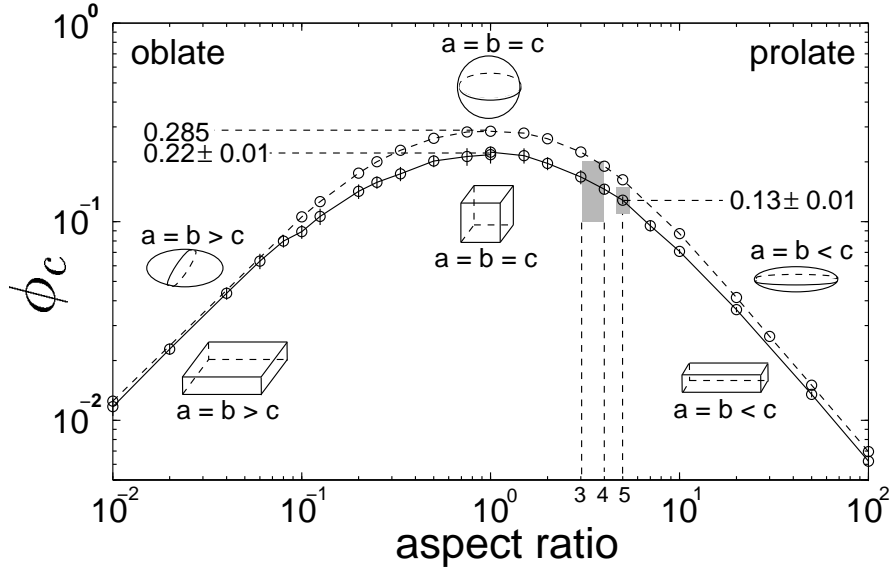


Figure 3.5. Simulation results of ϕ_c versus aspect ratio for randomly oriented biaxial soft-core rectangular prisms (solid curve, this study), compared with values for randomly oriented rotational soft-core ellipsoids (dashed curve) determined by [50]. Maximum values of $\phi_c = 0.22 \pm 0.01$ and $\phi_c = 0.285$ are reached for the most equant shapes, i.e., for cubes and spheres respectively. The number of crystals per simulation ranges from 4×10^2 to 8×10^4 (extreme prolate case). The standard deviation is shown with vertical bars. Two simulations, with 10 repetitions each, are performed for cubes, first with 401 ± 49 cubes and second with 2597 ± 128 cubes. Both simulations yield the same result, indicating that the larger cube size is sufficiently small to avoid finite size effects. The large and small shaded areas represent experimental results from Hoover et al. [70] and Philpotts et al. [140], respectively. This figure is equivalent to parts of Figure 2.4b

al. [50] for overlapping, randomly placed and randomly oriented, rotational ellipsoids. The general form of the two curves in Fig. 3.5 is the same, but the curves are offset for the more equant shapes. Both curves converge at the extreme prolate and oblate limits.

Results for triaxial soft-core rectangular prisms at random positions and orientations are shown in Fig. 3.6. Aspect ratios are given as short over medium and as long over medium axis for oblate and prolate prisms, respectively. Again, the uniaxial limit

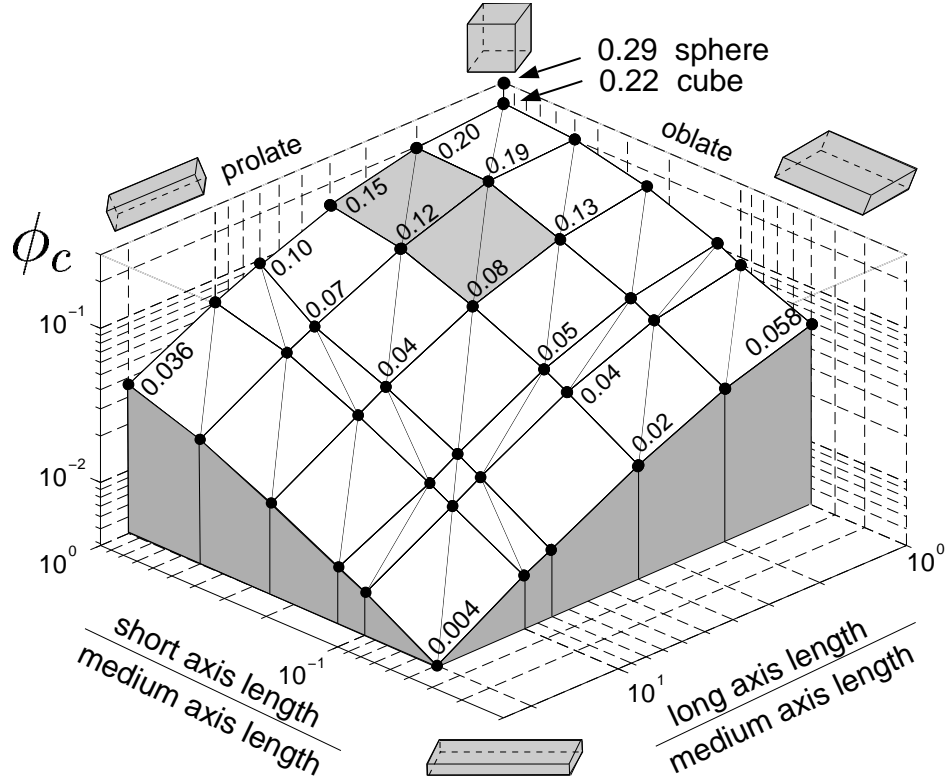


Figure 3.6. Simulation results of ϕ_c versus aspect ratio for randomly oriented triaxial soft-core rectangular prisms. A maximum value of $\phi_c = 0.22 \pm 0.01$ is reached for the most equant shape (cube). The gray shaded area indicates the range of aspect ratios for typical tabular plagioclase crystals [70, 140, 208].

and thus most equant shape (cube) provides the maximum value of $\phi_c = 0.22 \pm 0.01$. Deviation from an equant shape by either elongation or flattening causes a decrease in ϕ_c , with the largest combined decrease when all three axes have different lengths.

The effect of crystal size on the percolation threshold was examined by simulations involving bimodal size distributions. Fig. 3.7 shows ϕ_c versus occurrence fraction of large crystals in a bimodal size distribution of soft-core cubes. The volume of a large crystal is $V_{\text{large}} = 8V_{\text{small}}$, where V_{small} is the volume of a small crystal. For both parallel-aligned (solid line) and randomly oriented (dashed line) crystals, ϕ_c is

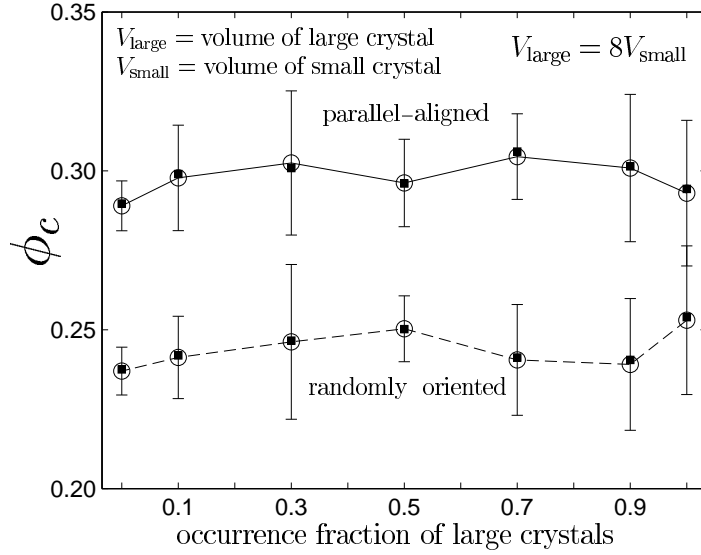


Figure 3.7. Critical crystal volume fraction, ϕ_c , versus occurrence fraction of large crystals in a bimodal size distribution. Crystals are parallel-aligned (solid line) and randomly oriented (dashed line) soft-core cubes. Open circles and error bars indicate numerical crystal volume fraction calculations using a space discretization method. Also shown are calculations of crystal volume fraction using the number of crystals, n , and the mean volume of the crystals, V_m , in $\phi = 1 - \exp(-nV_m)$ (filled squares). Error bars for the latter calculation of ϕ are comparable in size to the ones shown.

invariant (to within the standard deviation) of bimodal size distribution. Fig. 3.7 also shows good agreement between calculations of crystal volume fraction using the discretization approach (open circles) and using $\phi = 1 - \exp(-nV_m)$ [6, 51], where n is the number and V_m the mean volume of the crystals (solid squares).

3.5 Discussion

The onset of yield strength, τ_y , can be related to the formation of a continuous particle (or bubble) network that provides some resistance to applied stress [95, 210]. This particle network first forms at the percolation threshold, ϕ_c . No yield strength

is expected to exist for crystal volume fractions of $\phi < \phi_c$. Transitions in magmatic processes controlled by τ_y may thus not be expected to occur before ϕ has reached or exceeded ϕ_c . Therefore, the percolation threshold, ϕ_c , may be a crucial parameter in understanding the occurrence of transitions in magmatic flow and emplacement behavior.

Guéguen et al. [59] emphasize a necessary distinction between mechanical and transport percolation properties. They suggest that the effective elastic moduli of a material that contains pores and cracks is explained by “mechanical percolation.” In contrast, elastic moduli for media that contain particles with bond-bending inter-particle forces are probably described by the same percolation models that describe transport properties (permeability, conductivity) [59, 161]. Therefore, while rheological properties at critical melt fractions [147] probably belong to mechanical percolation that describes solid behavior, the networks of crystals that form solid bonds investigated in this study appear to be transport percolation problems.

In suspensions, τ_y may be created by friction, lubrication forces, or electrostatic repulsion between individual particles [101]. In addition, crystal-melt suspensions may provide τ_y by solid connections of intergrown crystals. I expect the latter to occur at lower ϕ and provide larger τ_y than friction. Therefore, I consider only the contribution of crystal network formation to τ_y .

3.5.1 Onset of yield strength

For randomly oriented biaxial soft-core prisms I obtain $0.01 < \phi_c < 0.22$ for oblate crystals with aspect ratios ranging from 0.01 to 1, and $0.006 < \phi_c < 0.22$ for prolate crystals with aspect ratios of 100 to 1, respectively (Fig. 3.5). Deviation from the uniaxial shape, a sphere for ellipsoids, or a cube for rectangular prisms, leads to a

decrease of ϕ_c (Fig. 3.5). The percolation threshold for spheres and parallel-aligned convex objects of any shape is $\phi_c \approx 0.29$ [61, 141, 167, 176]. When anisotropic particles are not perfectly aligned, ϕ_c depends on the orientation distribution of the objects [5, 8]. Randomly oriented cubes yield $\phi_c = 0.22 \pm 0.01$ in my simulations, a result that supports the predictions of Balberg et al. [5, 8]. Thus, the onset of yield strength is a function of both shape (Fig. 3.5) and the degree of randomness in the particle orientation, with τ_y occurring at lower ϕ for more elongated or flattened shapes, as well as for more randomly oriented objects. While it is well-established that size heterogeneity of non-overlapping particles, for example in sediments, increases the maximum packing fraction, size heterogeneity of overlapping objects does not appear to influence ϕ_c , as shown in Fig. 3.7. Therefore, onset of yield strength should not change with size variations of crystals.

Philpotts et al. [139, 140] observe a crystal network in the Holyoke flood basalt at total crystal volume fractions of about 0.25. Based on 3D imaging of the crystals using CT scan data, they conclude that plagioclase (aspect ratio 5:1) forms the crystal network, although it comprises only half of the total crystal volume fraction (≈ 0.13). My results show that the formation of a continuous network of randomly oriented plagioclase crystals of aspect ratio 5:1 at $\phi_c \approx 0.13$ is expected on a purely geometrical basis and thus show good agreement with the experimental results (dashed line at aspect ratio 5 in Figure 3.5). Because the elongated plagioclase crystals form a network at lower ϕ_c than the more equant (cube-like) pyroxenes, it may be reasonable, as a first approximation, to model crystal-network formation in this plagioclase-pyroxene system with plagioclase crystals only.

Typical plagioclase shapes may be approximated as triaxial polyhedra that are elongated and flattened (tablets). Fig. 3.6 shows that, for random orientations, the

combined effect of three independent axis lengths in rectangular prisms reduces ϕ_c further with respect to biaxial prisms. The shaded area in Fig. 3.6 indicates the range of rectangular prism shapes that best approximate typical plagioclase crystals [70, 140, 208]. These plagioclase tablets of aspect ratios (short:medium:long) 1:4:16 to 1:1:2 yield $0.08 < \phi_c < 0.20$, respectively, in my simulations. Therefore, under the condition of random crystal orientation, i.e., in a zero-shear environment, I expect typical plagioclase tablets to form a first fragile crystal network at crystal volume fractions as low as 0.08 to 0.20, where the particular values depend on the crystal aspect ratios.

My results also agree reasonably well with Hoover et al.’s [70] analog experiments with prismatic fibers in corn-syrup, in which $0.10 < \phi_c < 0.20$ for aspect ratios 3 to 4 (gray shaded area in Fig. 3.5). However, the particles in the experiment are non-overlapping, not soft-core as in my simulations, and thus I expect some deviation from the numerical results. In the same study Hoover et al. [70] conduct partial melting experiments with pahoehoe and ‘a‘a samples from Hawai‘i and Lava Butte, Oregon, respectively. Partially melted pahoehoe samples with subequal amounts of plagioclase and pyroxene show some finite yield strength, and thus the sample maintains its cubical shape, at volume fractions of 0.35 at a temperature of 1155 °C. At 1160 °C and volume fractions of 0.18, the sample collapses, indicating that the yield strength dropped below the total stress of about 5×10^2 Pa applied by gravitational forces. Backscattered electron images indicate that plagioclase and pyroxene form local clusters and a sample-spanning cluster network at 1155 °C (Fig. 3.8). Cluster formation suggests that crystal configurations in the pahoehoe sample may be dominated by nucleation site effects, possibly due to rapid cooling [97]. If I determine the average of the reported median plagioclase aspect ratio of about 1:2:5 and the estimated median pyroxene aspect ratio of 1:1:2, I obtain an aspect ratio of about

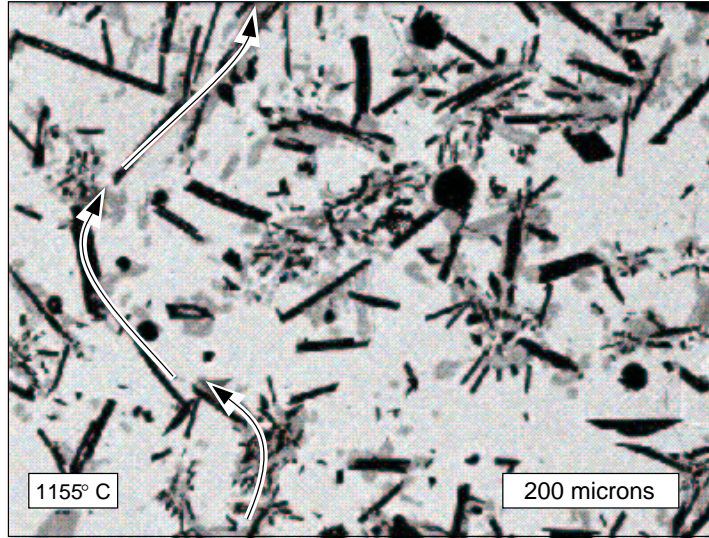


Figure 3.8. Backscattered electron image of a pahoehoe sample from Hawai'i close to the percolation threshold after partial melting experiments [70]. An image-spanning crystal pathway (arrows) formed of plagioclase (black) and pyroxene (gray) crystals can be observed.

1:1.5:3.5 (volume fractions are about equal). For this aspect ratio and random orientation, neglecting clustering effects visible in the experiments, my simulations suggest $\phi_c \approx 0.18$ (Fig. 3.6).

Hoover et al. [70] also carried out melting experiments with 'a'a samples from Lava Butte in Oregon, containing mainly plagioclase, with only minor pyroxene (volume fraction < 0.05). The plagioclase crystals show some local alignment and exhibit a small τ_y for a plagioclase volume fraction of 0.31 at 1142 °C, where the sample shape is preserved, but not at 0.26 at 1150 °C, where the sample collapses. The plagioclase aspect ratio is about 1:2:5 for which my simulations suggest $\phi_c \approx 0.16$. However, as discussed previously, alignment of crystals causes an increase of ϕ_c , where the upper bound $\phi_c = 0.29$ is reached for parallel-aligned objects of any convex shape.

The general trend of my simulations and other percolation threshold studies ap-

appears to be consistent with experiments presented by Hoover et al. [70] and agrees well with experiments presented by Philpotts et al. [139, 140] (Fig. 3.5). The drastic decrease in ϕ_c I observe with increasing particle shape anisotropy and increasing randomness in particle orientation is consistent with other numerical, experimental, and theoretical studies [6, 27, 59, 124, 156, 157] that investigate the formation of continuous object networks.

3.5.2 Scaling relation for $\tau_y(\phi)$ curves of differing particle shapes, and other generalizations

To develop general rules that explain the dependence of the geometrical percolation threshold, p_c , on object geometries I consider two percolation theory concepts (Chapter 2 and Saar and Manga [158]). First is the average critical number of bonds per site at p_c , B_c . Second is the excluded volume, v_{ex} , which is defined as the volume around an object in which the center of another such object cannot be placed without overlap. If the objects have an orientation or size distribution, the average excluded volume of an object is averaged over these distributions and denoted by $\langle v_{ex} \rangle$ and the average critical total excluded volume is given by $\langle V_{ex} \rangle = n_c \langle v_{ex} \rangle$ [8], where n_c is the number of soft-core particles at the percolation threshold. Balberg et al. [8] find that B_c is equal to $\langle V_{ex} \rangle$, i.e.,

$$B_c = n_c \langle v_{ex} \rangle = \langle V_{ex} \rangle, \quad (3.6)$$

equivalent to Eq. (2.8), and suggest that $\langle V_{ex} \rangle$ is invariant for a given shape and orientation distribution and thus independent of size distribution [5]. Values of $\langle V_{ex} \rangle$ are highest for spheres and parallel-aligned convex objects of any shape, where $\langle V_{ex} \rangle = 2.8$, lowest for orthogonally-aligned (macroscopically isotropic) widthless sticks where $\langle V_{ex} \rangle = 0.7$, and intermediate for randomly oriented cylinders, for which $\langle V_{ex} \rangle =$

1.4 [5]. In natural systems particles can be oriented between random and parallel, depending on the shear stress tensor and particle shapes [110, 194], and thus I expect $\langle V_{ex} \rangle$ to fall within the bounds of 1.4 and 2.8. Therefore, $\langle V_{ex} \rangle$ probably varies by a factor of 2 in natural systems.

Shante and Kirkpatrick [167] found $p_c = 1 - \exp(-B_c/8)$ for parallel-aligned convex objects in continuum percolation. Using Eq. (3.6) and $\langle v_{ex} \rangle = 8v$ for spheres (and parallel-aligned convex objects in general), where v is the volume of the sphere, it is possible to make further generalizations. At the percolation threshold, where $n = n_c$, $B = B_c$, and $\phi = p_c$, Eq. (3.6) is substituted into $\phi = 1 - \exp(-nv)$ [6, 51] to yield

$$p_c = 1 - \exp(-B_c v / \langle v_{ex} \rangle) \quad (3.7)$$

for systems containing interpenetrating objects of any convex shape. Eq. (3.7) and $B_c = \langle V_{ex} \rangle = 2.8$ for spheres agree well with the established percolation threshold $p_c = 0.29$ for soft-core spheres [141]. Soft-core parallel-aligned convex shapes also yield $p_c = 0.29$ [61]. Because the ratio of $v / \langle v_{ex} \rangle$ is constant for objects of different sizes and identical shape and orientation distributions, p_c may be expected to be invariant if only the size distribution changes. This expectation is confirmed in my simulations (Fig. 3.7).

Generalization of a relationship between p_c , $\langle V_{ex} \rangle$, n_c , and v to include variations in object shapes have been less successful. Garboczi et al. [50] investigate a number of possible shape functionals for randomly oriented soft-core rotational ellipsoids, including $\langle V_{ex} \rangle$. They find that $n_c \langle v_{ex} \rangle \approx 1.5$ and 3.0 for extremely prolate and oblate rotational ellipsoids, respectively, which agrees reasonably well with the range of 1.4 (randomly oriented widthless sticks) to 2.8 (spheres) suggested by Balberg [5]. Similar results for the other shape functionals lead Garboczi et al. [50] to conclude

that simple shape functionals do not produce invariants and thus cannot predict p_c for overlapping rotational ellipsoids.

Drory [39] also concluded that the total average excluded volume is not truly universal, but is influenced instead by the shape of objects “in a complicated way.” However, Drory et al. [41] point out that $\langle V_{ex} \rangle$ “seemed to be relatively insensitive to the shape of particles” when compared with p_c and that “it was therefore considered an approximately universal quantity.” A more rigorous theoretical model is developed to explain values of $B_c = \langle V_{ex} \rangle$ for interacting objects of different shapes [39, 40, 41]. While this theory predicts B_c well it does not provide an alternative to B_c that would be a true invariant.

Based on the above studies, I have to content myself with $\langle V_{ex} \rangle$ as an approximate invariant that varies by a factor of 2. Predictions of ϕ_c to within a factor of 2 should thus be possible for a large range of particle shapes [27]. In geological applications, a factor of 2 uncertainty in ϕ_c may be too large to interpret some observations, but may still be a valuable constraint for developing models and predictions.

For the case of randomly oriented rods with hemispherical caps of length $L + W$ and width W [8],

$$\langle v_{ex} \rangle = (4\pi/3)W^3 + 2\pi W^2L + (\pi/2)WL^2. \quad (3.8)$$

For $L \gg W$, Eq. (3.8) reduces to that of Onsager [135],

$$\langle v_{ex} \rangle \approx (\pi/2)WL^2. \quad (3.9)$$

Because the calculation of an average excluded volume for randomly oriented rectangular prisms is difficult, I define a volume $v^* = (4/3)\pi r_1 r_2^2$ that scales in a similar manner to Eq. (3.9). Here, r_1 is the distance from the center to the closest

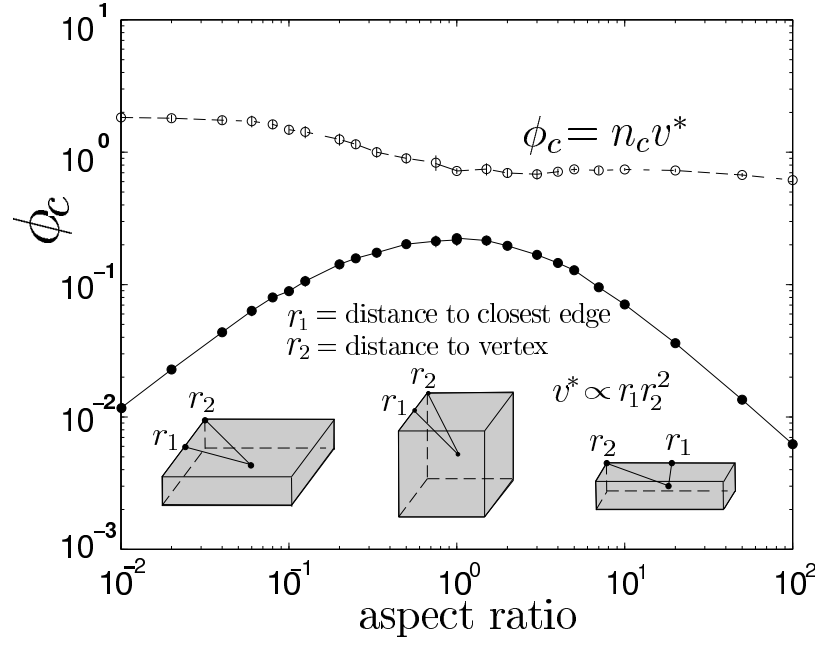


Figure 3.9. The volume $v^* = (4/3)\pi r_1 r_2^2$ scales in a similar manner to the average excluded volume (Eq. 3.9). I normalize v^* by the number of particles, n_c , at the percolation threshold.

edge and r_2 is the distance to a vertex (Fig. 3.9). When I normalize v^* by the critical number of crystals per unit volume, n_c , I obtain a quasi-invariant, $n_c v^*$. In the asymptotic limits of large and small aspect ratios $n_c v^*$ varies by about a factor of 3 (Fig. 3.9). The relatively small variations of $n_c v^*$ compared with ϕ_c suggests that $n_c v^*$ may be considered a reasonable estimate of a characteristic normalized volume.

If $n \langle v_{ex} \rangle$ were truly invariant, and could be applied to conditions of $\phi \neq \phi_c$ and non-overlapping (hard-core) particles, I could relate the volume fraction for particles of general shape and volume, V , to the volume fraction, ϕ_{eq} , of an equivalent object (here a sphere) by

$$\phi_{eq} = \frac{\phi_g \langle v_{ex} \rangle_g}{8V_g}, \quad (3.10)$$

where the subscript g denotes values for general particle shapes. For Eq. (3.10), I

use $\phi = nV$ (for hard-core particles). Similarly, for soft-core particles, where $\phi = 1 - \exp(-nV)$, I obtain the relationship

$$\phi_{eq} = 1 - (1 - \phi_g)^{\frac{\langle v_{ex} \rangle_g}{8V_g}}. \quad (3.11)$$

Because $n_c \langle v_{ex} \rangle$ varies by a factor of about 2, scaling in Eqs. (3.10-3.11) is accurate to a factor of about 2.

As an example, I use Eqs. (3.8) and (3.10), and $L = 2.5W$ for hard-core fibers of mean aspect ratio 3.4:1 [70] to calculate that $\phi_{eq} = 1.5\phi_g$. I may then use this scaling relation of 1.5 to scale experimentally measured $\tau_y(\phi)$ curves for these fibers to the values of the equivalent object (sphere). The two curves shown in Fig. 3.10 can be superimposed using $\phi_{eq} = 2.2\phi_g$. The factor 2.2 is greater than my estimated value of 1.5 by a factor of 1.5, and within the anticipated uncertainty range of a factor of 2.

An equivalent way of interpreting the experimental results is to determine the average excluded volume, $\langle v_{ex} \rangle$. My result of $\phi_{eq} = 1.5\phi_g$ implies that $\langle v_{ex} \rangle = 12V_g$ for the hard-core fibers. I now use $\langle v_{ex} \rangle = 12V_g$ together with the computed number of crystals at the percolation threshold, n_c . For biaxial randomly oriented prisms of aspect ratio 3:1 and a normalized particle volume of 1.7×10^{-6} , simulations yield $n_c = 113 \times 10^3$ which results in $n_c \langle v_{ex} \rangle = 2.3$. The average total excluded volume thus falls within the expected range of 1.4 to 2.8 for particle shape and orientation distributions in natural systems.

3.5.3 Implications

Possible implications of the development of yield strength in crystal-melt suspensions include transitions in surface textures of basaltic lava flows [26], melt extrac-

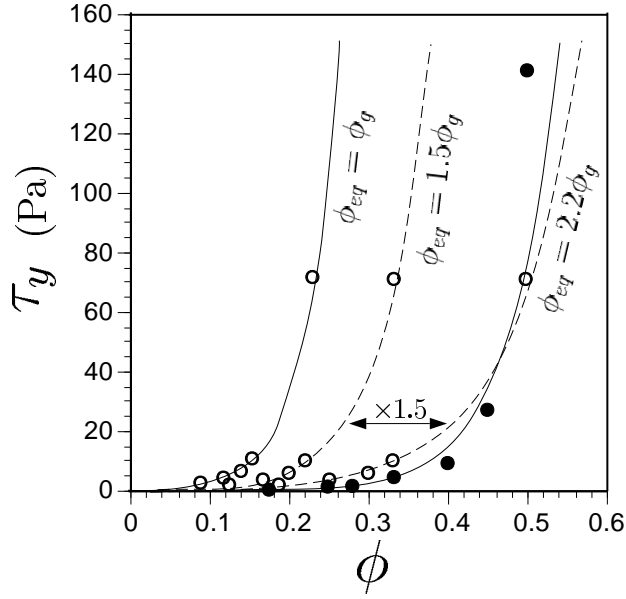


Figure 3.10. Scaling of an experimental $\tau_y(\phi)$ curve for fibers of aspect ratio 3.4:1 (open symbols along solid line) to the experimental $\tau_y(\phi)$ curve for spheres (filled symbols); data are from [10]. Dashed lines indicate scaled curves for the fibers using the scaling constants 1.5 and 2.2.

tion from crystal mushes [140], transitions from effusive to explosive volcanism [35], and propagation of shear waves through zones of partial melting [11]. Furthermore, the characteristics of mineral textures and the spatial distribution of ore deposits in komatiites are sometimes explained by fluid dynamical models that suggest post-emplacement convection [75, 193]. Aggregate and network formation of dendritic olivine crystals in komatiites increases viscosity and may provide yield strength, which would reduce the convective vigour and may potentially suppress convection. In general, the development of yield strength is likely to affect convective processes in a variety of geologic settings including lava lakes, flood basalts, and magma chambers. Finally, loss of a rigid crystal framework may be a necessary condition for some geologic processes to occur. For example, diapiric ascent of magma through the crust

[116] or thorough mixing of partially solidified material into an intruding melt [125] may require loss of continuous crystal networks.

3.6 Conclusions

I employ numerical simulations for soft-core (overlapping) rectangular prisms to determine the critical crystal volume fraction, ϕ_c , at which a suspension may develop a finite yield strength, τ_y . My results indicate that ϕ_c is a function of both shape and the degree of randomness in particle orientations. In general, the onset of τ_y should occur at lower crystal volume fractions for larger shape anisotropy, as well as for more randomly oriented objects.

Formation of a sample-spanning network of randomly oriented plagioclase crystals of aspect ratio 5:1 is expected at $\phi_c \approx 0.13$ and thus confirms experimental observations [139, 140]. In general, under random orientations, for typical plagioclase aspect ratios ranging from 1:4:16 to 1:1:2 I expect $0.08 < \phi_c < 0.20$, respectively. Randomly oriented crystals that have larger aspect ratios may exhibit yield strength at even lower crystal volume fractions. Therefore, the development of yield strength may occur at lower crystal volume fractions than the 0.35-0.5 commonly assumed [95, 103, 142], provided the crystals are anisotropic in shape and exhibit random orientations, as can be the case in low-shear environments.

For overlapping (soft-core) particles, ϕ_c increases with the degree of alignment and reaches a maximum of $\phi_c = 0.29$, the value for spheres, for parallel-aligned particles of any convex shape. This dependence of ϕ_c on the particle orientation distribution suggests that the flow regime, and therefore the resulting particle ordering, of a suspension is an important parameter in defining ϕ_c and hence the onset of yield

strength. In contrast, crystal size distributions are not expected to influence ϕ_c unless crystal overlap is inhibited. The presented results of ϕ_c in a zero-shear environment may be viewed as a lower bound for the onset of yield strength in shear environments.

Phenocryst volume fractions larger than 0.30 [195] and even 0.50 [115] have been reported for dikes. My results suggest that a first minimum yield strength ($\tau_y \rightarrow 0$) may develop at much lower volume fractions and potentially impede magma flow. Suppression of flow under high shear stresses, however, requires ϕ larger than about 0.5 [96]. Thus, it should be emphasized that even for $\phi > \phi_c$, flow can occur if stresses exceed the yield strength.

Finally, I confirm that the average total excluded volume $n \langle v_{ex} \rangle$ is a quasi-invariant that varies by only a factor of about 2 over a large range of shapes and I suggest that it provides a reasonable means to define an equivalent volume fraction, ϕ_{eq} . ϕ_{eq} captures the characteristic particle geometry that determines onset of ϕ_c and may also be applied to $\phi \neq \phi_c$. Using ϕ_{eq} for all ϕ appears to allow scaling of experimental $\tau_y(\phi)$ curves [70] for suspensions of different particle shapes to within a factor of 2.

Chapter 4

Hydroseismicity

This chapter is largely based on Saar and Manga [159]¹.

4.1 Introduction

Natural or artificial changes in pore-fluid pressure may trigger earthquakes, a process hereafter referred to as hydroseismicity. Examples include hydroseismicity induced by reservoirs [60, 173, 187], by fluid injection into [67, 71, 144, 145, 150], or withdrawal from [163, 164, 213] aquifers or oil reservoirs, or by pore-fluid pressure changes induced by other earthquakes [72, 133]. It has also been suggested that hydroseismicity may be caused by changes in groundwater recharge rates [30, 153, 205] which can be the result of seasonal snow melt or variations in precipitation [90, 100, 134, 205]. In this study I use signal processing techniques to investigate whether natural groundwater recharge variations trigger some earthquakes in the Cascade

¹Reprinted from Earth and Planetary Science Letters, Vol. 214, Saar, M. O., and M. Manga, Seismicity induced by seasonal groundwater recharge at Mt. Hood, Oregon, 605-618, Copyright (2003), with permission from Elsevier.

volcanic arc, U.S.A.

The Cascade arc is located on a tectonically active, and in parts densely populated, convergent plate boundary. Thus, for both seismic and volcanic hazard assessment it is important to discern triggers of earthquakes as tectonic, magmatic, or hydrologic. Moreover, rapid groundwater recharge may initiate larger (local magnitude, $M_l > 3$) earthquakes on critically stressed faults [212]. More generally, understanding the causes of hydroseismicity may provide additional insight into seismic hazards associated with reservoir impoundment or injection of fluids into the subsurface for example during waste fluid injection, carbon sequestration, and geothermal energy exploration. Detection of natural groundwater-recharge-induced earthquakes also provides a baseline against which reservoir- or fluid-injection-induced seismicity can be measured to evaluate the actual extent of human-caused hydroseismicity. Moreover, natural hydrologic triggering of earthquakes provides insight into the state of stress in the crust. In addition to tectonic information, the time lag between groundwater recharge and earthquakes allows me to determine hydraulic properties of the upper crust on spatial and temporal scales that are relevant for studies of regional hydrogeology.

Figure 4.1a shows seismicity at Mt. Hood, Oregon, a Quaternary stratovolcano, for the period from February 4th 1980 through July 11th 2002. Earthquakes occur preferentially on the southern flanks of the volcano. The offaxis concentration suggests the possibility that earthquakes are not all caused directly by magma flow although offcentered magma-related seismicity can occur when volcanic conduits are inclined. Instead, I hypothesize that at least some seismicity could be triggered by seasonal groundwater recharge that changes pore-fluid pressures on preexisting critically stressed faults. I select a region of concentrated off-axis seismicity (large open square in Figure 4.1a) to test this hypothesis.

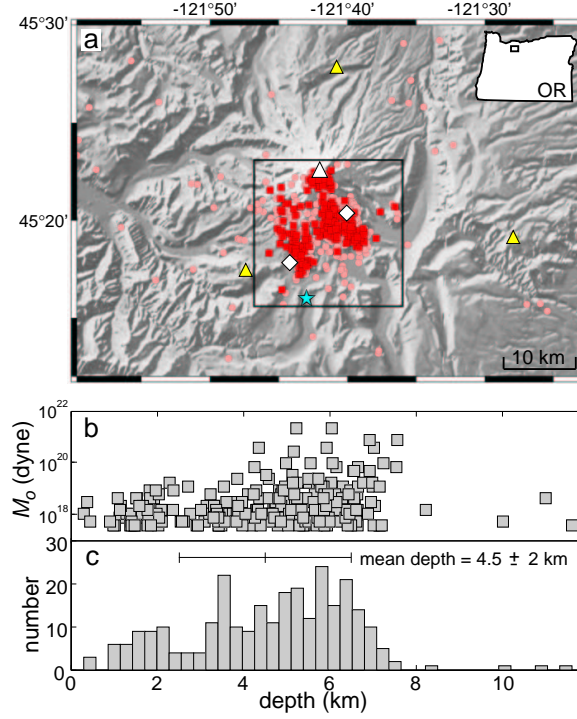


Figure 4.1. a) Shaded relief map of Mt. Hood, Oregon indicating all earthquakes (pink circles and red squares) and selected (for criteria see text) earthquakes (red squares), stream discharge gauging station on Salmon River (blue star), summit of Mt. Hood (large white triangle), and hydrothermal Swim Warm Springs (western white diamond) and Meadows Spring (eastern white diamond). Three (small yellow triangles) out of fourteen relevant seismometers (Appendix A.1) are located within the map region. b) Seismic moment, M_o , versus earthquake depth. c) Histogram of earthquake depths, mean earthquake depth (4.5 km), and range of 1σ -standard deviation (2 km).

4.2 Data and analysis

The 1980 Mount St. Helens eruption increased monitoring efforts at volcanos in the Cascade range. As a result, the Pacific Northwest Seismic Network (PNSN) has maintained short-period vertical-motion seismometers around Mt. Hood since the mid-1980s (Appendix A.1). To reduce instrumentation bias I only use earthquakes with a minimum local magnitude of $M_l = 1$ (Figure 4.2), above which $b \approx -1$ holds

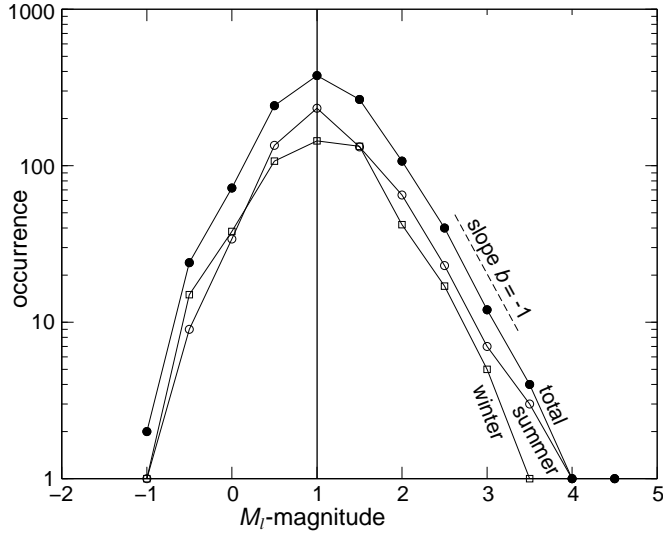


Figure 4.2. Earthquake magnitude, M_l , binned in half-magnitude increments, versus logarithmic frequency of occurrence (Gutenberg-Richter relationship) for all earthquakes displayed in Figure 4.1. Open circles, squares, and solid circles indicate seismicity during the summer ($15 \leq \text{week} \leq 40$, open circles) and winter ($\text{week} \geq 41$ or $\text{week} \leq 14$, open squares), and total years, respectively. Above the cut-off magnitude of $M_l = 1$ the decrease in seismicity with increasing magnitude follows approximately the expected slope of $b = -1$. This suggests that the data set is complete for $M_l \geq 1$.

in the Gutenberg-Richter [102] relationship,

$$\log_{10} N = a + bM_l, \quad (4.1)$$

where N is the number of earthquakes of magnitude M_l and a is the production of seismicity. Seismic moment, M_o , is approximated by [102]

$$M_o = 10^{1.5(M_w + 10.73)}, \quad (4.2)$$

where I assume $M_w \approx M_l$ due to the small earthquake magnitudes of $M_l \leq 4.5$.

Groundwater recharge at Mt. Hood is largely due to spring snow melt which provides a natural pore-fluid pressure signal of narrow temporal width and potentially relatively large amplitude. Groundwater recharge may be approximated by

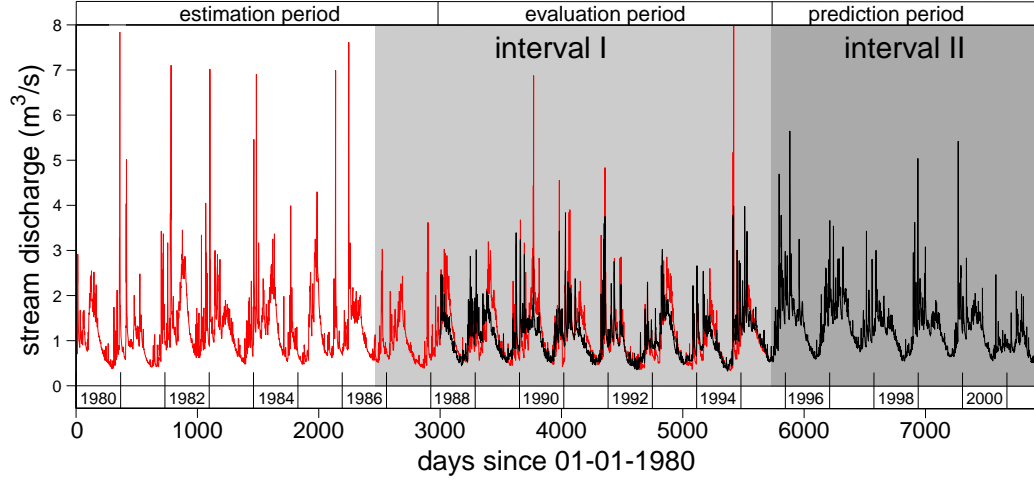


Figure 4.3. Stream discharge of Salmon River, Oregon, measured at USGS gauging station 14134000 (red curve) located at an elevation of 1050 m. During the estimation period, a transfer function between Hood River and Salmon River is determined using a Box-Jenkins [21] method (Appendix A.2). The evaluation period shows the fit between predicted (black) and actual (red) data. The prediction period shows the estimated discharge for Salmon River. Intervals I and I+II are used in the analysis and are discussed in the main text.

hydrographs of surface-runoff dominated streams at high elevations, such as Salmon River, that show a peak in discharge during snow melt [108] (Figure 4.3). Groundwater recharge may be delayed from stream discharge due to flow in the unsaturated zone. This possible delay is not considered here but may be neglected considering the uncertainty in earthquake depth discussed later.

Salmon River at USGS gauge 14134000 (blue star in Figure 4.1) has a 21 km² drainage area. Gauge elevation is 1050 m. Stream discharge for Salmon River is only available through September 30th 1995. Thus, I determine a transfer function between stream discharge of Hood River (USGS gauge 14120000) and Salmon River using a Box-Jenkins [21] method (Appendix A.2). Discharge at Hood River is available until September 30th 2001 and is convolved with the transfer function to extend the

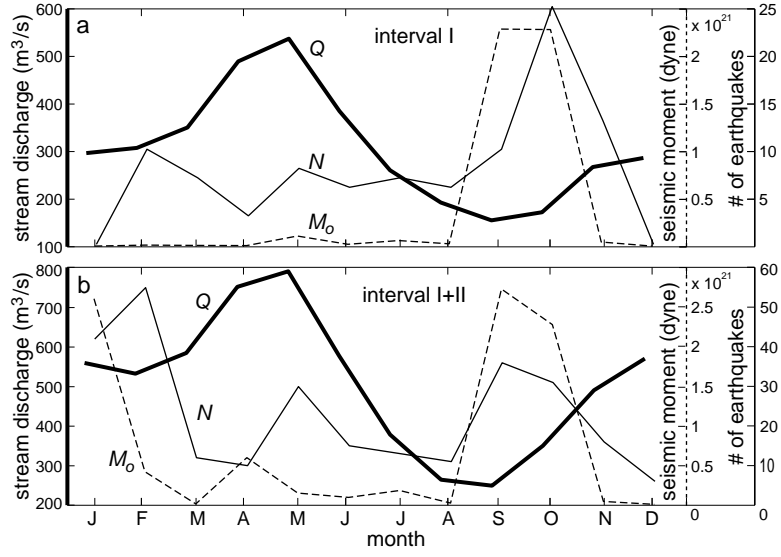


Figure 4.4. Monthly binned histograms showing cumulative mean daily stream discharge (bold solid line), cumulative number of earthquakes (thin solid line), and cumulative seismic moment (thin dashed line) for a) interval I and b) interval I+II.

discharge data to that date (Figure 4.3).

For this analysis I distinguish two time intervals. Interval I has a lower bound on October 1st, 1986, i.e., at the beginning of the water year when most seismometers had been installed. The upper bound of interval I is set to the last available discharge date for Salmon River, September 30th 1995. Interval II starts on October 1st 1995 and ends when discharge measurements at Hood River were discontinued on September 30th 2001 (Figure 4.3). Therefore, my analysis focuses on interval I, to allow evaluation of the best-constrained data, and on the combined interval I+II, to investigate the longest possible time series.

Figure 4.4a and b show histograms for stream discharge, Q , number of earthquakes, N , and seismic moment, M_o , binned monthly for intervals I and I+II, respectively. Elevated levels of stream discharge exist from November through June

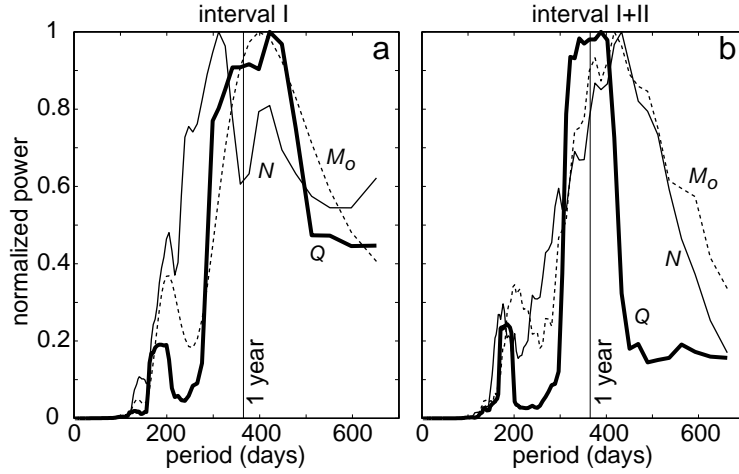


Figure 4.5. Period content of time series. Ten-day running average power spectra, normalized by their respective maximum power, of stream discharge, Q (bold solid line), number of earthquakes, N (thin solid line), and seismic moment, M_o (thin dashed line). Dominant periods around one year occur for both interval I (a) and interval I+II (b).

with a peak in May due to snow melt. Number of earthquakes and total seismic moment show a peak during September and October for both intervals I and I+II. In addition, interval I+II shows seismicity in January and February. For interval I, the time lag between peak stream discharge, a proxy for groundwater recharge, and seismicity is about 5 months. To test whether Q , N , and M_o have yearly periodicity, I determine their power spectra which indeed show dominant periods of about one year (Figure 4.5) for both intervals I and I+II.

Rather than using monthly-binned data averaged over all years from Figure 4.4 to determine cross correlation coefficients, I use the actual time series at a resolution of one day. Seismicity is binned to yield daily number of earthquakes, N , and total daily seismic moment, M_o . Next, I apply moving least-squares polynomial fits (Appendix A.3) of order ≤ 5 to Q , N , and M_o (Figure 4.6), resulting in the interpolated

time series denoted \overline{Q} , \overline{N} , and $\overline{M_o}$, respectively. This type of interpolation assures that the data is optimally matched in a least-squares sense and that later determination of cross-correlation coefficients between time series are based on equivalent frequency bands. Moreover, interpolation of N and M_o provides evenly-spaced data allowing for standard spectral analysis techniques. For better temporal comparison, the interpolated data from Figure 4.6 (black curves) are shown normalized by their respective maximum values in Figure 4.7.

For a lead channel f and a lag channel g , the normalized cross ($f \neq g$) and auto ($f = g$) correlation coefficients, $\Phi_{fg}(t)$, at a time lag of t , are given by

$$-1 \leq \Phi_{fg}(t) = \frac{\phi_{fg}(t)}{\sqrt{\phi_{ff}(0)}\sqrt{\phi_{gg}(0)}} \leq 1, \quad (4.3)$$

where

$$\phi_{fg} = \int_{-\infty}^{\infty} f(\tau)g(t + \tau)d\tau. \quad (4.4)$$

The normalization assures that perfect correlation, no correlation, and perfect anti-correlation, are indicated by values of 1, 0, and -1, respectively.

I determine normalized unbiased cross-correlation coefficients, $\Phi_{\overline{QN}}$ and $\Phi_{\overline{QM_o}}$ (Figure 4.8) for the time series. Cross-correlations show statistically significant peaks at 151 days that are distinct from 99% confidence intervals for random earthquake distributions (Appendix A.4).

To reduce possible dominance by a year with exceptionally high seismicity, I also determine moving normalized unbiased cross-correlation coefficients, $\overline{\Phi}_{fg}$, on overlapping segments within each time series (Appendix A.4). The segment width is 3 years with 30 days shift after each cross-correlation calculation resulting in 75 and 109 segments for intervals I and I+II, respectively. For each segment 20 repetitions are performed so that a total of over 1000 and 2000 iterations are used to determine the

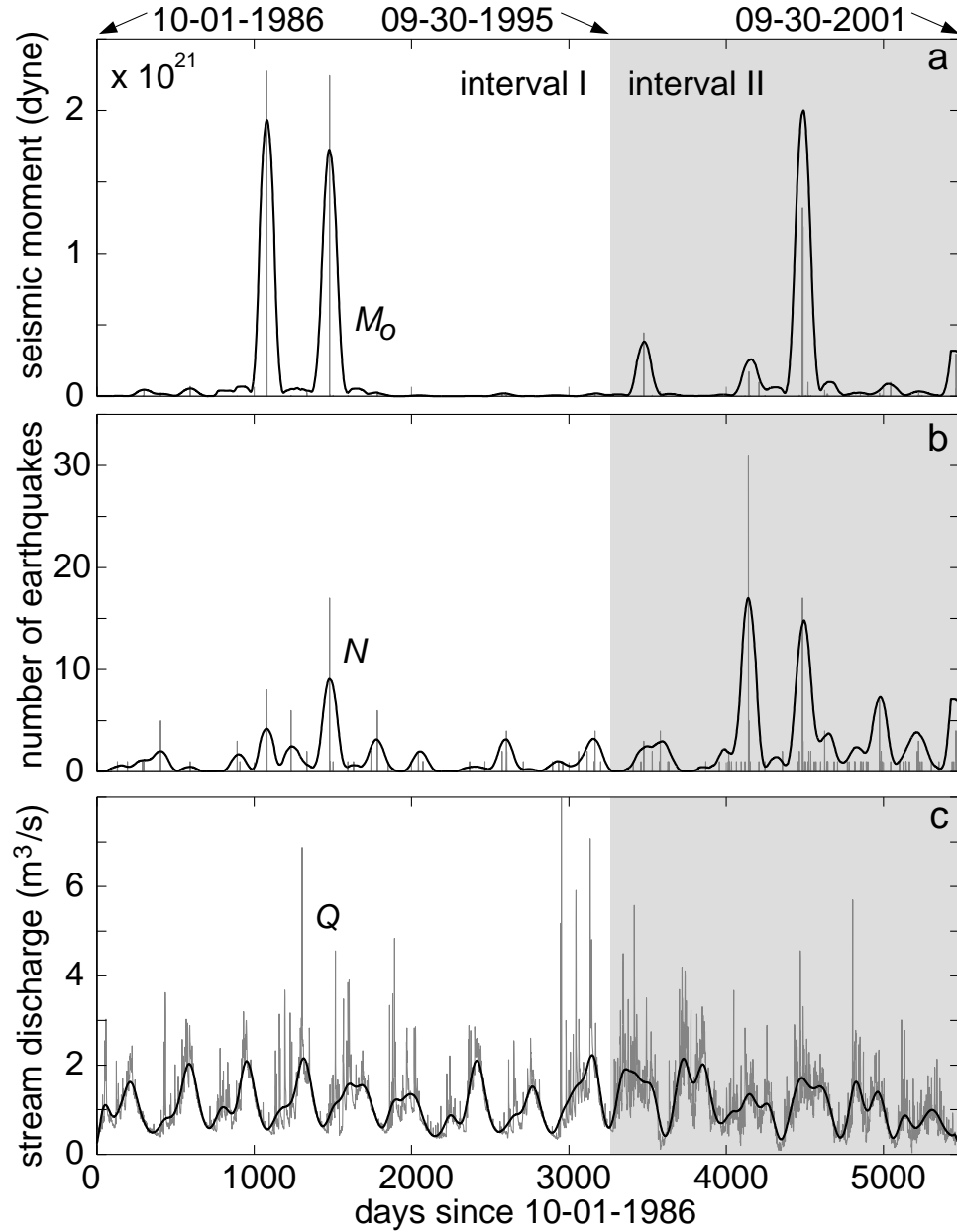


Figure 4.6. Original (gray) and interpolated (black) time series of a) seismic moment, b) number of earthquakes, and c) stream discharge of Salmon River at Mt. Hood. Stream discharge includes predicted data from Figure 4.3 for interval II. Interpolation is performed using a moving least-squares polynomial fit method of order ≤ 5 per segment as described in the text and in Appendix A.3. This assures that the data is optimally matched in a least-squares sense and that the series can be compared at equivalent frequency bands (Figure 4.7).

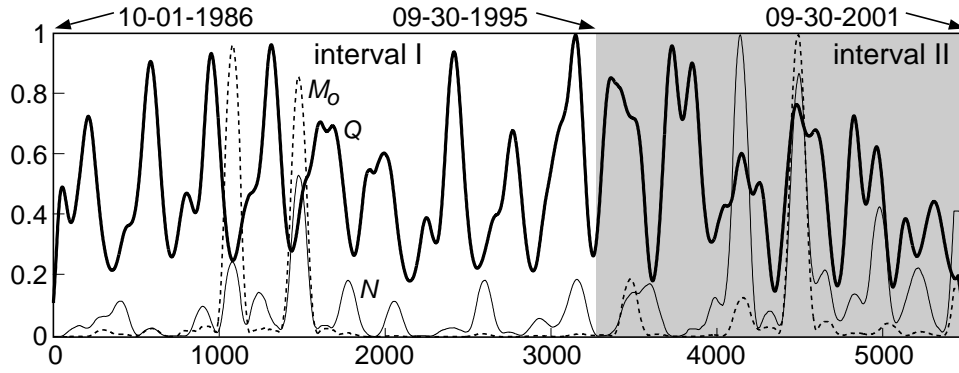


Figure 4.7. Interpolated time series from Figure 4.6, normalized by each series' absolute maximum value. Local maxima of number of earthquakes (thin solid line) and seismic moment (thin dashed line) typically follow local maxima of stream discharge (bold solid line) after a time lag of about 151 days.

confidence intervals for intervals I and I+II, respectively (Appendix A.4). Figure 4.9 shows statistically significant moving cross-correlation coefficients for $\overline{\Phi}_{QN}$ and $\overline{\Phi}_{QM_o}$ that are always distinct from the 90%, and in 3/4 of the cases even from the 99%, confidence limits for random earthquake distributions. Results from all segments are averaged for each time lag (bold lines in Figure 4.9). For both $\overline{\Phi}_{QN}$ and $\overline{\Phi}_{QM_o}$ a maximum is reached for a time lag of about $\Gamma \approx 151$ days.

4.3 Discussion

In the following I describe processes that can cause hydroseismicity and provide a model that allows me to determine both hydraulic diffusivity, κ , and critical pressure change, P' . From κ I then estimate hydraulic conductivity, K_h , and permeability, k . Throughout the discussion I compare my results with other studies.

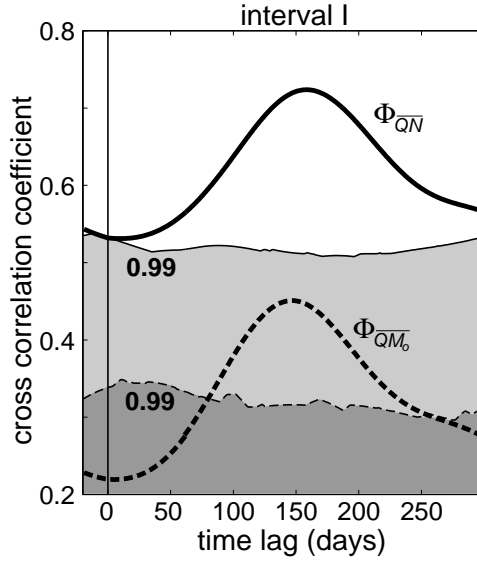


Figure 4.8. Time lag versus unbiased normalized cross-correlation coefficients Φ_{QN} (bold solid line) and Φ_{QM_o} (bold dashed line) for interval I. Thin horizontal lines indicate the respective upper bounds of the 99% confidence intervals of 1000 cross-correlations for randomly-assigned phases for each lag channel (Appendix A.4). Lower bounds are comparable to the negative of the upper bounds. Both curves suggest a time lag of about 151 days.

4.3.1 Causes of hydroseismicity

Principal mechanisms involved in triggering hydroseismicity may be explained by combining concepts from linear poroelasticity [198] with the Coulomb failure criterion,

$$\tau_s = \tau_0 + \mu\sigma'_n, \quad (4.5)$$

where τ_s , τ_0 , μ are the fault's shear strength, cohesion, and coefficient of friction, respectively, and σ'_n is the effective normal stress across the fault. Throughout this chapter compressive stresses are positive. σ'_n , is given by

$$\sigma'_n = \frac{\sigma'_1 + \sigma'_3}{2} + \frac{\sigma'_1 - \sigma'_3}{2} \cos(2\theta), \quad (4.6)$$

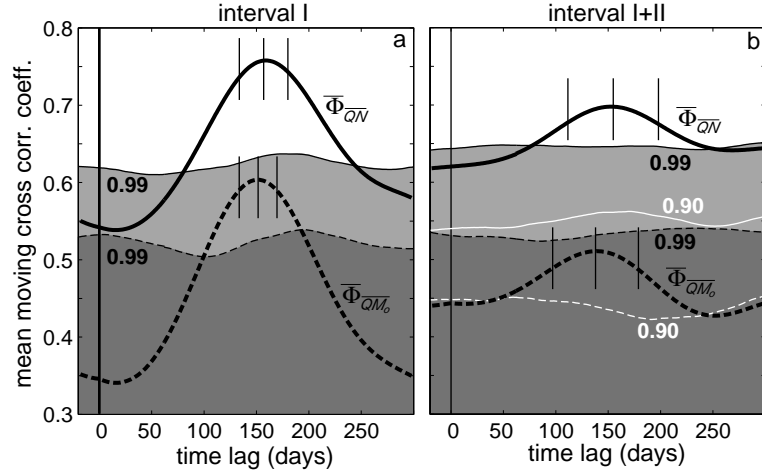


Figure 4.9. Time lag versus the mean of the unbiased normalized moving cross-correlation coefficients $\overline{\Phi}_{QN}$ (bold solid line) and $\overline{\Phi}_{QM_o}$ (bold dashed line). Thin horizontal lines indicate the respective upper bounds of the 99% (black) and 90% (white) confidence intervals of over 2000 cross-correlations for randomly-assigned phases for each lag channel (Appendix A.4). Lower bounds are comparable to the negative of the upper bounds. Vertical lines at maximum coefficient values indicate mean (center line) and mean $\pm 1\text{-}\sigma$ standard deviation (outer lines) for the respective time lags determined from 75 (a) and 109 (b) moving windows of 3-year width. The four mean time lags and respective standard errors are (in days): a) 157 ± 2.7 (solid line), 152 ± 2.1 (dashed line); b) 155 ± 4.1 (solid line), 139 ± 3.9 (dashed line), resulting in a total mean and standard error of 151 ± 6.6 days.

where σ'_1 and σ'_3 are the effective principal maximum and minimum compressive stresses, respectively, and θ is the angle between σ'_1 and the normal to the failure plane (Figure 4.10a). σ'_n clamps the fault requiring larger shear stresses, τ , to induce failure (Figure 4.10). The three effective principal stresses, σ'_1 , σ'_2 , and σ'_3 are the diagonal elements of the effective principal stress tensor given by

$$\boldsymbol{\sigma}' = \boldsymbol{\sigma} - \alpha P \delta_{ij}, \quad (4.7)$$

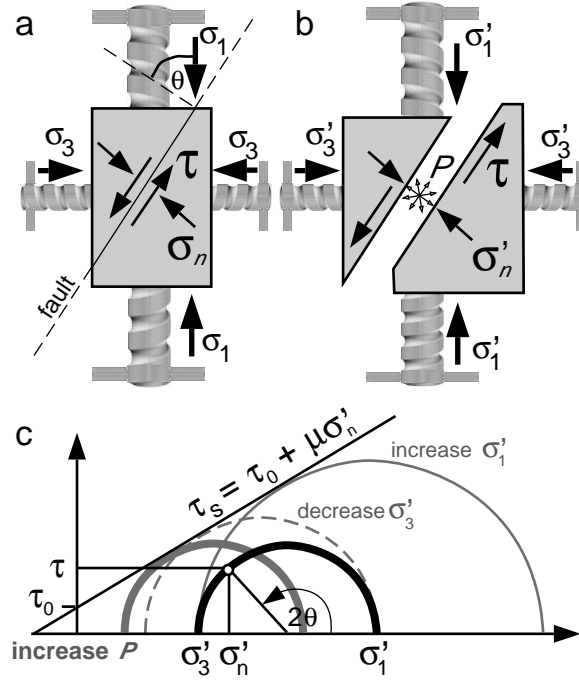


Figure 4.10. Relationship between stresses: a) pore-fluid pressure is $P = 0$ so that the effective stress is $\sigma' = \sigma$; b) pore-fluid pressure is $P \neq 0$ (the fluid-filled gap is drawn only for illustrative purposes) and thus $\sigma' = \sigma - \alpha P \delta_{ij}$ as described in the text; c) Mohr-circle with Mohr-Coulomb failure envelope (diagonal line). For explanation see main text.

where σ is the (regular) principal stress tensor, P is the pore fluid pressure, δ_{ij} is the Kronecker delta, and α is the Biot-Willis coefficient, defined as

$$\alpha = 1 - K/K_s. \quad (4.8)$$

Here, K and K_s are the bulk moduli (incompressibilities) of the bulk rock matrix and the solid “grains”, respectively [198]. A material’s deformation under drained conditions is given by the strain tensor, ϵ , that is related to the imposed effective stress tensor, σ' , by [198]

$$2G\epsilon = \sigma' + \frac{\nu_d}{1 + \nu_d} \sigma'_{kk} \delta_{ij}, \quad (4.9)$$

where $\sigma'_{kk} = \sigma'_{xx} + \sigma'_{yy} + \sigma'_{zz}$ is the trace of $\boldsymbol{\sigma}'$, G is the shear modulus, and

$$\nu_d = \left(\frac{\partial \epsilon_{jj}}{\partial \epsilon_{ii}} \right)_{\partial P=0; \partial \sigma_{jj}=0} \quad (4.10)$$

is the drained poisson's ratio. Deformation can lead to failure, when the shear stress,

$$\tau = \left| \frac{\sigma'_1 - \sigma'_3}{2} \sin(2\theta) \right|, \quad (4.11)$$

exceeds the material's shear strength, τ_s , in Eq. (4.5), for a given effective normal stress σ'_n . Because σ'_n and τ depend on both orientation of the fault within a stress field and on the magnitude of the stresses [Eqs. (4.6,4.11)], failure can be triggered by changes in both θ and $\boldsymbol{\sigma}'$ (Figure 4.10). The latter mechanism may induce earthquakes by causing 1) an increase in σ'_1 , 2) a decrease in σ'_3 , or 3) an equal decrease in all effective principal stresses, for example due to an increase in P [Eq. (4.7)]. The first two mechanisms cause failure by increasing the effective differential stress, $\sigma'_1 - \sigma'_3$, and thus shear stress, τ , in Eq. (4.11). The third mechanism induces failure by decreasing the effective strength of the material caused by a decrease in σ'_n which unclamps the fault and moves the Mohr-circle closer to the Mohr-Coulomb failure envelope, while leaving τ unchanged (Figure 4.10).

Fluctuations in pore-fluid pressure, P , denoted P' , on faults due to an increase in σ'_1 (e.g., by the weight of a filling reservoir that contracts the pore space) occur immediately. In contrast, a local increase in hydrostatic pore-fluid pressure, $P_h = \rho_w g h$, (e.g., by groundwater recharge, reservoir impoundment, or injection of fluids at depth), may trigger earthquakes after a time lag, Γ , that is related to pressure diffusion to the fault. Here, ρ_w is the density of water, g is acceleration due to the Earth's gravity, and h is the height of the water column above the point of interest. Reservoirs exhibit both processes and thus typically cause earthquakes both concurrent with, and delayed from, their filling [150, 173]. In this study I am interested in seismicity

induced by groundwater recharge and am thus focusing on earthquakes delayed from recharge by pore-fluid pressure diffusion. Here, the load of the additional groundwater is small and thus triggered seismicity due to a (small) increase in σ'_1 is neglected. Nonetheless, because only the connected pore space is fluid-filled, relatively high hydrostatic pore-fluid pressure changes, P' , may be reached that may be sufficient to induce earthquakes.

4.3.2 Analytic model

I can approximate the effect of seasonal groundwater recharge with periodic yearly ($\psi = 1$ year) pore-fluid pressure variations of amplitude P_0 at the surface ($z = 0$ m) as

$$P'(t, z = 0) = P_0 \cos\left(\frac{2\pi t}{\psi}\right). \quad (4.12)$$

Pore-fluid pressure evolution below the water table is governed by the (pressure) diffusion equation. In a 1-dimensional half-space the (pressure) diffusion equation is given by

$$\kappa \frac{\partial^2 P'}{\partial z^2} = \frac{dP'}{dt}, \quad (4.13)$$

where the hydraulic diffusivity,

$$\kappa = \frac{K_h}{S_s} = \frac{gk}{\nu S_s}, \quad (4.14)$$

is assumed constant. Here, K_h , S_s , k , and ν are the hydraulic conductivity, specific storage, permeability, and kinematic viscosity, respectively. The solution to Eq. (4.13) with boundary condition (4.12) is [192]

$$\frac{P'}{P_0} = \exp\left(-z\sqrt{\frac{\pi}{\psi\kappa}}\right) \cos\left(\frac{2\pi t}{\psi} - z\sqrt{\frac{\pi}{\psi\kappa}}\right) \quad (4.15)$$

and is graphed in Figure 4.11 for $\psi = 1$ year and hydraulic diffusivity $\kappa = 0.3 \text{ m}^2/\text{s}$ as determined later in Eq. (4.18) for the study region. The exponential term in Eq. (4.15)

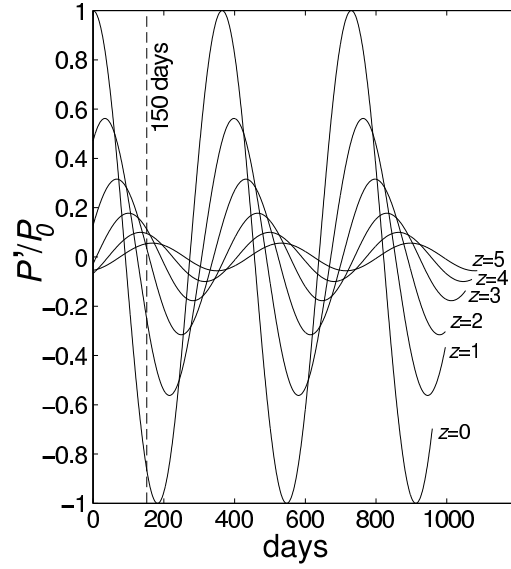


Figure 4.11. Periodic pore-fluid pressure fluctuations, P'/P_0 , at various depths, z (in km), for hydraulic diffusivity $\kappa = 0.3 \text{ m}^2/\text{s}$ and surface pressure perturbation periodicity $\psi = 1 \text{ year}$. With increasing depth, the amplitude of the pore-fluid pressure perturbation decreases and the phase lag increases. At a depth of 4.5 km, approximately 10% of the original pressure amplitude, P_0 , remains and the delay of the peak is about 151 days (dashed line), i.e., a phase lag of about 0.8π .

describes the decrease in the time-dependent pressure amplitude with depth, z , to $P'/P_0 = 1/e$ at a characteristic length scale (skin depth) of

$$z_c = \sqrt{\frac{\psi \kappa}{\pi}}. \quad (4.16)$$

The cosine term in Eq. (4.15) describes the periodic variations of the pressure signal as a function of both depth, z , and time, t . In addition, both terms in Eq. (4.15) are a function of κ and ψ .

The actual pore-fluid pressure at depth is $P = P_h + P'$, i.e., the hydrostatic pore-fluid pressure, P_h , with superimposed periodic pore-fluid pressure fluctuations, P' (Figure 4.12). The argument in the cosine in Eq. (4.15) is expected to be zero (or a multiple of 2π) so that the cosine reaches its maximum, one, during failure (e.g., point

C in Figure 4.12). It may be reasonable to assume that if a critical pore-fluid pressure, P_c , had been reached before the cosine maximum (e.g., point B in Figure 4.12) then failure should have occurred at shallower depths where a cosine maximum reaches the same critical pore-fluid pressure, P_c , earlier in time (e.g., point A in Figure 4.12). Here, I assume that the subsurface has a pervasive system of at least one fault along which failure can occur at any depth given appropriate stress conditions. Thus, from the condition that the argument of the cosine term in Eq. (4.15) has to be zero, I can determine κ from

$$\kappa = \frac{\psi z^2}{4\pi t^2}. \quad (4.17)$$

4.3.3 Hydraulic diffusivity

In this study the proposed period of pressure perturbation is $\psi = 1$ year and the time lag, Γ , between groundwater recharge and seismicity at Mt. Hood is $\Gamma = t = 151$ with a standard error of ± 7 days (Figure 4.9). Earthquake phase data for earthquake relocation was not readily available. Thus, I could not resolve whether the 1σ -standard deviation in the earthquake depth distribution, $z = 4.5 \pm 2$ km (Figure 4.1c), reflects error in determining earthquake locations. Hurwitz et al. [77] suggest that ice caps on many Cascade range volcanos may restrict recharge on their summits and uppermost flanks and that the water table below stratovolcanos may thus be relatively deep. Consequently, pore-fluid pressure diffusion distances to mean seismic depths may be shorter than the 4.5 km assumed here, while relatively slow flow through the unsaturated zone above the water table could delay fluctuations of water table levels. Furthermore, isotopic contents of water discharged for example at hydrothermal Meadows Spring suggest a recharge elevation of 2700 - 2900 m, i.e.,

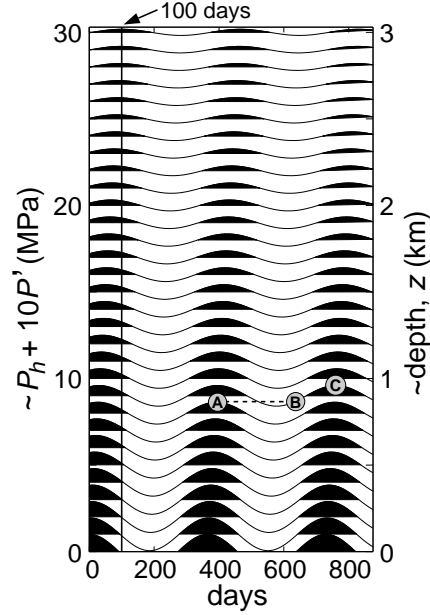


Figure 4.12. Hydrostatic pressure, P_h , (at depths from 0 to 3 km) with superimposed (for better visibility) 10-fold exaggerated periodic pore-fluid pressure fluctuations, $P = P_h + 10P'$, versus time for $\kappa = 0.3 \text{ m}^2/\text{s}$ and periodicity of $\psi = 1$ year. The critical pore-fluid pressure for failure should be reached at the maximum of the cosine term and a minimum possible depth (point A) as explained in the main text. At a depth of 3 km, the peak of the pressure perturbation is delayed (with respect to the surface) by 100 days (vertical line). Thus, at the mean earthquake depth of about 4.5 km the peak is delayed by the determined time lag of about 151 days. The upper halves of the sinusoids are filled to better visualize the decrease in amplitude and increase in phase lag of the pore-fluid pressure perturbation with increasing depth.

about 600 m below the summit of Mt. Hood [127]. However, lowering of the water table not only reduces the available diffusion time, t , in the saturated zone but also decreases the diffusion depth, z , to the earthquakes. Lower values of t and z in Eq. (4.17) tend to cancel each other. In addition, earthquake depths are determined relative to a horizontal plane that is approximately at the mean elevation (~ 1 km) of the relevant seismometers in the region. As a result, z and t assumed here are probably both somewhat smaller than may be expected. Due to the large uncertainty

in earthquake depth (± 2 km) already considered and due to the cancelling effects of reducing both z and t , I neglect the effects of water table reduction by a possible 0.5 to 1 km relative to the surface.

Using $\psi = 1$ year, $t \approx 151$ days, and $z \approx 4.5$ km in Eq. (4.17) yields a hydraulic diffusivity of

$$\kappa = 0.30 \pm 0.22 \text{ m}^2/\text{s}. \quad (4.18)$$

This value of κ agrees with other crustal hydraulic diffusivities compiled by Talwani and Acree [187] and is in the upper range for fractured igneous rocks [149]. Gao et al. [49] suggest a value as high as $1 \text{ m}^2/\text{s}$ for some fractured volcanic systems.

4.3.4 Critical pore-fluid pressure change

The step-function characteristics of a pore-fluid pressure increase due to initial reservoir impoundment and its error function solution [2, 187] does not allow for evaluation of the critical value of P'/P_0 at which failure occurs [187]. In contrast, the additional temporal information provided here by the periodicity of the surface pressure perturbation in the case of seasonal groundwater recharge allows for estimation of critical P'/P_0 . Because failure is likely to occur when the cosine term in Eq. (4.15) is one, I can determine P'/P_0 for the above calculated value of $\kappa = 0.3 \text{ m}^2/\text{s}$ at a mean depth of about $4 \leq z \leq 4.5$ km and period $\psi = 1$ year as

$$\frac{P'}{P_0} = \exp\left(-z\sqrt{\frac{\pi}{\psi\kappa}}\right) \approx 0.1. \quad (4.19)$$

Thus, about 10% of the estimated amplitude of near-surface pressure variations appears to be sufficient to trigger hydroseismicity at Mt. Hood.

Average annual precipitation in the (Oregon) Cascades, and particularly at Mt. Hood, is about 3 m [165] of which approximately 50% infiltrates the ground [85, 109]

mostly during spring snow melt. This leads to infiltration rates of about 1.5 m per year concentrated during a few months. Lava flows in the region typically have near-surface porosities of about 15 % [81] that decrease with depth. Thus, groundwater levels may fluctuate annually by approximately 10 m resulting in seasonal fluid pressure variations that may exceed $P_0 = 0.1$ MPa. Therefore, according to Eq. (4.19), the critical pore-fluid pressure increase at depth $z \approx 4.5$ km may be as low as $P' \approx 0.01$ MPa, and possibly lower, at Mt. Hood.

While several authors mentioned in the introduction, as well as this study, suggest that some earthquakes are triggered by pore-fluid pressure perturbations, the necessary critical pore-fluid pressure increase, P' , is uncertain [187]. However, it is often argued that many faults are near critically-stressed [190]. Therefore, small stress changes invoked by a variety of different mechanisms may be sufficient to cause seismicity on some preexisting faults. Examples include earthquake triggering by solid Earth and ocean tides [94, 188, 201], seasonal modulations of seismicity by the load of snow [68], precipitation and snow melt induced seismicity [100, 205] and general fluid-driven seismicity [4]. Lockner and Beeler [104] conduct laboratory studies of rock failure along preexisting faults induced by periodic axial stress changes superimposed on a confining pressure of 50 MPa. They find a transition from weak to strong correlation between periodic stress and failure at an amplitude of 0.05 to 0.1 MPa shear stress. Roeloffs [149, 150] suggests that an increase of $P' \approx 0.1$ MPa can cause reservoir-induced seismicity. Similarly, possible triggering of earthquakes by static stress changes of about 0.1 MPa and less has been proposed by King et al. [98] and Stein et al. [183, 184, 185]. Harris [65] summarizes the work of several authors and states that “It appears that static stress changes as low as 0.01 MPa (0.1 bar) can affect the locations of aftershocks.”

The examples cited previously as well as my results suggest that the necessary stress change for earthquake initiation on preexisting faults may be as low as 0.01 to 0.1 MPa which is only a fraction of the coseismic stress drop. Therefore, Harris [65] points out that Coulomb stress changes are said to “enhance” the occurrence of an earthquake, as opposed to generating it. I support this view and suggest that pore-fluid pressure changes due to groundwater recharge at Mt. Hood increase the probability of seasonal earthquake occurrences.

Heki [68] states that seasonal seismicity is not expected if the rate of secular (long-term) regional stress increase is much larger than the annual superimposed disturbance. For the case of the Cascades subduction zone, and assuming the validity of a characteristic earthquake model [169], the annual secular stress increase may be estimated by the (approximately constant) coseismic stress drop, $\Delta\sigma \approx 10$ MPa, divided by the average recurrence interval, $t_r \approx 300$ years, of large earthquakes. Estimated annual pore-fluid pressure fluctuations of 0.01 MPa/year at Mt. Hood at a mean earthquake depth of $z = 4.5$ km are comparable to $\Delta\sigma/t_r \approx 0.03$ MPa/year. Therefore, the pore-fluid pressure fluctuations below Mt. Hood at depths of about 4.5 km caused by groundwater recharge may be large enough to induce seasonal hydroseismicity.

The concentration of (hydro-) seismicity south of Mt. Hood may be due to preferential occurrences of active faults in this region [92, 127, 200]. Jones and Malone [92] performed earthquake relocations and determined focal mechanisms of events from the June-July 2002 swarm which reveal distinct clusters along normal faults (e.g., White River fault) located south of Mt. Hood as well as events located beneath the summit that appear to be magma-related. This relation between snow melt, groundwater recharge, and seismicity on faults that are kept relatively permeable, may

also be reflected by the occurrence of the only hydrothermal springs (Swim Warm Springs, Meadows Spring) at Mt. Hood [77, 127] in the region south of the volcano (Figure 4.1a).

4.3.5 Hydraulic conductivity and permeability

Once the hydraulic diffusivity, κ , is known, the hydraulic conductivity, K_h , permeability, k , or specific storage, S_s , can be determined by Eq. (4.14). The specific storage is given by

$$S_s = \rho g(\alpha + n\beta), \quad (4.20)$$

where α is the bulk aquifer compressibility (at constant vertical stress and zero lateral strain), n is the pore fraction, and $\beta = 4.8 \times 10^{-10} \text{ m}^2/\text{N}$ is the compressibility of water. If I assume a mean $n \approx 0.05$ for the study region [85] and $\alpha = 10^{-10} \text{ m}^2/\text{N}$ for fractured rock [37, 150], then, for the hydraulic diffusivity range given in Eq. (4.18), the hydraulic conductivity is

$$8 \times 10^{-8} \leq K_h = \kappa S_s \leq 5 \times 10^{-7} \text{ m/s} \quad (4.21)$$

which, from Eq. (4.14) and for a kinematic water viscosity of $\nu \approx 10^{-7} \text{ m}^2/\text{s}$ at 80°C , corresponds to a permeability range of

$$8 \times 10^{-16} \leq k \leq 5 \times 10^{-15} \text{ m}^2 \quad (4.22)$$

for the upper ~ 6 km of the crust at Mt. Hood.

The suggested permeabilities are relatively high compared with a maximum of $k \approx 10^{-16} \text{ m}^2$ required for mostly conductive heat transfer [114] as suggested for the Oregon Cascades at depths below about 2 km. However, I suggest two possible arguments that potentially explain why k is higher than may be expected.

First, a reasonable assumption is that permeability is much higher at shallower depths and decreases with depth due to compaction. Therefore, pore fluid diffusion is much faster in the shallower section and most of the observed time delay probably occurs at deeper portions of the profile. Reducing z for example by a factor of two in Eq. (4.17) would decrease κ , K_h , and k by a factor of four.

Second, I suggest that the region south of Mt. Hood is anomalous with respect to conductive heat transfer because it hosts the only two hot-springs observed on the flanks of Mt. Hood to date [127]. The presence of hot springs suggests that geothermal fluids rise relatively quickly along higher- k paths (e.g., faults) so that time scales for complete conductive thermal equilibration between hot fluids and colder surrounding rock are larger than the travel times of fluids. Indeed, Forster and Smith [46] suggest that hot springs can only be expected for a permeability window of $10^{-17} \leq k \leq 10^{-15} \text{ m}^2$. My permeability values from Eq. (4.22) fall in the upper range suggested for hot springs by Forster and Smith [46]. Here, high permeabilities lead to increased water fluxes that result in lower geothermal spring temperatures that are consistent with those (5°C to about 25°C [127]) observed at Meadows Spring and Swim Warm Springs.

The magnitudes for (mostly vertical) permeability, k , calculated here, reflect values for a large spatial scale that includes Mt. Hood and its nearby active (normal) faults that are kept permeable by rupture and appear to provide fluid pathways. That the magnitudes of hydraulic diffusivity, κ , and permeability, k , are plausible further supports the hypothesis of seasonal elevated seismicity levels due to groundwater recharge in this region.

4.4 Conclusions

Several arguments support the hypothesis that some seismicity at Mt. Hood, Oregon, is triggered by pore-fluid pressure diffusion as a result of rapid groundwater recharge due to seasonal snow melt. Statistically significant cross-correlation coefficients between groundwater recharge and seismicity suggest a time lag of about 151 days. The values of the correlation coefficients are distinct from those for random temporal earthquake distributions determined by Monte Carlo simulations. The time lag and mean earthquake depth provide a reasonable (mostly) vertical hydraulic diffusivity ($\kappa \approx 10^{-1} \text{ m}^2/\text{s}$), hydraulic conductivity ($K_h \approx 10^{-7} \text{ m/s}$), and permeability ($k \approx 10^{-15} \text{ m}^2$) that agree with other studies [46, 187, 190]. Finally, I determine the critical fraction ($P'/P_0 = 0.1 \text{ MPa}$) of the periodic near-surface pore-fluid pressure fluctuations ($P_0 \approx 0.1 \text{ MPa}$) that reach the mean earthquake depth, suggesting that $P' \approx 0.01 \text{ MPa}$ can trigger seismicity. This value of $P' \approx 0.01 \text{ MPa}$ is at the lower end of the range of critical pore-fluid pressure changes of $0.01 \leq P' \leq 0.1 \text{ MPa}$ suggested in previous studies [65, 98, 149, 150]. Therefore, while seismicity is distributed throughout the year at Mt. Hood, I conclude that some earthquakes are hydrologically induced by a reduction in effective stress due to a seasonal increase in hydrostatic pore-fluid pressure, P_h , by a small amount P' . In fact, elevated seismicity levels due to such small effective stress changes suggest that the state of stress in the crust at Mt. Hood, Oregon, could be near critical for failure.

Chapter 5

Permeability-depth curve

5.1 Introduction

Permeability, \mathbf{k} , describes a material's ability to transmit fluids. It is thus a critical material property that is relevant to numerous geological processes that depend on mass and/or energy transfer as for example described by Ingebritsen and Sanford [82]. Examples include transfer of water, steam, hydrocarbons, pore fluid pressure, and heat. Permeability is a second rank tensor that can be highly anisotropic and heterogeneous, varying over more than 15 orders of magnitude in geological materials [47]. Because fluid driving forces and viscosities vary much less, permeability is the most important parameter in geological porous media flow, largely determining fluid fluxes. Measuring the permeability of rock cores in laboratory settings [22, 23, 157] is done routinely. However, such rock core permeabilities may not reflect field-scale values [28, 79, 162] where larger representative elementary volumes [12] may have to be considered that include large-scale fractures or layers [37]. At intermediate field scales, from tens to hundreds of meters, it is frequently possible to conduct pumping

or slug tests [43] to determine \mathbf{k} . However, to investigate permeability distributions at large field scales, ranging from tens to thousands of meters, it is necessary to employ analytical or numerical models that are constrained by (sometimes indirect) observations [114].

Because \mathbf{k} affects mass and energy transfer it is in principle possible to use various observations as constraints or boundary conditions in models to estimate \mathbf{k} , provided that the observations depend on, or determine, mass and/or energy transport. Possible constraints and boundary conditions include classical hydrogeologic parameters such as surface water infiltration rates, hydraulic head distribution, spring discharge, and no-flow boundaries. Other observations may include subsurface temperature distribution, heat-flow, rock metamorphism, mineral precipitation, chemical or biological fluid-rock interactions, pore-fluid pressure variations and related seismicity, magma intrusions providing heat and volatiles, and concentrations of fluids and isotopes.

Hydrogeologic models are typically underconstrained, particularly at large scales. Therefore, utilizing multiple constraints is desirable. Despite the inherent difficulties of constraining fluid flow models, it is often the regional large-scale permeability distribution that has important implications for geological processes. These processes and applications include regional groundwater flow patterns, long-term water management, coupled heat and fluid transfer, geothermal energy exploration, carbon sequestration, subsurface waste fluid injection, and mineral, oil, and gas exploration.

In this chapter I determine permeability as a function of depth in the upper crust of the Oregon Cascades (Figure 5.1). The Cascades arc is a volcanic range located along an active, convergent plate boundary. I use four different modeling approaches to estimate 1-dimensional permeability, k (vertical or horizontal), at four different depth scales: 1) A spring discharge model provides insight into (mostly)

horizontal permeability values at depths of $z < 0.1$ km. 2) Analytic and numerical models of coupled heat and groundwater transfer provide vertical k at depth scales of about $z < 1$ km. 3) Studies of seismicity induced by groundwater recharge allow for estimates of vertical k at approximately $z < 5$ km. 4) Finally, magma intrusion and degassing models provide insight into permeabilities at the largest depth scale considered here of about $z < 15$ km. Methods from scale 1) as well as methods and results from scale 3) are based on previous publications [109, 111, 159] and are summarized, applied, and interpreted here to fit the objective of this chapter. Methods and results from scales 2) and 4) are original to this publication (and the corresponding manuscript in review) and are thus described in more detail.

I compare my results for permeability, k , as a function of depth, z , for the upper crust of the Oregon Cascades with the $k(z)$ -curve compiled by Manning and Ingebritsen [114] for continental crust in general and show that there is good agreement for depths larger than about 1 km. For depths smaller than approximately 1 km, I propose an exponential permeability curve. In addition, from the study of coupled heat and groundwater transfer (scale 2) I infer regional geothermal background heat-flow and groundwater recharge rates.

5.2 Four depth scales of k

I investigate permeability, k , at four different depth scales which are considered representative elementary volumes of four different sizes that are in themselves homogeneous but possibly anisotropic. In this section I present methods and results starting at the smallest (shallowest) and proceeding towards the largest (deepest) scale. The four methods employed either provide hydraulic conductivity, K (in ver-

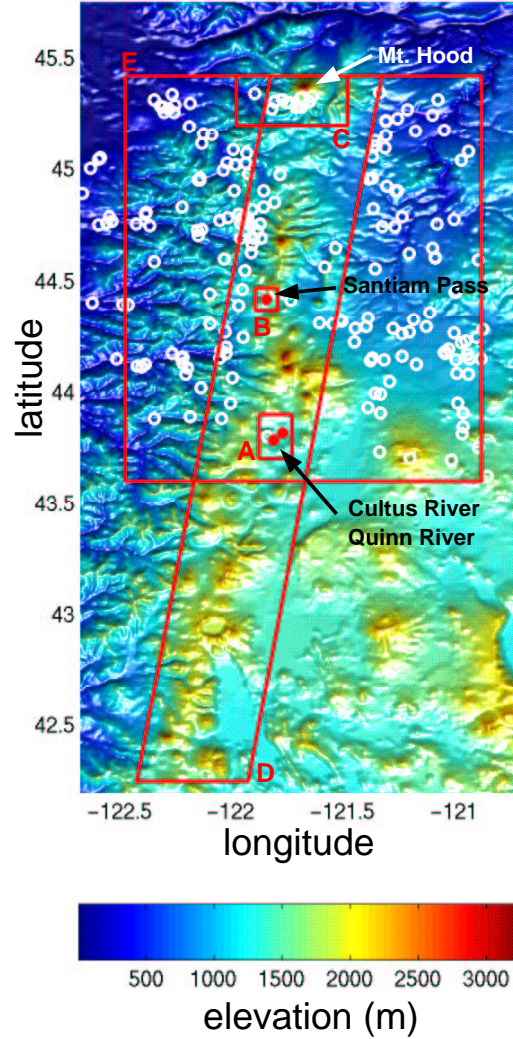


Figure 5.1. Shaded relief map of the study region in Oregon, USA. Red boxes indicate particular study regions used for the four methods and scales described in Section 5.2: A) spring discharge model, B) coupled heat and groundwater flow model in a 1-dimensional recharge area, C) radial coupled heat and groundwater flow model, D) magma intrusion model, E) region for heat-flow interpolation based on 209 geotherm profiles (white circles).

tical, K_z , or horizontal, K_x , direction) or vertical hydraulic diffusivity, κ_z . Both hydraulic conductivity, K , and hydraulic diffusivity, κ , are converted to permeability, k , as described in Section 5.3, so that the change in k as a function of depth can be discussed in Section 5.4. Appendix B.1 lists symbols used in this chapter, their units, and their definitions.

5.2.1 Spring discharge model: $k(z < 0.1 \text{ km})$

Manga [109, 111, 112] shows that discharge at springs can be used to estimate large-scale near-surface horizontal hydraulic conductivity, K_x , and horizontal permeability, k_x . I briefly describe the general approach and apply the method to discharge data from springs in the study region. I reserve interpretation for the discussion section.

Method

Stacked lava flows form aquifers that typically show high horizontal hydraulic conductivities within the upper blocky parts of each flow [23, 122]. The dense but jointed interior of a solidified lava flow shows predominantly vertical groundwater flow along cooling joints. Manga [112] suggests that the horizontal blocky layer may be approximated as a confined aquifer of mean constant thickness, b , and high horizontal hydraulic conductivity, K_x , and the dense interior as an unconfined aquifer providing water from storage according to its specific yield, S_Y . As a result, hydraulic head distribution is governed by a (1-dimensional) confined aquifer equation

$$\frac{\partial h}{\partial t} = \frac{K_x b}{S_Y} \frac{\partial^2 h}{\partial x^2} + \frac{u_R(x, t)}{S_Y}, \quad (5.1)$$

where specific storage, S_S , has been substituted by S_Y/b . Here, t , x , u_R , K_x , and S_Y are time, horizontal dimension, recharge rate, horizontal hydraulic conductivity, and specific yield, respectively. The (variable) hydraulic head in the dense interior layer is denoted h . Eq. (5.1) is equivalent to a linearized Boussinesq equation for unconfined aquifer flow, in which case b and h denote mean constant hydraulic head and small (variable) head, respectively. Eq. (5.1) is a linear diffusion equation where the hydraulic diffusivity is given by

$$\kappa_x = \frac{K_x b}{S_Y}. \quad (5.2)$$

As usual in a diffusive system, the diffusion time scale, \mathcal{T} , is characterized by $\mathcal{T} = L^2/\kappa_x$, where L is the aquifer length (Figure 5.2). Therefore, Eq. (5.2) becomes

$$K_x = \frac{S_Y L^2}{b \mathcal{T}}. \quad (5.3)$$

The aquifer thickness, b , is related to the mean residence time of water in the aquifer, \bar{t}_r , by

$$\bar{t}_r = \frac{A b S_Y}{\overline{Q}_s} = \frac{b S_Y}{\bar{u}_R}, \quad (5.4)$$

where A , \overline{Q}_s , and $\bar{u}_R = \overline{Q}_s/A$ are the surface area (exposed to recharge) of the unconfined aquifer, the mean spring discharge flux, and the mean groundwater recharge rate, respectively (Figure 5.2). Substituting Eq. (5.4) into Eq. (5.3) yields

$$K_x = \frac{S_Y^2 L^2}{\mathcal{T} \bar{t}_r \bar{u}_R}. \quad (5.5)$$

I determine horizontal hydraulic conductivity, K_x , from Eq. (5.5). Hydraulic diffusivity, κ_x , and other parameters can be estimated from baseflow recession curves of streams [1, 62, 174, 186]. The aquifer length, L , is given by the watershed geometry and κ_x is adjusted until good agreement between measured and calculated stream discharge is achieved [109, 111]. Mean groundwater recharge, \bar{u}_R , can be approximated by discharge in runoff-dominated streams [108]. Specific yield, S_Y , may be

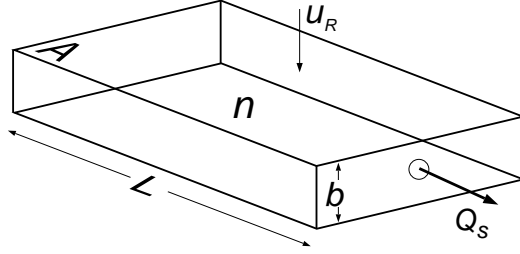


Figure 5.2. Spring discharge model of a simplified aquifer. Symbols are defined in the main text.

approximated by connected pore fraction, n . The mean residence time, \bar{t}_r , for these springs is determined from radiogenic tracers [87].

Results

I apply Eq. (5.5) to two spring-fed streams, Cultus River and Quinn River, in the Oregon Cascades (study region A in Figure 5.1). The input data from both streams and results for horizontal hydraulic conductivity, K_x , are given in Table 5.1. For the assumed range of specific yield, $0.05 \leq S_Y \leq 0.15$, the range of horizontal hydraulic conductivity is about

$$10^{-3} \leq K_x \leq 10^{-2} \text{ m/s.} \quad (5.6)$$

5.2.2 Coupled heat and groundwater transfer model:

$$k(z < 1 \text{ km})$$

Several studies have discussed heat and groundwater transfer in the subsurface [25, 36, 46, 52, 76, 179, 206, 207]. Similar to the work presented in this section, Dem-

Parameter	Quinn River	Cultus River
<i>Input Data to Eq. (5.5)</i>		
\bar{u}_R (m/year) ^a	0.66	1.27
\bar{t}_r (years) ^b	2.1	2.5
\mathcal{T} (years) ^c	3.2	4.8
$S_Y \approx n$ ^d	0.05 – 0.15	0.05 – 0.15
L (km) ^e	10	12
<i>Results from Eq. (5.5)</i>		
$-\log K_x$ (m/s)	2.7 – 1.8	3.1 – 2.2

Table 5.1. Spring model input and results for Quinn River and Cultus River. Data is provided in a) Manga [109], b) James et al. [87], c) Manga [109], d) Ingebritsen et al. [85], e) Manga [112].

ing [33] investigates coupled heat and groundwater flow at the north slope of Alaska to estimate the regional permeability. Here, I employ analytical and numerical models to simulate coupled groundwater and heat-flow in a 1-dimensional cartesian and a 3-dimensional cylindrical coordinate system, respectively. Due to low temperatures present in the region of interest, I assume gravity-driven convection only and no density-driven flow. This allows me to first solve the groundwater flow equation followed by the heat advection-diffusion equation to determine the temperature field. In Section 5.2.2, the temperature distribution is compared with measurements in boreholes to evaluate model input parameters.

Method: 1D flow

The central axis of approximately radially symmetric mountains as well as the vertical axis at the center of saddles between two such mountains may be represented by vertical 1-dimensional (1D) groundwater recharge and flow regimes (vertical lines in Figure 5.3). Away from the axes flow becomes 2-dimensional (2D) or possibly 3-dimensional (3D). In this section, I employ analytical models of coupled groundwater

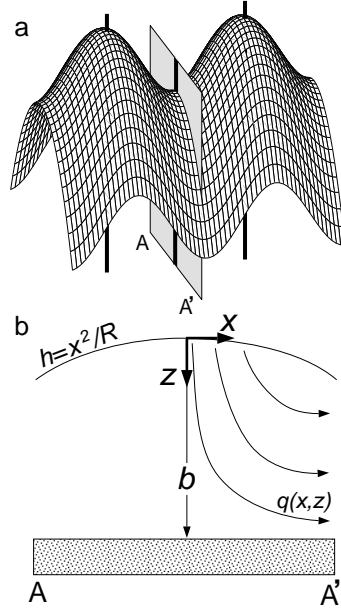


Figure 5.3. a) Schematic peaks (e.g., Three Fingered Jack and Mt. Washington, Oregon) and a saddle (e.g., Santiam Pass, Oregon) may represent groundwater recharge regimes with 1-dimensional (1D) vertical groundwater flow. The saddle can also constitute a (local) groundwater discharge regime. b) Schematic cross section A-A' (see panel a) showing a typical recharge geometry. Parameters are defined in the main text.

and heat transfer in a 1D recharge region.

Phillips [138] derives a solution for the advection-diffusion equation, providing temperature as a function of depth, $T(z)$, in a 1D groundwater recharge area. The solution assumes a constant mean horizontal permeability and a linear decrease in vertical groundwater flow (Darcy) velocity, u_z , from a recharge (Darcy) velocity at the surface to $u_z = 0$ at the bottom of the aquifer. Here, I provide an equivalent solution for $T(z)$, Eq. (5.16), however with inverted z -axis so that z is positive-downwards, consistent with the reference frame adopted for this chapter (Figure 5.3b). In addition, I introduce a solution to the 1D heat advection-diffusion equation where permeability decreases exponentially with depth, Eq. (5.15). More detailed derivations of the equa-

tions can be found in Appendices B.2 and B.3. For the remainder of this section I will refer to Darcy velocity, \mathbf{u} , as velocity, with the understanding that the actual interstitial (seepage) velocity is given by $\mathbf{v} = \mathbf{u}/n$, where n is the connected pore fraction. The vertical mean recharge velocity at the surface, $z = 0$, is $\bar{u}_R = \bar{u}_z(z = 0) = \Phi\Psi$, where Φ is the fraction of the precipitation, Ψ , that infiltrates the ground. In the Oregon Cascades, $\Phi \approx 0.5$ and $\Psi \approx 2$ m/year [81] so that $\bar{u}_R \approx 1$ m/year.

In a recharge zone (Figure 5.3), the vertical velocity, u_z , at depth, z , is given by the divergence in the horizontal directions, $\mathbf{x} = (x, y)$, of the volume flux per unit width, \mathbf{q} , i.e., [138]

$$u_z(z) = \nabla_{\mathbf{x}} \cdot \mathbf{q}. \quad (5.7)$$

For an exponential decrease in hydraulic conductivity with depth, \mathbf{q} is given by

$$\mathbf{q} = K_s(b - z)e^{-z/\delta} \nabla_{\mathbf{x}} h(\mathbf{x}). \quad (5.8)$$

Therefore,

$$\begin{aligned} u_z(z) &= \nabla_{\mathbf{x}} [K_s(b - z)e^{-z/\delta}] \cdot \nabla_{\mathbf{x}} h(\mathbf{x}) \\ &+ K_s(b - z)e^{-z/\delta} \nabla_{\mathbf{x}}^2 h(\mathbf{x}), \end{aligned} \quad (5.9)$$

where $\nabla_{\mathbf{x}}$ and $\nabla_{\mathbf{x}} \cdot$ are the respective gradient and divergence operators in the horizontal directions, $\mathbf{x} = (x, y)$, and h is the hydraulic head, K_s is the near-surface hydraulic conductivity, and b is the total vertical thickness of the saturated zone. The skin depth, δ , in the exponential term determines the decrease in K (from a near-surface value, K_s) as a function of depth, z . In the case of constant hydraulic conductivity and linearly decreasing u_z to $u_z(z = b) = 0$, the skin depth is given by $\delta = \infty$ and thus the exponential terms in Eqs. (5.8) and (5.9) vanish. At the vertical symmetry axis in Figure 5.3b, the water table is at a maximum, and thus

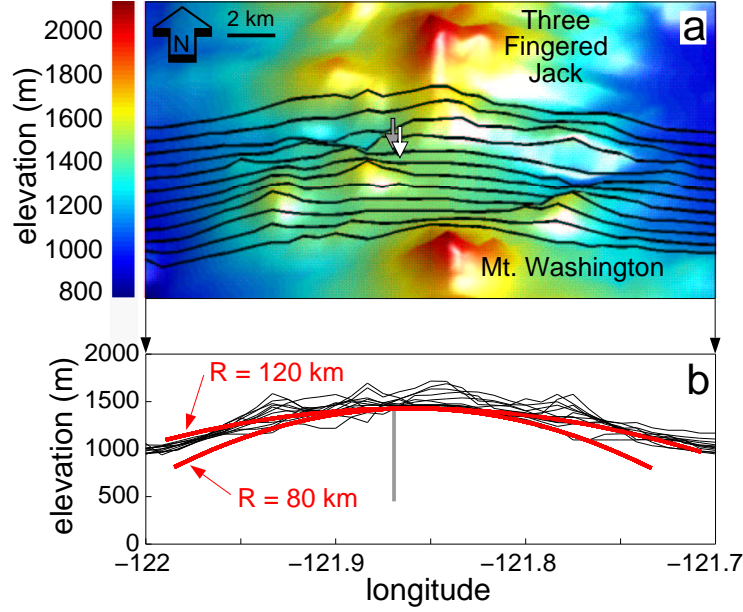


Figure 5.4. Radius of curvature of the Earth's surface at Santiam Pass, Oregon. a) Shaded relief map between longitudes 44.25 and 44.55, color coded to elevation. Black lines indicate locations of the 12 cross sections shown in b. The geotherm borehole location is indicated by the gray arrow. Weather station 357559 (U.S. Department of Commerce, National Oceanic & Atmospheric Administration, NOAA) is given by the white arrow. b) East-west cross sections (thin black lines) used to estimate the minimum ($R=80$ km) and maximum ($R=120$ km) radius of curvature (red curves). The geotherm borehole is shown as the gray vertical line.

$\nabla_{\mathbf{x}} h(\mathbf{x}) = (0, 0)$ so that Eq. (5.9) reduces to

$$u_z = \frac{K_s(b-z)}{R} e^{-z/\delta}, \quad (5.10)$$

where $R = -(\partial^2 h / \partial x^2)^{-1}$ is the radius of curvature of the water table (in x-direction) and is assumed constant near the symmetry axis where $\|\mathbf{x}\| \approx 0$. I use topography (Figure 5.4) to obtain $R \approx 100$ km. For an incompressible fluid, $\nabla \cdot \mathbf{u} = 0$. Thus, for u_z given by Eq. (5.10) the 1D horizontal velocity is

$$u_x = \frac{K_s}{R} \left(\frac{b-z}{\delta} + 1 \right) x e^{-z/\delta}. \quad (5.11)$$

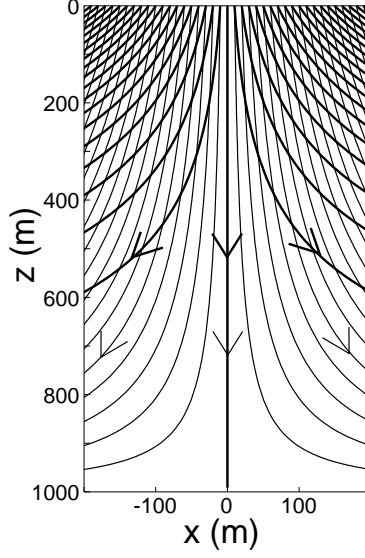


Figure 5.5. Groundwater flow streamlines near a 1D recharge region for exponentially decreasing hydraulic conductivity, Eqs. (5.10) and (5.11) with $\delta = 270$ (bold curves), and constant hydraulic conductivity, Eqs. (5.12) and (5.13) (thin curves). The exponential K model, leads to a recharge velocity of $u_R \approx 0.9$ m/year compared with $u_R \approx 0.1$ m/year for the constant K model (Figure 5.7a).

As before, $\delta = \infty$ for constant hydraulic conductivity, reducing Eqs. (5.10) and (5.11) to

$$u_z = \frac{K_s}{R}(b - z) \quad (5.12)$$

and

$$u_x = \frac{K_s}{R}x, \quad (5.13)$$

respectively, which are equivalent to the solutions presented by Phillips [138] with inverted z -axis. Figure 5.5 shows groundwater flow streamlines based on Eqs. (5.10-5.13) for both constant and exponentially decreasing hydraulic conductivity. Substituting Eq. (5.10) into the steady-state 1D vertical heat advection-diffusion equation,

$$\gamma u_z \frac{\partial T}{\partial z} = \kappa_m \frac{\partial^2 T}{\partial z^2}, \quad (5.14)$$

and integrating with respect to z , yields (Appendix B.2)

$$\frac{\partial T}{\partial z} = - \left(\frac{\partial T}{\partial z} \right)_b \exp \left[\frac{\gamma K_s \delta}{\kappa_m R} e^{-z/\delta} \left(z - b + \delta - \delta e^{\frac{z-b}{\delta}} \right) \right] \quad (5.15)$$

for exponentially decreasing hydraulic conductivity. To obtain $T(z)$, I integrate Eq. (5.15) numerically with respect to z and with boundary condition $T(z=0) = T_R$, where T_R is the (near-surface) recharge temperature.

In contrast to Eq. (5.15), for the case of constant hydraulic conductivity, i.e., linearly decreasing u_z , Eq. (5.12) is substituted into Eq. (5.14) and integrated twice with respect to z resulting in (Appendix B.3)

$$T = T_R - \left(\frac{\partial T}{\partial z} \right)_b \sqrt{\frac{\pi \kappa_m R}{2 \gamma K_s}} \operatorname{erfc} \left[(b - z) \sqrt{\frac{\gamma K_s}{2 \kappa_m R}} \right]. \quad (5.16)$$

Here, erfc is the complementary error function, $(\partial T / \partial z)_b$ is the (conductive) background temperature gradient at the bottom of the aquifer, and

$$\gamma = \frac{\rho_w c_w}{\rho_m c_m}. \quad (5.17)$$

For a given pore fraction, n , mixed properties, ξ_m , of the water-rock complex are approximated by

$$\xi_m = n \xi_w + (1 - n) \xi_r, \quad (5.18)$$

where ξ_w and ξ_r are the properties in question of pure water and pure rock, respectively. Water-rock complex properties to be substituted into Eq. (5.18), where subscripts remain as given in Eq. (5.18), are mixed density, $\xi = \rho$, mixed specific heat, $\xi = c$, and mixed thermal conductivity, $\xi = k_T$. Mixed thermal diffusivity is then given by

$$\kappa_m = \frac{k_{Tm}}{\rho_m c_m}. \quad (5.19)$$

Throughout this analysis I assume local thermal equilibrium between water and rock and that n is sufficiently small so that Eq. (5.18) applies.

In Section (5.2.2) I compare results from the exponential- k [integral of Eq. (5.15)] and constant- k [Eq. (5.16)] solutions and estimate groundwater recharge rates, u_R , characteristic depth scale, δ , aquifer thickness, b , and background heat flux,

$$H_b = -k_{T_r} \left(\frac{\partial T}{\partial z} \right)_b. \quad (5.20)$$

Here, k_{T_r} is the thermal conductivity of the rock alone, assumed to be on average about $k_{T_r} \approx 2 \text{ Wm}^{-1}\text{C}^{-1}$, based on measurements on cores and cuttings from the Cascades [18, 81].

Method: Radial flow

As described previously, owing to relatively low temperatures, I assume only gravity-driven convection and no density-driven flow. This allows me to first solve the steady-state groundwater flow (hydraulic head diffusion) equation,

$$\frac{\partial}{\partial r} \left(K_r \frac{\partial h}{\partial r} \right) + \frac{K_r}{r} \frac{\partial h}{\partial r} + \frac{\partial}{\partial z} \left(K_z \frac{\partial h}{\partial z} \right) = 0, \quad (5.21)$$

for anisotropic (and possibly heterogeneous) hydraulic conductivities, \mathbf{K} , in a 3D-cylindrical coordinate system using only hydrogeologic and no thermal boundary conditions. Here, h is the variable hydraulic head and K_r and K_z are the hydraulic conductivities in the radial, r , and vertical, z , directions, respectively. This coordinate system is chosen because of the radial symmetry of Mt. Hood (Fig. 5.6). The outer no-flow boundary is chosen based on the occurrence of apparent groundwater-recharge induced earthquakes (Section 5.2.3 and [159]) and on the existence of a borehole geotherm that shows a concave-down temperature profile (triangles in Fig. 5.8) suggesting upward flow of warmer water [25].

I solve Eq. (5.21) numerically by employing a finite difference algorithm with successively under-relaxed iterations (Appendix B.4). The obtained hydraulic head

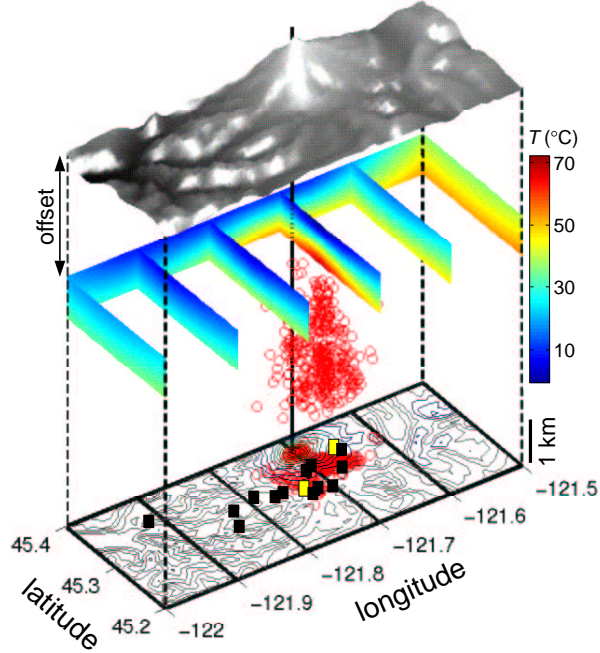


Figure 5.6. Shaded relief map of Mt. Hood, Oregon, and subsurface temperature distribution (color coded) based on a multiquadratic interpolation of thirteen geotherms (black bars) in study region C in Figure 5.1. The relief map is vertically offset by 3 km from the temperature map for better visualization of the temperature data. Elevated temperatures beneath Mt. Hood appear to be offset towards the south (see vertical bar through the summit for comparison), consistent with the occurrence of the only two hot spring areas, Meadows Spring and Swim Warm Springs (yellow bars on contour plot) observed to date at Mt. Hood [127]. Most earthquakes also occur beneath the southern flanks of the volcano (see projection of earthquakes onto map) and show mostly normal-fault focal mechanisms (Section 5.2.3 and [92, 159]).

field, $h(r, z)$, in the rz -plane is then converted into a Darcy velocity field, $u(r, z)$, using a finite difference approach (Appendix B.4).

I determine the temperature distribution by solving the steady-state heat-advection-

diffusion equation (without heat sources or sinks) in cylindrical coordinate form,

$$\frac{\kappa_m}{\gamma} \left(\frac{\partial^2 T}{\partial r^2} + \frac{1}{r} \frac{\partial T}{\partial r} + \frac{\partial^2 T}{\partial z^2} \right) = -u_r \frac{\partial T}{\partial r} - u_z \frac{\partial T}{\partial z}, \quad (5.22)$$

where T , u_r , and u_z are temperature and Darcy velocities in the radial and vertical directions, respectively.

Eq. (5.22) is also solved using a finite difference approximation and successively under-relaxed iterations (Appendix B.4). Boundary conditions (Appendix B.5) for Eqs. (5.21) and (5.22) are no groundwater- and heat-flow (Dirichlet) boundary conditions, $\partial h/\partial r = 0$ and $\partial T/\partial r = 0$, at the central axis and at the outer boundary. The lower boundary has mixed boundary conditions with no groundwater flow, $\partial h/\partial z = 0$, but constant heat-flow (Neumann) boundary condition, $\partial T/\partial z = \text{constant}$. Hydraulic head and temperature distribution along the upper boundary are a function of elevation, where the water table is assumed to be similar to the topography and temperature is approximated by the mean adiabatic lapse rate (MALR).

Hurwitz et al. [77] suggest that water tables in volcanos with ice-caps may be much lower than the surface. However, for the approximate radial model the uncertainty associated with the unknown position of the water table is small compared with the overall model dimensions.

Results for 1D and radial flow

Figure 5.7a shows measured [16] and modeled temperature-depth profiles for the groundwater recharge region at Santiam Pass, Oregon. Solutions to both the constant, Eq. (5.16), and the exponentially decreasing, integral of Eq. (5.15), hydraulic conductivity model are provided. Both models suggest a very similar aquifer thickness, $b \approx 1000$ m, and background heat flux, $H_b \approx 0.080$ W/m² (Table 5.2). However,

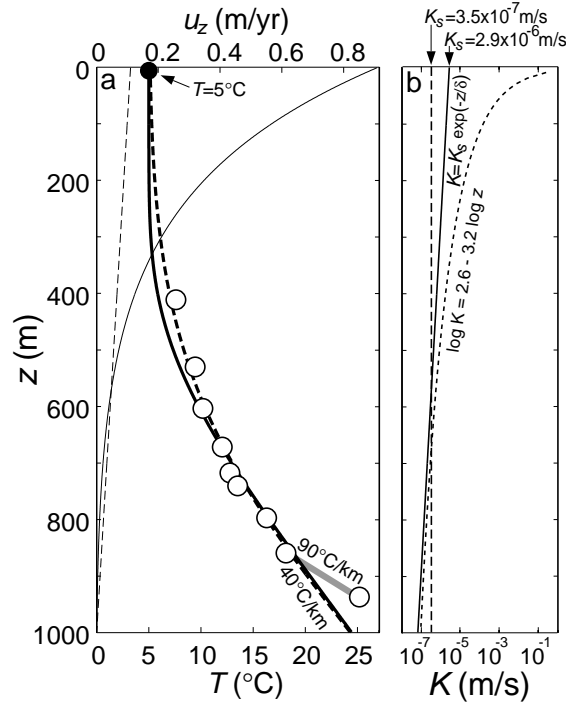


Figure 5.7. a) Temperature, T , models (bold curves), and vertical groundwater flow velocity, u_z (thin curves), versus depth, z , at Santiam Pass, Oregon. White-filled circles are temperature measurements from drill hole SP 77-24 [16]. Thin curves show $u_z(z)$ -profiles for the constant (dashed line, Eq. 5.16) and exponential (solid curve, numerical integral of Eq. 5.15) hydraulic conductivity profiles (see panel b). The filled circle is the mean annual surface temperature at closeby NOAA weather station 357559 (white arrow in Figure 5.4a) at Santiam Pass, Oregon, averaged over the last 10 available years (1975 - 1984) at an elevation of 1449 m. Precipitation rate at the same weather station is about 2.2 m/year. The gray bold line connects the deepest two data points at a slope of about 90°C/km. The slope of the models at $z \approx 1000$ m is about 40°C/km. b) Hydraulic conductivity, K , versus depth, z , for the constant $K = 3.5 \times 10^{-7}$ m/s model (long-dashed line) and the exponential $K = K_s \exp(-z/\delta)$ model (solid line) with $K_s = 2.9 \times 10^{-6}$ m/s and $\delta = 270$ m. The short-dashed curve is the permeability-depth curve suggested by Manning and Ingebritsen [114] converted to z in m and hydraulic conductivity in m/s, assuming a constant temperature of about 20°C. Parameters are provided in Table 5.2 and Appendix B.1.

the constant K model requires a much lower recharge rate of $u_R \approx 0.1$ m/year compared with the exponentially decreasing K model which allows for $u_R \approx 0.9$ m/year. The larger recharge velocities in the latter case (thin solid curve in Figure 5.7a) are due to near-surface hydraulic conductivities that are about one order of magnitude larger than in the case of constant K (Figure 5.7b). The mean absolute error between temperature data, T_D , and calculated temperatures, T_C , is given by $\epsilon = |T_D - T_C|/N$, where N is the number of measurements (including the surface temperature). The constant K model allows for a lower minimized error of $\epsilon \approx 0.68^\circ\text{C}$ compared with $\epsilon \approx 0.92^\circ\text{C}$ for the exponential K model. However, the improvement in ϵ for the constant K model is only by a factor of about 1.4. In contrast, the exponential model improves estimates of recharge rates, u_R , by about a factor of 9, as typical values are about $u_R \approx 1$ m/year in the Cascades [81]. In addition, recharge rates of $u_R \approx 1$ m/year are also supported by the results from the radial model discussed in the next paragraph.

Figure 5.8 shows measured and calculated temperature-depth profiles for the three geotherm boreholes that fall within the radially symmetric model region at Mt. Hood. Results agree well with the two deeper profiles but the shallow profile shows some deviations from measurements that are probably dominated by limitations in reducing the three dimensions into a 2D cross section (i.e., owing to deviations from radial symmetry). Minimizing the misfit, ϵ , between model and data yields a horizontal near-surface hydraulic conductivity, $K_{xs} = 10^{-6}$ m/s, that is about 30 times larger than the vertical near-surface hydraulic conductivity, $K_{zs} = 3 \times 10^{-8}$ m/s. Both conductivities are assumed to decrease exponentially with depth according to a skin depth of $\delta = 250$ m. The simulation results also suggest a background heat-flow of $H_b \approx 0.134$ W/m² and a recharge velocity of $u_R \approx 1$ m/year (Table 5.2).

Symbol	Units	1D	1D	3D-radial
$K_x(z)$	(m/s)	K_{zs}	$K_{zs}e^{-z/\delta}$	$\eta K_{zs}e^{-z/\delta}$
K_{zs}	(m/s)	3.4×10^{-7}	2.9×10^{-6}	3.3×10^{-8}
δ	(m)	∞	270	250
η		1	1	30
b	(m)	1000	1000	1200
h	(m)	x^2/R	x^2/R	TOPO
u_R	(m/yr)	0.1	0.9	1
T_R	(°C)	5	5	MALR
$(\frac{\partial T}{\partial z})_b$	(°C/m)	0.042	0.040	0.067
H	(W/m ²)	0.84	0.080	0.134
ϵ	(°C)	0.68	0.92	~ 1

Table 5.2. Parameters for coupled groundwater and heat-flow models. The anisotropy ratio of horizontal to vertical hydraulic conductivity is given by $\eta = K_x/K_z$. For the radial model the recharge temperature is determined by the mean adiabatic lapse rate (MALR) and the hydraulic head, h , is approximated by topography (TOPO). For the 1D models, h is determined by the radius of curvature of the water table, $R = 10^5 \pm 2 \times 10^4$ m (Figure 5.4), and the horizontal distance, x , from the maximum h in the recharge region.

5.2.3 Groundwater-recharge-induced seismicity model:

$$k(z < 5 \text{ km})$$

Saar and Manga [159] (see also Chapter 4) suggest that an increase in seismicity in late summer at Mt. Hood, Oregon, is caused by seasonal groundwater recharge during spring due to snow melt on the flanks of the volcano. They show that a statistically significant correlation exists between groundwater recharge and seismicity. Groundwater recharge is approximated by discharge in runoff-dominated streams. The recharge in this region provides a natural pore-fluid pressure signal of narrow temporal width and potentially relatively large amplitude. The pore fluid pressure pulse diffuses and can cause an effective stress decrease on preexisting faults at depth, effectively “unclamping” the fault and triggering earthquakes. Saar and Manga [159] use the time lag between groundwater recharge and increased seismicity at a mean

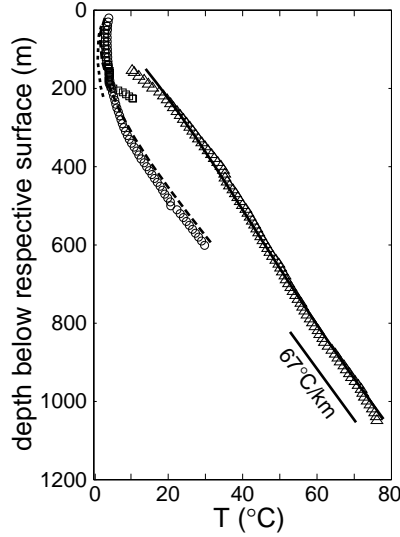


Figure 5.8. Temperature, T , versus depth, measured from the surface at each geotherm at Mt. Hood, Oregon. The solid, dashed, and dotted curves are results from the 3D-radial simulation. Measurements are indicated by triangles, circles, and squares. Two geotherms (circles and squares) show typical recharge dominated profiles with isothermal upper section, similar to the one shown in Figure 5.7a. The geotherm depicted by the triangles shows a mostly linear (conductive) profile with a slight concave-downward bend at shallower depths, suggesting a groundwater discharge region.

depth of 4.5 km to estimate (vertical) hydraulic diffusivity, K_z , for the depth range of $0 < z < 5 \times 10^3$ m, assumed to be homogeneous.

Method

The solution to the 1-dimensional (pressure) diffusion equation for periodic sinusoidal boundary conditions,

$$P'(t, z = 0) = P_0 \cos\left(\frac{2\pi t}{\psi}\right), \quad (5.23)$$

in a half-space is given by [192]

$$\frac{P'}{P_0} = \exp\left(-z\sqrt{\frac{\pi}{\psi\kappa_z}}\right) \cos\left(\frac{2\pi t}{\psi} - z\sqrt{\frac{\pi}{\psi\kappa_z}}\right), \quad (5.24)$$

where P_0 , P' , ψ , t , and z are near-surface pore fluid pressure amplitude, pore fluid pressure amplitude at depth (in excess to hydrostatic pressure), period, time, and depth, respectively. The cosine term in Eq. (5.24) describes the phase lag of the pressure peak as a function of depth. Saar and Manga [159] (see also Chapter 4) show that the argument in the cosine-term is likely to be zero (or a multiple of 2π) and can thus be used to determine vertical hydraulic diffusivity,

$$\kappa_z = \frac{\psi z^2}{4\pi t^2}. \quad (5.25)$$

Results

I use Eq. (5.25) to determine the large-scale vertical hydraulic diffusivity, κ_z , for the upper 5 km of crust at Mt. Hood, Oregon. The periodicity of groundwater recharge due to snow melt in spring is $\psi = 1$ year. The mean earthquake depth, $z = 4.5$ km, and time lag, $t = 151$ days (determined by cross correlations), provide the remaining parameters for Eq. (5.25), resulting in a hydraulic diffusivity of [159]

$$\kappa_z = 0.30 \pm 0.22 \text{ m}^2/\text{s}. \quad (5.26)$$

5.2.4 Magma intrusion and degassing model: $k(z < 15 \text{ km})$

The Cascades range is a volcanic arc located at the convergent plate boundary between the Juan de Fuca plate and the North American plate. Subduction zone related magmas intrude into the crust where they may (partially) solidify, assimilate crustal material, and/or erupt. Devolatilization of (mostly) water from solidifying

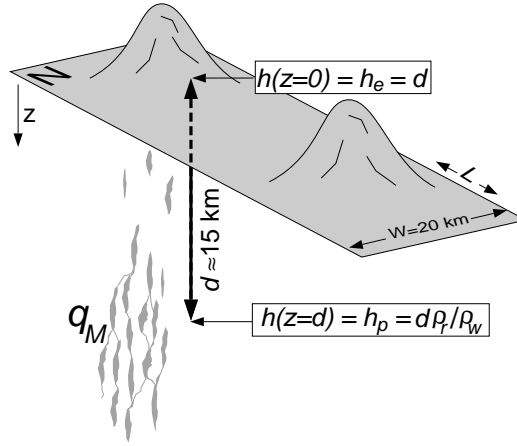


Figure 5.9. Schematic illustration of magma intrusion underneath the Cascades range volcanic arc (not drawn to scale), after Hildreth [69]. Symbols are defined in the main text.

magma provides a fluid source in the crust that, due to conservation of mass, is transmitted to the Earth's surface, unless consumed in metamorphic reactions. This volumetric fluid flux, Q , can be used to estimate vertical hydraulic conductivity, K_z , on a depth scale of about 15 km, i.e., from the estimated main magma intrusion depth to the surface (Figure 5.9). As before, within this region, K_z is assumed homogeneous.

Method

The volumetric magma flux is given by

$$Q_M = q_M W, \quad (5.27)$$

where q_M is the volumetric magma intrusion rate per kilometer arc length and W is the estimated arc width (Figure 5.9). I assume that only water devolatilizes. Therefore, the volume flux of water, Q_w , released by the solidifying magma is given by

$$Q_w = \frac{q_M W \rho_M \phi_w}{\rho_w}, \quad (5.28)$$

where ϕ_w , ρ_M , and ρ_w are weight fraction of water content in the magma, and the densities of magma and water, respectively. In one (vertical) dimension, Darcy's law reduces to

$$q_z = \frac{Q_w}{A} = -K_z \frac{\partial h}{\partial z}, \quad (5.29)$$

where A and z are the total cross-sectional area perpendicular to the fluid flow direction and depth, respectively. Here, $A = WL$, where $L = 1$ km is the arc length considered for the magma intrusion rate, q_M , described previously. The hydraulic head, $h = h_e + h_p$, is the sum of elevation head, h_e , and pressure head, $h_p \approx P\rho_w^{-1}g^{-1}$, where P is the pore fluid pressure. At depth, z , the magma and its exsolved volatiles are under lithostatic pressure so that $P = P_\ell \approx \rho_r gz$, where ρ_r is the mean rock density. At the surface ($z = 0$), P is given by the hydrostatic pressure, $P = P_h = \rho_w gz = 0$. Therefore, if I set the arbitrary reference elevation to the magma intrusion depth, d , then $h(z = d) = h_p \approx \rho_r d / \rho_w$ and $h(z = 0) = h_e = d$. As a result, if I approximate the density ratio between rock and water to be $\rho_r / \rho_w \approx 3$, then for any intrusion depth the hydraulic gradient is

$$\frac{\partial h}{\partial z} = \frac{h_p - h_e}{d} = \frac{3d - d}{d} = 2. \quad (5.30)$$

Substituting Eqs. (5.28) and (5.30) into Eq. (5.29) and recognizing that $A = WL$, yields the vertical hydraulic conductivity,

$$K_z = \frac{Q_w}{2A} = \frac{q_M \rho_M \phi_w}{2\rho_w L}. \quad (5.31)$$

Therefore, K_z is independent of the assumed arc width, W . Applying $L = 1$ km, used for the magma intrusion rate, and approximating the density ratio between magma and water to be $\rho_M / \rho_w \approx 3/1$ reduces Eq. (5.31) to

$$K_z = 1.5 q_M \phi_w \text{ km}^{-1}. \quad (5.32)$$

Eq. (5.32) is independent of intrusion depth, d , because as depth increases, so does the lithostatic pressure, P_ℓ . However, d determines the depth scale for which K_z is determined. As before, within this depth scale, K_z is assumed homogeneous.

Results

I use Eq. (5.32) to determine overall (assumed homogeneous) vertical hydraulic conductivity for the upper 15 km of the crust in the Cascades. As input data I assume a range of magma intrusion rates of $9 \leq q_M \leq 50 \text{ km}^3 \text{ Ma}^{-1} \text{ km}^{-1}$ [19, 84]. Sisson and Layne [175] and other authors [58] suggest a magma water content of about 0.2 to over 3 wt.-% and up to 7 wt.-% for the Cascades arc and the nearby Mt. Shasta region in northern California. Here, I pick 1.5 wt.-% (i.e., $\phi_w = 0.015$). Substituting these values into Eq. (5.32) results in a range of vertical hydraulic conductivities of approximately

$$6 \times 10^{-12} \leq K_z \leq 4 \times 10^{-11} \text{ m/s.} \quad (5.33)$$

5.3 Conversions between κ , K , and k

In order to compare results from the four methods employed in this study I convert hydraulic diffusivity, κ , and hydraulic conductivity, K , to permeability, k . Transferring κ to hydraulic conductivity,

$$K = \kappa S_S \quad (5.34)$$

requires assuming a value for specific storage,

$$S_S = \rho_w g (\alpha + n\beta), \quad (5.35)$$

where n is pore fraction, $\beta = 4.8 \times 10^{-10} \text{ m}^2/\text{N}$ is the compressibility of water, and α is the bulk aquifer compressibility at constant vertical stress and zero lateral strain [198]. Further assumptions about temperature (and pressure) dependent (dynamic) viscosity, μ , and water density, ρ_w , have to be made when converting hydraulic conductivity, K , to permeability, k , using

$$k = \frac{\nu K}{g}, \quad (5.36)$$

where the kinematic viscosity is given by $\nu = \mu/\rho_w$. Estimating α , ρ_w , and μ is not trivial and can lead to large uncertainties in inferred permeability values, particularly when converting from hydraulic diffusivity to permeability, where, in addition to ν , S_S has to be estimated. I assume $\alpha \approx 10^{-10} \text{ m}^2/\text{N}$ for fractured igneous rock [37, 150] and $n \approx 0.01$ [77, 85] yielding $S_s \approx 10^{-6} \text{ m}^{-1}$.

Similar to Germanovich et al. [53], I approximate kinematic viscosity as a function of depth-dependent mean temperature, T_m , for Eq. (5.36) by

$$\nu(T_m) \approx \frac{0.032 \text{ Pa} \cdot \text{s} \cdot ^\circ\text{C}}{\rho_w [1 - \alpha_w T_m] [15.4 \text{ } ^\circ\text{C} + T_m]}, \quad (5.37)$$

where $\alpha_w = 10^{-3} \text{ } ^\circ\text{C}^{-1}$ is the coefficient of thermal expansion of water and $\rho_w = 10^3 \text{ kg/m}^3$ and $\rho_w = 0.5 \times 10^3 \text{ kg/m}^3$ are the water density for mean depths (and associated pressures and temperatures) $z_m \leq 3 \text{ km}$ and $z_m \approx 10 \text{ km}$, respectively. For calculation of z_m and depth ranges (z -ranges) over which the permeability results from the previous section are applicable, I refer to Section 5.4 in conjunction with Table 5.3. The mean temperature for Eq. (5.37) is then given by $T_m \approx T_R + z_m (\partial T / \partial z)_b$ with a typical recharge temperature of $T_R \approx 5 \text{ } ^\circ\text{C}$ (Figures 5.7 and 5.8) and a background temperature gradient of $(\partial T / \partial z)_b \approx 50 \text{ } ^\circ\text{C}/\text{km}$ (Figure 5.7 and Section 5.4.2). Resulting kinematic viscosities, ν , agree to within the implicit uncertainties with compilations by Grigull et al. [57]. As I will show later, the depth ranges over which calculated permeabilities are applicable are independent of the actual permeability values. However,

the z -ranges do depend on the characteristics of the assumed decrease in permeability with depth (exponential versus power-law relationship) and on the calculation of the mean (arithmetic versus harmonic). Table 5.3 summarizes the hydraulic conductivities discussed in the previous section and the resulting permeabilities for the different depth scales.

5.4 Discussion

In Section 5.4.1 I discuss results from the previous two sections and suggest a curve describing permeability as a function of depth. In Section 5.4.2 I address mean background heat-flow values determined in Section 5.2.2.

5.4.1 Heterogeneity and anisotropy of permeability

Permeability typically decreases with depth due to compaction, metamorphism, and/or filling of pore spaces and fractures by precipitating minerals, particularly in hydrothermal regions [17, 45, 82, 130]. In some cases, however, fractures can remain open due to earthquakes providing long-term (10s to 100s of years) high- k pathways [151]. The characteristics of the reduction of k with depth, z , are difficult to determine and are controversial [22, 23, 33, 48, 54, 73, 123]. Several publications [14, 77, 114, 136, 170, 171, 204] as well as this study suggest a non-linear decrease of k with z in the Cascades region and for continental crust in general. Non-linear $k(z)$ -profiles allow for high near-surface permeabilities and related high groundwater recharge rates so that the observed near-surface isothermal and inverted temperature-depth profiles are possible (Figures 5.7, 5.8, and 5.10). At the same time, a non-linear $k(z)$ -profile can reduce permeabilities to $k \leq 10^{-16} \text{ m}^2$ at $z \geq 4 \text{ km}$, thus allowing for conduction-

Symbol	Units	1	2	3	4	5	6
Method		spring dis.	heat-flow	heat-flow	heat-flow	hydroseis.	magma intr.
Section #		5.2.1	5.2.2	5.2.2	5.2.2	5.2.3	5.2.4
x, z		x	x	z	z	z	z
Study Area		A	C1	B	C2	C3	D
EA, EH, PH		EA	EA	EH	EH	PH	PH
$\delta_{\min}, \delta_{\max}$	km	0.2, 0.3	0.2, 0.3	0.2, 0.3	0.2, 0.3	-	-
$\lambda_{\min}, \lambda_{\max}$		-	-	-	-	1, 10	1, 10
$b \pm 0.25b$	km	0.05 ± 0.0125	1 ± 0.25	1.2 ± 0.3	1.2 ± 0.3	4.5 ± 1.125	15 ± 3.75
z -range, z_m	km	0.02 - 0.03, 0.025	0.3 - 0.5, 0.4	0.4 - 0.9, 0.65	0.6 - 1.1, 0.85	1.7 - 4.4, 3	5.6 - 14.8, 10
$(\partial T / \partial z)_b$	°C/km	50	50	50	50	50	50
T_m	°C	6	25	38	48	155	505
P_m	MPa	0.25	4	6.5	8.5	30	100
ρ_m	kg/m ³	10^3	10^3	10^3	10^3	10^3	0.5×10^3
μ_m	Pa · s	1.5×10^{-3}	8×10^{-4}	6×10^{-4}	5×10^{-4}	2×10^{-4}	5×10^{-5}
ν_m	m ² /s	1.5×10^{-6}	8×10^{-7}	6×10^{-7}	5×10^{-7}	2×10^{-7}	1×10^{-7}
K_{\min}	m/s	10^{-3}	10^{-6}	3×10^{-7}	3×10^{-8}	8×10^{-8}	6×10^{-12}
K_{\max}	m/s	10^{-2}	10^{-6}	3×10^{-6}	3×10^{-8}	5×10^{-7}	4×10^{-11}
k_{\min}	m ²	1.5×10^{-10}	8.2×10^{-14}	1.8×10^{-14}	1.5×10^{-15}	1.6×10^{-15}	6×10^{-20}
k_{\max}	m ²	1.5×10^{-9}	8.2×10^{-14}	1.8×10^{-13}	1.5×10^{-15}	1.0×10^{-14}	4×10^{-19}

Table 5.3. Conversions from hydraulic conductivity, K , to permeability, k , in horizontal, x , and vertical, z , directions, based on Eqs. (5.36) and (5.37). The average of the z -range, z_m , is calculated using combinations of min/max values for the aquifer depths, $b \pm 25$ %, skin depths, δ , and/or exponents, λ , for exponential, E, or power-law, P, functions, respectively. The exponential solution, E, for the z -range is used for $b \leq 2$ km, both for subhorizontal (parallel) pathways (Eq. 5.48) and for subvertical (serial) pathways (Eq. 5.45) that are calculated using the arithmetic mean, A, and the harmonic mean, H, permeability expressions, respectively. The power-law solution, P, is reserved for mean depths $z_m > 1$ km and is determined only for subvertical (serial) pathways (Eq. 5.46) that are characterized by harmonic mean, H, permeability values. Hydraulic conductivity for column 5 (Section 5.2.3) is based on results for vertical hydraulic diffusivity, \mathcal{K}_z , and assuming $S_S \approx 10^{-6} \text{ m}^{-1}$ in Eq. (5.34) as discussed in Section 5.3. Uncertainties in K and k (columns 2 and 4) are based on uncertainties calculated for k in columns 1, 3, 5, and 6.

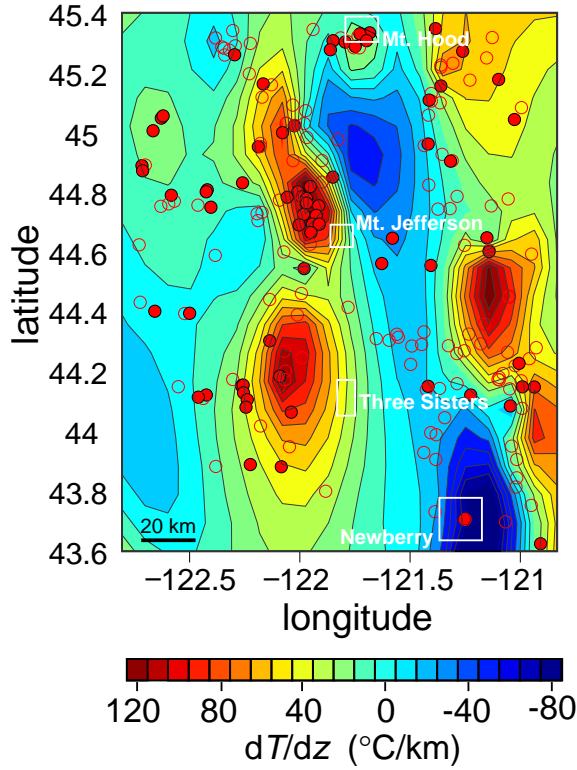


Figure 5.10. Map of near-surface temperature gradients in study region E (Figure 5.1), based on interpolation of geotherm data from drill holes (circles). Isothermal and inverted temperature gradients exist in high precipitation and groundwater recharge areas such as the high-relief volcanos. Cold groundwater is heated at depth, the heat is advected and discharged at hot springs [84, 85].

dominated heat transfer at these depths, as also required by observations [85]. A transition from advection- to conduction-dominated heat transfer at $k \approx 10^{-16} \text{ m}^2$ has been suggested by numerous authors [29, 66, 73, 77, 113, 114, 132, 178].

In Section 5.2.2, I invoked non-linearity by decreasing permeability exponentially with depth. Figure 5.5 shows streamlines for constant (thin curves) and exponentially decreasing (bold curves) k , where recharge rates for the latter are about nine times larger than for constant k (Figure 5.7a). The exponential $k(z)$ -curve results in larger horizontal groundwater flow components at smaller depths, rapidly reducing vertical

groundwater flow velocities and allowing for conduction-dominated heat transfer at relatively shallow depths.

However, while exponential functions of (vertical) permeability, such as

$$k_z(z) = k_{zs}e^{-z/\delta}, \quad (5.38)$$

provide reasonable near-surface (denoted with the subscript “s”) values, including $k_z(z = 0) = k_{zs}$, they also reduce permeability to unrealistically low magnitudes at depths greater than about 2 km (Figure 5.11). In contrast, power laws, such as

$$k_z(z) = k_{zD} \left(\frac{z}{D} \right)^{-\lambda}, \quad (5.39)$$

provide larger, and thus more realistic, permeabilities at greater depths, but approach infinity for $z \rightarrow 0$ and result in a singularity for $z = 0$. They are thus defined for a finite depth, D , i.e., $k_z(z = D) = k_{zD}$.

Due to these advantages and limitations of either function, I suggest Eq. (5.38) for $0 \leq z \leq 0.8$ km and Eq. (5.39) for $z > 0.8$ km. Eq. (5.39) is equivalent to the curve suggested by Manning and Ingebritsen [114] if $\lambda = 3.2$ and $k_{zD} = 10^{-14} \text{ m}^2$ at $D = 1$ km are chosen. In general, units of z and D have to be identical (e.g., both m or both km). My results from Section 5.2.2 suggest $\delta \approx 250$ m and $k_{zs} \approx 5 \times 10^{-13} \text{ m}^2$ for Eq. (5.38). For these values of λ , k_{zD} , δ , and k_{zs} , as well as depth $z \approx 0.8$ km, the vertical permeabilities and their gradients,

$$-\frac{k_{zs}}{\delta}e^{-z/\delta} \approx -\frac{k_{zD}\lambda D^\lambda}{z^{\lambda+1}}, \quad (5.40)$$

are similar, thus enabling the suggested transition from Eq. (5.38) to Eq. (5.39) at $z = 0.8$ km (Figure 5.11).

The methods employed and conversions discussed in Sections 5.2 and 5.3 provide estimates of mean permeability, \bar{k} , at four depth scales, mostly in vertical, but in

two cases also in approximately horizontal, directions. The spring discharge model (Section 5.2.1) of study region A (Figure 5.1) yields an estimate of mean horizontal permeability, \bar{k}_x , because the method considers individual near-surface aquifers that consist of slope-parallel, and thus roughly horizontally-layered, lava flows. Within such solidified lava flows (or aquifers), water can flow primarily through the (about parallel and horizontal) pathways of highest permeability. Thus, the mean horizontal permeability is given by the arithmetic mean [106],

$$\bar{k}_x = \frac{1}{b} \sum_{i=1}^N k_{x_i} b_i, \quad (5.41)$$

where the subscript i denotes the i^{th} layer or pathway, b_i is the thickness of layer i , and b is the total thickness of all layers.

In contrast, vertical groundwater flow across horizontal lava flows (or aquifers) is passing through sections of varying permeability in series, so that mean vertical permeabilities are typically determined by the harmonic mean [106],

$$\bar{k}_z = b \left(\sum_{i=1}^N \frac{b_i}{k_{z_i}} \right)^{-1}, \quad (5.42)$$

where \bar{k}_z is dominated by the lowest permeabilities along that path. Hence, in volcanic or sedimentary settings, where slope-parallel, and thus approximately horizontal, layers, pathways, and aquifers are common, typically $10 \leq \bar{k}_x/\bar{k}_z \leq 1000$, at least near the surface [33].

A further consequence of \bar{k}_z being determined by the harmonic mean (Eq. 5.42) and $k_z(z)$ generally decreasing with depth is that my \bar{k}_z results from Section 5.2 apply predominantly towards the lower portions of the considered depth ranges. Replacing the discrete layer formulation in Eq. (5.42) with the definite integral from zero to b of the continuous functions, Eqs. (5.38) and (5.39), results in the harmonic mean

vertical permeabilities

$$\overline{k}_z = \frac{bk_{zs}}{\delta(e^{b/\delta} - 1)} \quad (5.43)$$

and

$$\underline{k}_z = k_{zD} \left(\frac{D}{b} \right)^\lambda (\lambda + 1) \quad (5.44)$$

suggested for $0 \leq z \leq 0.8$ km and $z > 0.8$ km, respectively. Setting Eq. (5.38) equal to Eq. (5.43) and Eq. (5.39) equal to Eq. (5.44) provides the depths

$$\overline{z}_z = -\delta \ln \left[\frac{b}{\delta(e^{b/\delta} - 1)} \right] \quad (5.45)$$

and

$$\underline{z}_z = b(\lambda + 1)^{-1/\lambda}, \quad (5.46)$$

where \overline{k}_z and \underline{k}_z are reached, respectively. Here, over- and underbars denote functions applicable to shallow (based on Eq. 5.38) and deeper (based on Eq. 5.39) depths, respectively. As before, b is the considered depth scale. Eqs. (5.45) and (5.46) are independent of the actual permeability value but depend on the characteristics of the decrease in permeability with depth (exponential versus power-law relationship). I use Eq. (5.45) for depths shallower than about 1 km, Eq. (5.46) for depths greater than approximately 1 km, and ranges of $200 \leq \delta \leq 300$ m, $1 \leq \lambda \leq 10$, and $b \pm 0.25b$ to determine the applicable depth ranges (Table 5.3 and Figure 5.11) for the respective values of \overline{k}_z and \underline{k}_z , determined in Section 5.2.

For the shallow-most model (Section 5.2.1 and study region A in Figure 5.1) the arithmetic mean horizontal permeability is determined. Here, each horizontal layer's permeability is assumed to decrease with depth according to Eq. (5.38). As before, I replace the discrete formulation of the arithmetic mean (Eq. 5.41) with the definite vertical integral from zero to b of the continuous function (Eq. 5.38) resulting in the

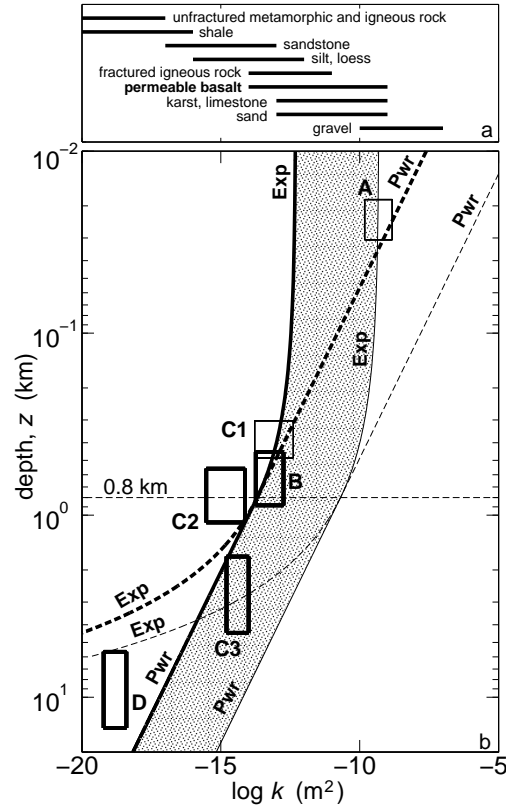


Figure 5.11. a) Approximate (near-surface) range of permeability values (after Freeze and Cherry [47]). The (Oregon) Cascades primarily consist of basalt and basaltic andesite where youngest (< 2.3 Ma) rock units show high near-surface permeabilities of $k \approx 10^{-14}$ m² [81, 85], consistent with the k -range indicated for permeable basalts. b) Permeability, k , as a function of depth, z . Shown are the results for study regions A,B,C, and D (Figure 5.1 and Table 5.3) for horizontal (thin boxes) and vertical (bold boxes) permeabilities. The depth ranges are determined as described in the main text and in the caption to Table 5.3. Box widths reflect approximate variations in permeability. Superimposed is the exponential profile of Eq. (5.38), denoted Exp, with $\delta = 250$ m and $k_{zs} = 5 \times 10^{-13}$ m² for vertical (bold curve) and $k_{xs} = 5 \times 10^{-10}$ m² for horizontal (thin curve) permeabilities. Also shown is the power law profile of Eq. (5.39), denoted Pwr, with $\lambda = 3.2$ and $k_{zD} = 10^{-14}$ m² at $D = 1$ km as suggested by Manning and Ingebritsen [114] for vertical (bold line) permeability. $k_{zD} = 10^{-11}$ m² is used for horizontal (thin line) permeabilities. Solid lines indicate the permeability-depth curves suggested with a transition from exponential to power-law profile at a depth of 0.8 km (dashed horizontal line). The dotted area indicates the expected range between vertical and horizontal permeability. At depth this range between k_x and k_z may be expected to reduce (not shown here).

arithmetic mean horizontal permeability given by

$$\overline{k}_x = \frac{\delta k_{zs}}{b} (1 - e^{-b/\delta}). \quad (5.47)$$

Setting Eq. (5.38) and Eq. (5.47) equal yields the depth,

$$\overline{z}_x = -\delta \ln \left[\frac{\delta}{b} (1 - e^{-b/\delta}) \right], \quad (5.48)$$

where \overline{k}_x is reached, based on the suggested ranges of maximum near-surface aquifer depths (thicknesses), $b = 50 \text{ m} \pm 25 \%$, and skin depths $200 \leq \delta \leq 300 \text{ m}$ (Table 5.3). The values for δ are inferred from my heat-flow model (Section 5.2.2). As before, the overbars denote functions applicable to shallower depths.

Figure 5.11b shows the results for \overline{k}_x , \overline{k}_z , and \underline{k}_z from Section 5.2 at depths \overline{z}_x , \overline{z}_z , and \underline{z}_z determined using Eqs. (5.48), (5.45), and (5.46), respectively. This approach allows me to base depths, for which the permeability results are applicable, on the shape of the $k(z)$ -curve (exponential versus power-law) and the method of calculating the mean (arithmetic versus harmonic). Therefore, while this technique does not use the actual (near-surface) permeability values, it requires assuming a model describing the change of permeability with depth (Eqs. 5.38 and 5.39). While the equations appear to describe $k_z(z)$ -profiles in principle, the appropriate parameters are not well-constrained and depend largely on the local geology. I thus use a wide range of values for δ , λ , and particularly b , as suggested previously, to calculate depth ranges (i.e., uncertainties) over which the mean permeabilities are applicable (Table 5.3).

I recognize that my depth ranges are partially based on assuming that Eq. (5.39) applies for mean depths $z_m > 1 \text{ km}$ and are thus dependent on the curve suggested by Manning and Ingebritsen [114], with $\lambda = 3.2$. However, I can use a wide range of $1 \leq \lambda \leq 10$ values to calculate a range of \underline{z}_z using Eq. (5.46). For shallower mean depths of $0 \leq z_m \leq 1 \text{ km}$, I employ my suggested Eqs. (5.45) and (5.48) that are

instead based on Eq. (5.38) and use $200 \leq \delta \leq 300$ m to determine ranges of \bar{z}_z and \bar{z}_x . For either method I estimate independently a large uncertainty range in $b \pm 25$ %. Thus, while \underline{z}_z is not completely decoupled from $\lambda = 3.2$, the depth range is nonetheless based on an independent estimate of maximum depth b , a wide range of λ , and the reasonable assumption that the mean horizontal and vertical permeabilities are given by the arithmetic and the harmonic means, respectively, if approximately horizontal layers are present.

Given the previous considerations, I suggest that my results for $k_z(z)$ and $k_x(z)$ in the Oregon Cascades are largely independent from, but comparable to, the permeability-depth profile suggested by Manning and Ingebritsen [114] for the continental crust. However, I propose that for depths smaller than about 0.8 km, Eq. (5.38) with $k_{zs} \approx 5 \times 10^{-13}$ m² and $\delta \approx 250$ m is more appropriate at least for the Cascades and possibly for continental crust in general.

For example, Shmonov et al. [170] suggest a near-surface permeability of approximately $k_s \approx 2.75 \times 10^{-13 \pm 1.9}$ m² that decreases to $1.67 \times 10^{-20 \pm 1.5}$ at 40 km depth based on experimental data on the permeability of samples of amphibolite and gneiss from the Kola Ultradeep Borehole. Furthermore, Patriarche et al. [136] invoke an exponential relationship between depth and hydraulic conductivity analogous to Eq. (5.38) with $\delta \approx 0.28$ km to satisfy both hydraulic head model calibration and measured ⁴He concentrations in the sedimentary Carrizo aquifer in Texas. Because of the similarity of their δ value to the one introduced here, their $K(z)$ -curve (converted to $k(z) = K\nu/g \approx 10^{-7}K$) has a similar shape as my exponential $k(z)$ -curve. Their zero-depth permeability of 2×10^{-11} m² is based on a near-surface hydraulic conductivity of the aquifer of about 2×10^{-4} m/s. Finally, measurements from the German Continental Deep Drilling Program (KTB) [73] show even lower near-surface

permeabilities of 5×10^{-18} to 3×10^{-16} m², however, with no clear depth-dependence.

A further advantage of using Eq. (5.38) for shallow depths is that the function provides a finite near-surface permeability of k_{zs} as depth approaches zero. In contrast, Eq. (5.39) diverges towards infinity for $z \rightarrow 0$ and results in a singularity at $z = 0$. This limitation of Eq. (5.39) may not be critical for global studies of permeability, where overall estimates over larger depth scales ($z > 0.5$ km) may be desired. In fact, for $z > 2$ km, Eq. (5.39) is preferred because at greater depths its permeability gradient is smaller than the one for Eq. (5.38), providing more realistic deeper permeabilities. Therefore, I propose a transition from Eq. (5.38) to Eq. (5.39) at $z = 0.8$ km. This transition is relatively smooth as permeabilities and their gradients (Eq. 5.40) are comparable at $z = 0.8$ km (Figure 5.11b) for the suggested values of $k_{zs} \approx 5 \times 10^{-13}$ m², $\delta \approx 250$ m, $k_{zD} \approx 10^{-14}$ m², and $\lambda = 3.2$ (the latter two values are adopted from Manning and Ingebritsen [114] and corroborated by this study).

Of course there are large variations in permeability as a function of lithology [47] particularly at zero depth (Figure 5.11a). However a maximum value may be reached at about $k \approx 10^{-7}$ m² for gravel (Figure 5.11a). A more typical upper limit for continental crust in general may be $k \approx 10^{-12}$ m² (Table 1 and Figure 8 in Manning and Ingebritsen [114]) at least in the vertical direction across horizontal layers. Such a low maximum average permeability further supports the exponential $k_z(z)$ -relationship with the suggested finite near-surface value of about $k_{zs} \approx 5 \times 10^{-13}$ m² (Figure 5.11b) for vertical groundwater flow across sub-horizontal lava flows or sedimentary layers and in the absence of near-vertical fractures.

However, if sub-vertical fractures and faults are present, high- k_z pathways can alter the relationship between depth and permeability. Hence, I suggest that my elevated values of $k_z \approx 10^{-15}$ m² at $z_m \approx 3$ km (Table 5.3 and Figure 5.11), deter-

mined by the hydroseismicity method (Section 5.2.3), are due to faults located on the southern flanks of Mt. Hood, such as the White River fault. These faults, that are located away from the volcano’s central axis, show predominantly normal-fault focal mechanisms [92] and thus suggest tectonically-driven (possibly hydrologically-triggered [159]) earthquakes, rather than magma-flow-induced seismicity that is typically characterized by non-double couple focal mechanisms [38]. High values of k allow for advective heat transfer and hot springs, where water can reach the surface faster than heat diffusion time scales required for thermal equilibration with the surrounding rock. Indeed, the only two off-centered hot spring areas (Meadows Spring and Swim Warm Springs) observed at Mt. Hood to date [127] are located on the southern flanks of the volcano close to the earthquakes’ epicenters (Figure 5.6). Therefore, I suggest that the slightly elevated \bar{k}_z values inferred for mean applicable depths of about $z_m = 3$ km in study region C3 (Figure 5.1 and Table 5.3) reflect the permeability of a large representative elementary volume that is dominated by normal faults that are being kept permeable by hydroseismicity [151, 190]. In addition, vertical faults are approximately parallel to each other, thus providing parallel pathways whose combined mean permeability is dominated by the highest- k pathways which is determined by the larger arithmetic mean (Eq. 5.41), rather than by the smaller harmonic mean (Eq. 5.42) [154].

Scale-dependence of permeability is controversial [13, 22, 23, 28, 79, 148, 154, 162, 190, 211]. In general, permeability tends to increase, as the representative elementary volume increases from laboratory rock-core measurements, over in-situ field measurements, to large-scale regional models, as those considered in this study. This relationship may be the case because large-scale heterogeneities, that may include high permeability pathways, are more likely to be sampled if larger volumes are considered. For example this appears to be the case in the hydroseismicity model described in the

previous paragraph. However, an upper bound appears to be reached at the upper field and regional modeling scale [28, 162], possibly because most heterogeneities have been included [148].

5.4.2 Basal heat-flow, H_b

Figure 5.10 shows a map of vertical near-surface heat-flow for study region E in Figure 5.1. The near-surface results are based on a multi-quadratic interpolation technique [131] applied to 209 geotherm boreholes and $K_{Tr} = 2 \text{ W}^\circ\text{C}^{-1}\text{m}^{-1}$ [16, 80, 83]. High precipitation ($\sim 2 \text{ m/year}$) and infiltration rates ($\sim 1 \text{ m/year}$) in the Oregon Cascades cause isothermal (and sometimes inverted) near-surface geotherm profiles (Figures 5.7a, 5.8, and 5.10) effectively masking the background heat-flow [84, 85]. I minimize the mean absolute error, ϵ , between data and calculated temperature values and infer a thermal gradient of about $(\partial T/\partial z)_b \approx 40^\circ\text{C/km}$ at Santiam Pass, located between two volcanos, Three-Fingered Jack and Mt. Washington (Figure 5.7a). Connecting the deepest two data points yields $(\partial T/\partial z)_b \approx 90^\circ\text{C/km}$. However, the last data point was taken as drilling progressed [16]. Deeper portions of the linear temperature-depth profiles at Mt. Hood volcano (Figure 5.8) yield $(\partial T/\partial z)_b \approx 65^\circ\text{C/km}$. Therefore, I infer a mean background heat-flow, H_b , for the study region of approximately

$$0.080 \leq H_b \approx k_{Tr} \left(\frac{\partial T}{\partial z} \right)_b \leq 0.130 \text{ W/m}^2, \quad (5.49)$$

where the lower and upper heat-flow values are inferred from the study of Santiam Pass and Mt. Hood, respectively (Table 5.2). These values are consistent with the more extensive studies of Blackwell et al. [18] and Ingebritsen et al. [81]. As expected for a region showing active volcanism, heat-flow is elevated with respect to global average values for continents of about 0.065 W/m^2 [143].

5.5 Conclusions

I employ analytical and numerical modeling techniques to estimate permeability at different depth scales for the Oregon Cascades. My results suggest that for depths shallower than about 0.8 km, permeability decreases exponentially with depth, with a skin depth of $\delta \approx 250$ m, from a near-surface value of $k_{zs} \approx 5 \times 10^{-13}$ m².

For depths larger than about 1 km, permeability appears to decrease according to a power law as suggested by Manning and Ingebritsen [114] with an exponent of $\lambda \approx 3.2$ and a permeability of $k_{zD} \approx 10^{-14}$ m² at depth $z = 1$ km. Therefore, I propose

$$k_z(z) = \begin{cases} 5 \times 10^{-13} \text{ m}^2 \exp\left(\frac{-z}{0.25 \text{ km}}\right) & \text{for } 0 \leq z \leq 0.8 \text{ km} \\ 10^{-14} \text{ m}^2 \left(\frac{z}{1 \text{ km}}\right)^{-3.2} & \text{for } z > 0.8 \text{ km,} \end{cases} \quad (5.50)$$

where the parameters for $z > 0.8$ km are adopted from Manning and Ingebritsen [114]. The advantage of using two functions in Eq. (5.50) is that they provide realistic vertical permeabilities for both small ($z < 0.5$ km) and large ($z > 2$ km) depths which neither function alone could both achieve, as discussed in Section 5.4.1. In addition, the functions in Eq. (5.50) yield a relatively smooth transition at $z = 0.8$ km, where their permeabilities and their permeability gradients are similar.

I also determine horizontal permeabilities at depths shallower than about 1 km. At least near the surface, and in the absence of vertical fractures, horizontal permeabilities are typically one to three orders of magnitude larger in volcanic or sedimentary settings where slope-parallel, and thus approximately horizontal, layers, pathways, and aquifers are common.

I note a divergence from Eq. (5.50) for my hydroseismicity model that suggests about one order of magnitude higher permeability values. However, higher perme-

abilities in this region may be consistent with advective heat transfer along active faults causing observed hot springs.

Finally, the coupled heat and groundwater transfer models suggest mean background heat-flow values of about $H_b \approx 0.080$ to $H_b \approx 0.134$ W/m² for the investigated region in the Oregon Cascades. The higher background heat-flow values are associated with volcanic centers that may have magma sources at shallower depths.

Because large-scale hydrogeologic models are generally underconstrained, it is desirable to utilize multiple direct and indirect observations to improve simulations, as described in the introduction to this chapter. In this study, I use classic hydrogeologic boundary conditions and parameters as well as temperature and seismic data, and estimates of magma intrusion rates. Further improvements in future work may include additional constraints such as water chemistry and multi-phase fluid flow, particularly at greater depths.

Lithological variations can cause a wide range of permeabilities. Therefore, it is important to emphasize that the general relationship between depth and permeability suggested here provides only a large-scale average estimate. This estimate was developed for the volcanic (Oregon) Cascades but may also apply to continental crust in general including sedimentary basins where near-horizontal layers are present. However, the suggested $k(z)$ -relationship is not a substitute for more lithologically-specific measurements of k for a given region of interest. Frequently such direct permeability measurements are, however, technically or economically not feasible at greater depths or over large regional scales. In such cases, estimates of the depth dependence of permeability, as presented here, can be useful.

Chapter 6

Glacier-induced volcanism

6.1 Introduction

Similar to hydroseismicity discussed in Chapter 4, a decrease in confining pressure in the subsurface, due to a reduction in the load exerted by surface water or ice, can cause dike propagation and volcanism. In fact, volcanic activity may be modulated by several external physical processes affecting the stress regime and acting over a wide range of time scales. At short time scales volcanic eruptions may be triggered by Earth tides [64, 91, 118, 180]), short term climatic effects [146] and daily variations in atmospheric pressure and temperature[128]. Annual periodicity is also sometimes observed [121]. At long periods (i.e., greater than hundreds of years) it has been suggested that volcanism is influenced by changes in sea level [119, 197] and by ice loading [56, 63, 93, 126, 172]. In addition, at long periods, both changes in hydrothermal circulation [117] and melt productivity [107, 177] have been invoked.

Glazner et al. [56] suggest that glacial ice thickness and volcanism are anticorrelated in eastern California over the past 800 kyr. While this relationship appears to

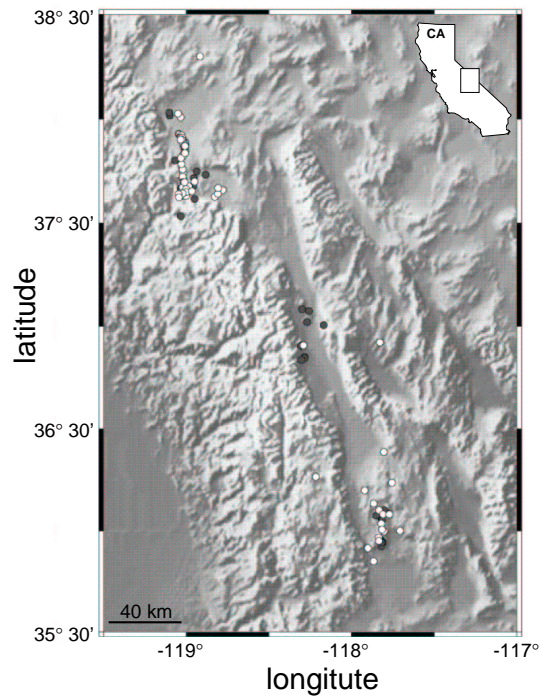


Figure 6.1. Shaded relief map with locations of basaltic (dark circles) and silicic (white circles) eruptions in Long Valley and Owens Valley volcanic fields in eastern California during the past 400 kyr.

hold true, a stronger correlation between the rate of change of glaciation and volcanic eruptions is suggested here. The hypothesis is that the volcanism in Long Valley and Owens Valley volcanic fields (Figure 6.1) is a response controlled by the dynamics of dike formation, which in turn is influenced by the rate of change of ice volume rather than the total ice volume. Moreover, the responses for basaltic and silicic systems is distinctive. The difference in response time allows for constraining critical magma chamber overpressures required for volcanic eruptions as well as mechanical properties of the wall rock governing rhyolitic and basaltic dike formation. The results are consistent with basaltic magmas being generated at greater depths than rhyolitic

(hereafter referred to as silicic) magmas, in accord with geochemical observations.

6.2 Data analysis

I employ signal processing techniques on time series of volcanic eruptions and glaciation (Figure 6.2a). Eruption data is provided by Glazner et al. [56] and Glazner [55] and is divided into basaltic and silicic categories (Figure 6.1). Glaciation is assumed here to be proportional to ice thickness and is approximated by oxygen isotopic data, $\delta^{18}\text{O}$, from the SPECMAP time series [120, 166]. Here, peaks in $\delta^{18}\text{O}$ correspond to glacial times. Figure 6.2a shows the original time series for basaltic and silicic eruptions as well as for $\delta^{18}\text{O}$ for the past 400 kyr. The sparse data available for eruptions before 400 kyr is not used because individual eruptions would dominate the analysis. Also shown in Figure 6.2a are binned eruption numbers where the bin width is 1 kyr. In order to be able to compare the data at equivalent frequency bands, I smooth the time series by convolving them with a Gaussian kernel with a width of 23 kyr. As a test, I also smooth the data using a moving polynomial interpolation (Appendix A.3), where the polynomial order used in each segment is ≤ 5 . The latter method is equivalent to the one employed in Chapter 4 and by Saar and Manga [159] and ensures that no artificial frequencies are introduced. Both techniques yield similar results. Therefore, in the following I present results based on the convolution method because it is similar to the approach reported by Glazner et al. [56] and thus allows for easier comparison. Interpolating the binned data also provides the continuous functions B and S for basaltic and silicic eruptions, respectively, on which standard spectral analyses can be performed.

Figure 6.4 shows power spectra for the interpolated and smoothed time series

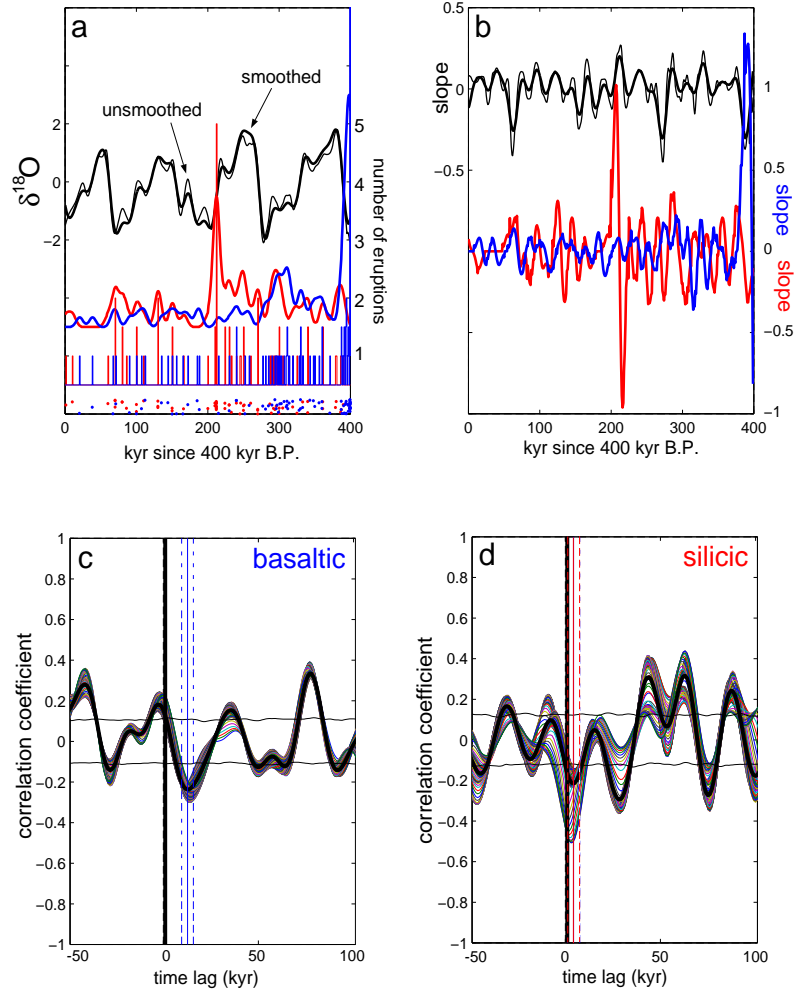


Figure 6.2. Original, binned, interpolated, differentiated, and cross-correlated data for basaltic (blue) and silicic (red) volcanic eruptions, as well as glaciation (black) approximated by $\delta^{18}\text{O}$ SPECMAP data. a) Original $\delta^{18}\text{O}$ data (thin black curve) and smoothed (by convolution with a 23-kyr-width Gaussian kernel) data (bold black curve). Original volcanic eruption numbers are shown as dots, binned eruption numbers as bars, and interpolated (by same kernel as above) eruption numbers as curves. b) Derivative of original (thin curve for $\delta^{18}\text{O}$ only) and interpolated (bold) curves from panel a. c) Normalized correlation coefficients versus time lag of 100 moving cross-correlations for curves from panel b. The bold black curve indicates the mean of the 100 moving cross-correlations (see Figure 6.3). Thin black curves indicate upper and lower bounds of the 90% confidence intervals for random eruption number distributions. The time lag and its 2- σ standard deviation is shown by the vertical solid and dashed lines, respectively. d) Same as c) but for silicic eruptions.

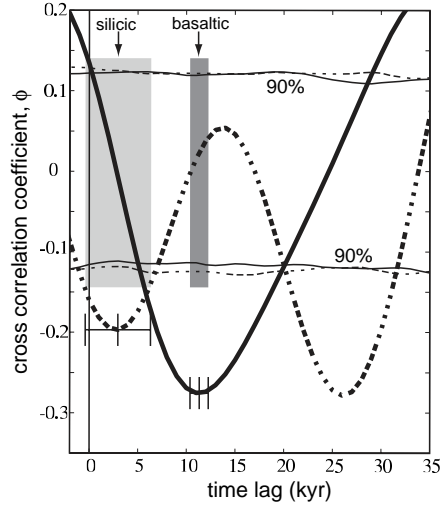


Figure 6.3. Mean correlation coefficients from Figure 6.2c,d for cross-correlations between derivatives of $\delta^{18}\text{O}$ and derivatives of basaltic (solid) and silicic (dashed) eruption numbers. Statistically significant anticorrelations, that are distinct from the 90% confidence limits for random occurrences of basaltic (solid) and silicic (dashed) eruptions are given at time lags of 11.3 and 3.3 kyr, respectively.

from Figure 6.2a. A distinctive peak is observed in all three data sets at a period of about 40 kyr, suggesting that the characteristic time scale for a full glacial cycle (i.e., advance and retreat) is reflected in the volcanic record. Hence, melting glaciers do indeed appear to cause volcanic eruptions in eastern California.

In order to compare quantitatively the rate of change in the time series, I compute moving normalized unbiased cross-correlations, $\Phi_{fg}(t)$ (Eqs. 4.3 and 4.4 in Chapter 4), between the derivative of the SPECMAP time series, $f = \delta^{18}\text{O}' = d\delta^{18}\text{O}/dt$, and the derivatives of the basaltic, $g = B' = dB/dt$, and silicic, $g = S' = dS/dt$, time series (Figure 6.2b) on overlapping segments. The segment width is 300 kyr and the step size is 1 kyr resulting in 100 segments. 90% confidence intervals are determined for cross-correlations of random distributions of B' or S' . This is achieved by performing 10

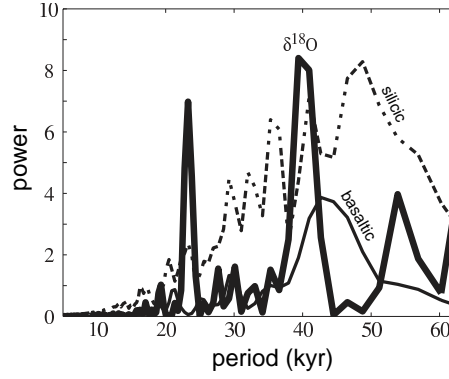


Figure 6.4. Power spectra of the interpolated (bold curves) data from Figure 6.2a (thus no short periods, i.e., high frequencies are present).

cross-correlations per segment, resulting in 1000 correlation calculations during which one of the time series is assigned random phases for each frequency so that its auto-correlation is unaffected (Appendix A.4). Moving cross-correlations are chosen to reduce the dominating effects of (locally) highly correlated segments of the time series. The segment width of 300 kyr is significantly higher than the dominant period in the time series of about 40 kyr (Figure 6.4) so that multiple periods contribute to the calculation of each cross-correlation coefficient. At the same time, the segment width is sufficiently small to allow for 100 (moving) cross-correlation calculations at the given step size of 1 kyr and the time series length of 400 kyr. Moving cross-correlations also provide uncertainties for the time lags. Time lags for cross-correlations $\Phi_{\delta^{18}\text{O}'B'}(t)$ and $\Phi_{\delta^{18}\text{O}'S'}(t)$ are found to be approximately $\Gamma = 11.3 \pm 1.0$ kyr and $\Gamma = 3.0 \pm 3.4$ kyr, respectively (Figures 6.2c,d and 6.3), where the uncertainty reflects 2σ standard deviations.

6.3 Discussion

In a model developed by Jellinek and DePaolo [89] the evolution of overpressure, $\Delta p_{ch} = (p_{ch} - \sigma_r)$, within a shallow (5 km depth) spherical magma chamber contained in a Maxwell viscoelastic wall rock is given by

$$\frac{d\Delta p_{ch}}{dt} = \frac{E}{\mu_{wr}}(\Delta p_{max} - \Delta p_{ch}), \quad (6.1)$$

where Δp_{ch} is the pressure in the chamber, σ_r is the remote lithostatic stress, and E and μ_{wr} are the elastic modulus and the effective viscosity of the wall rock, respectively. Here, Δp_{max} is the maximum sustainable magma chamber overpressure. For a given magma supply rate, effective wall rock viscosity, and magma chamber volume, Δp_{ch} is approximately constant. Dike formation is expected to lead to volcanic eruptions if $\Delta p_{max} > \Delta p_{crit}$, where Δp_{crit} is the critical overpressure required to propagate a dike from the chamber to the surface, resulting in an eruption. In principal, glacial unloading can influence both the confining lithostatic stress retarding dike formation as well as the rate of decompression melting in the mantle, which governs the long term magma supply [93]. However, the time lags identified in Figure 6.3 show that glacial unloading affects rhyolitic and basaltic volcanism differently. This observation is inconsistent with volcanism being caused by a uniform increase in the magma supply resulting from enhanced decompression melting. Moreover, mantle-derived basalts are likely to form at depths greater than about 50 km [34], which is comparable to the order 100 km width of Sierra ice sheets, hence, is an approximately linear surface load, where the lateral extent may be neglected. Stresses resulting from such loads fall off as $1/r^3$, where r is the radial distance from the center [189]. Thus the effect of glacial loading and unloading in the Sierras on underlying mantle melting is expected to be small.

In contrast to changing the magma supply, the influence of glacial unloading on the stresses retarding dike formation from a shallow (5 km deep) magma chamber may be sufficiently large to influence eruption frequency. To investigate this possibility the constant source term in Eq. (6.1) is replaced with the rate of change of glacial unloading, i.e.,

$$\frac{E}{\mu_{wr}}\Delta p_{ch} = -\frac{d\Delta p_f}{dt}, \quad (6.2)$$

resulting in a new equation for the evolution of magma chamber overpressure,

$$\frac{d\Delta p_{ch}}{dt} + \frac{E}{\mu_{wr}}\Delta p_{ch} = -\frac{d\Delta p_f}{dt}. \quad (6.3)$$

Nondimensionalizing Eq. (6.3) by making the substitutions $p_{ch} = \Delta p_{ch}/\Delta p_{crit}$, $P_f = \Delta p_f/\Delta p_{crit}$, and $\tau = t/\tau_m$, where

$$\tau_m = \frac{\mu_{wr}}{E} \quad (6.4)$$

is the Maxwell relaxation time [192], reduces Eq. (6.3) to

$$\frac{dp_{ch}}{d\tau} + p_{ch} = -\frac{dp_f}{d\tau}. \quad (6.5)$$

To further compare the model with data it is useful to look at the solution to Eq. (6.5) in the frequency domain given by

$$i\omega P_{ch} + P_{ch} = -i\omega P_f, \quad (6.6)$$

where P is the fourier transform of p , the complex number i is given by $i^2 = -1$, and ω is frequency. The transfer function, $H(\omega)$, relating the glacial forcing pressure, P_f (input signal), to the chamber pressure, P_{ch} (output signal), is thus given by the spectral division (deconvolution in the time domain)

$$H(\omega) = \frac{P_{ch}}{P_f} = -\frac{i\omega}{i\omega + 1}. \quad (6.7)$$

Multiplying Eq. (6.7) by $(i\omega - 1)/(i\omega - 1)$ and rearranging yields

$$H(\omega) = -\frac{\omega^2}{\omega^2 + 1} - \frac{i\omega}{\omega^2 + 1}, \quad (6.8)$$

where $-\omega^2/(\omega^2 + 1)$ and $-\omega/(\omega^2 + 1)$ are the real, \Re , and imaginary, \Im , terms of $H(\omega) = \Re\{H(\omega)\} + i\Im\{H(\omega)\}$, respectively. As usual, the amplitude and phase of $H(\omega)$ are given by [24]

$$A_H(\omega) = \sqrt{\Re^2\{H(\omega)\} + \Im^2\{H(\omega)\}} \quad (6.9)$$

and

$$\phi_H(\omega) = \tan^{-1} \left[\frac{\Im\{H(\omega)\}}{\Re\{H(\omega)\}} \right], \quad (6.10)$$

respectively. Substituting the real and imaginary terms of Eq. (6.8) into Eqs. (6.9) and (6.10) results in the amplitude

$$A_H(\omega) = \frac{\omega}{\sqrt{\omega^2 + 1}} \quad (6.11)$$

and the phase

$$\phi_H(\omega) = \tan^{-1} \left(\frac{1}{\omega} \right), \quad (6.12)$$

of $H(\omega)$, respectively. Because frequency $\omega > 0$, Eq. (6.12) becomes

$$\phi_H(\omega) = \frac{\pi}{2} + \tan^{-1}(-\omega). \quad (6.13)$$

The amplitude of the transfer function, $A_H(\omega)$ given by Eq. (6.11), is the amplitude of the output, $A_{P_{ch}}$, divided by the amplitude of the input, A_{P_f} , and describes the amplitude filtering characteristics of the magmatic system (Figure 6.5). Physically, the output (dike propagation and volcanism) is given by the critical magma chamber overpressure, Δp_{crit} . The input or forcing (glacial unloading) is given by the rate of change of unloading (Eq. 6.2) also given as unloading per (glacial) forcing time scale,

$\Delta P_{crit}/\tau_f$. Figure 6.6 shows this physical interpretation of the transfer function, $H(\omega) = \text{output}/\text{input}$, normalized by the Maxwell time scale, i.e.,

$$H(\omega) = \frac{\Delta P_{crit}\tau_f}{\Delta P_f\tau_m}, \quad (6.14)$$

versus forcing frequency, $1/\tau_f$, also normalized by τ_m , resulting in τ_m/τ_f .

Physically, a phase lag of $\phi_H(\omega) = 2\pi$ radians in Eq. (6.13) corresponds to a full glacial cycle (i.e., growth and retreat) with a forcing period of $\tau_f \approx 40$ kyr (Figure 6.4). Consequently, the phase lag, $\phi_H(\omega)$, or equivalently the time lag, Γ , provide information about the temporal response of the magmatic system as a function of forcing frequency $1/\tau_f$. Time lags between the rate of glacial retreat, approximated by $\delta^{18}\text{O}'$, and the increase in the frequency of both basaltic, B' , and silicic, S' , eruptions are determined in Section 6.2. Time lags, Γ , and phase lags, $\phi_H(\omega)$, are related by

$$\phi_H(\omega) = \frac{2\pi\Gamma}{\tau_f}. \quad (6.15)$$

Figure 6.6 shows $\phi_H(\omega)$, determined from time lags, Γ , using Eq. (6.15), versus forcing frequency normalized by the Maxwell time scale, i.e., τ_m/τ_f , for basaltic and silicic eruptions. Each of these phase lags, along with their uncertainties, may be projected onto the theoretical curve for the phase, which, in turn, identifies a range of values for the normalized frequency, τ_m/τ_f , and the normalized amplitude of the transfer function, $A_H(\omega) = (\Delta p_{crit}/\Delta p_f)/(\tau_f/\tau_m)$. Consequently the time lags determined from the data analysis constrain $\Delta p_{crit}/\Delta p_f \approx 0.8$ for silicic volcanism and $\Delta p_{crit}/\Delta p_f < 2 \times 10^{-2}$ for basaltic volcanism. In principle, with additional constraints on Δp_{crit} or Δp_f , values for either parameter may be obtained.

Glazner et al. [56] suggest that a plausible estimate for the mean ice thickness and lake depth in this region is around 300 m which corresponds to $\Delta p_f \approx 3$ MPa. Thus, from Figure 6.6, for silicic and basaltic volcanism, this loading constrains $\Delta p_{crit} \approx 3$

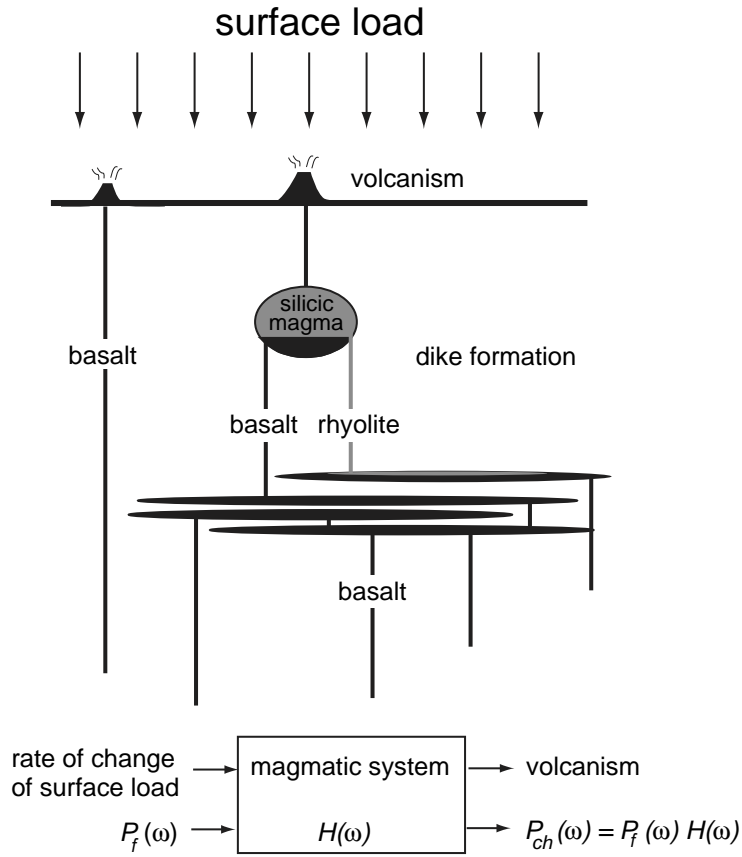


Figure 6.5. Conceptual model of the magmatic system envisioned for the Sierras. The system, $h(t)$, serves as a filter that is convolved with the input forcing pressure, $p_f(t)$, to produce the output magma chamber pressure, $p_{ch}(t)$. In the frequency domain, the convolution becomes spectral multiplication, where $P_{ch}(\omega) = P_f(\omega)H(\omega)$

MPa and $\Delta p_{crit} \ll 1$ MPa, respectively. For comparison, Jellinek and DePaolo [89] argue on the basis of the dynamical requirements for the formation and propagation of dikes to the surface that Δp_{crit} is in the range of 10-30 MPa for rhyolitic magmas and is likely $\ll 1$ MPa for basaltic magmas. However, Glazner et al. [56] indicate that the maximum ice thickness was about 1.5 km. If this estimate for ice thickness is more accurate then $\Delta p_{crit} \approx 15$ MPa and $\Delta p_{crit} \ll 1$ MPa may be more appropriate estimates for silicic and basaltic volcanism, respectively. The present analysis, based

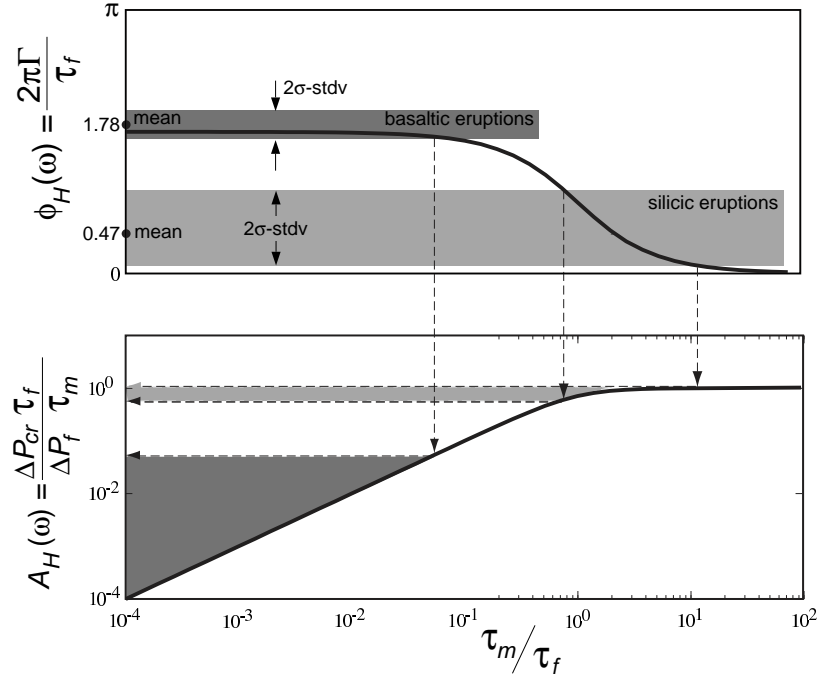


Figure 6.6. Phase lag (i.e., time lag) and amplitude normalized by the Maxwell time scale, τ_m , versus glacial forcing frequency, $1/\tau_f$, also normalized by τ_m . Shown are the phase lags for the basaltic and silicic time lags determined in Section 6.2.

on data, thus provides an additional independent constraint on Δp_{crit} .

Figure 6.6 also shows that the estimate for $\tau_f \approx 40$ kyr constrains the Maxwell time to $32 \leq \tau_m \leq 400$ kyr and $\tau_m < 2.4$ kyr for rhyolitic and basaltic volcanism, respectively. Taking $E = 10^{10}$ Pa in Eq. (6.4) to be typical for all rocks, these Maxwell times imply that the average effective wall rock viscosities governing silicic and basaltic volcanism are $10^{22} \leq \mu_{wr} \leq 10^{23}$ Pa·s and $\mu_{wr} < 8 \times 10^{20}$ Pa·s, respectively. Assuming that crustal rheology is thermally-activated [99] and that temperature increases monotonically with depth, these results are consistent with basaltic magmas originating at greater depths than silicic magmas (Figure 6.5). Geochemical and petrological observations suggest that, while rhyolite magmas may erupt from

depths of 5-8 km [3, 196], basaltic magmas appear to erupt from the base of the lithosphere [34]. Finally, these wall rock viscosities agree with Jellinek and DePaolo [89] who conclude that under most plausible conditions for silicic magma chambers in intracontinental settings, the dynamics governing dike formation are likely to lead to volcanism if $\mu_{wr} \geq 10^{20}$ Pa·s.

6.4 Conclusions

Magmatic and volcanic systems involve processes that operate over a wide range of time and length scales. In the example investigated here, glacial forcing at the kiloyear time scale appears to modulate volcanic eruption frequency and provides insight into crustal dynamics (e.g., the Maxwell time scale and wall rock viscosity). In particular, I propose that statistically significant anticorrelations exist between the rate of change of ice thickness (approximated by the derivative of the $\delta^{18}\text{O}$ time series) and the change in volcanic eruption frequency. The time lags between maxima and minima of the derivatives of glaciation and basaltic and silicic eruption frequency are about 11.3 ± 1.0 kyr and 3.0 ± 3.4 kyr, respectively. These results suggest a wall rock viscosity of $\mu_{wr} < 8 \times 10^{20}$ Pa·s and $10^{22} \leq \mu_{wr} \leq 10^{23}$ Pa·s for basaltic and silicic volcanism, respectively, which implies that basaltic magmas originate from greater depths than silic magmas.

Chapter 7

Conclusions

In the following I summarize the findings of this dissertation by providing the abstracts of the original publications (Sections 7.1, 7.2, and 7.3) or manuscripts in review (Sections 7.4 and 7.5).

7.1 Continuum percolation theory

In Chapter 2, I study continuum percolation of three-dimensional randomly oriented soft-core polyhedra (prisms). The prisms are biaxial or triaxial and range in aspect ratio over 6 orders of magnitude. Results for prisms are compared with studies for ellipsoids, rods, ellipses, and polygons and differences are explained using the concept of the average excluded volume, $\langle v_{ex} \rangle$. For large shape anisotropies I find close agreement between prisms and most of the above mentioned shapes for the critical total average excluded volume, $n_c \langle v_{ex} \rangle$, where n_c is the critical number density of objects at the percolation threshold. In the extreme oblate and prolate limits simulations yield $n_c \langle v_{ex} \rangle \approx 2.3$ and $n_c \langle v_{ex} \rangle \approx 1.3$, respectively. Cubes exhibit the lowest

shape anisotropy of prisms minimizing the importance of randomness in orientation. As a result, the maximum prism value, $n_c \langle v_{ex} \rangle \approx 2.79$, is reached for cubes, a value close to $n_c \langle v_{ex} \rangle = 2.8$ for the most equant shape, a sphere. Similarly, cubes yield a maximum critical object volume fraction of $\phi_c = 0.22$. ϕ_c decreases for more prolate and oblate prisms and reaches a linear relationship with respect to aspect ratio for aspect ratios greater than about 50. Curves of ϕ_c as a function of aspect ratio for prisms and ellipsoids are offset at low shape anisotropies but converge in the extreme oblate and prolate limits. The offset appears to be a function of the ratio of the normalized average excluded volume for ellipsoids over that for prisms, $R = \langle \overline{v_{ex}} \rangle_e / \langle \overline{v_{ex}} \rangle_p$. This ratio is at its minimum of $R = 0.758$ for spheres and cubes, where $\phi_{c(sphere)} = 0.2896$ may be related to $\phi_{c(cube)} = 0.22$ by $\phi_{c(cube)} = 1 - [1 - \phi_{c(sphere)}]^R = 0.23$. With respect to biaxial prisms, triaxial prisms show increased normalized average excluded volumes, $\langle \overline{v_{ex}} \rangle$, due to increased shape anisotropies, resulting in reduced values of ϕ_c . I confirm that $B_c = n_c \langle v_{ex} \rangle = 2C_c$ applies to prisms, where B_c and C_c are the average number of bonds per object and average number of connections per object, respectively.

7.2 Yield strength development in crystal-melt suspensions

In Chapter 3, I investigate the formation of a continuous crystal network in magmas and lavas. Network formation in crystal-melt suspensions can provide finite yield strength, τ_y , and can thus cause a change from Newtonian to Bingham rheology. The rheology of crystal-melt suspensions affects geological processes, such as ascent of magma through volcanic conduits, flow of lava across the Earth's surface, melt extrac-

tion from crystal mushes under compression, convection in magmatic bodies, or shear wave propagation through partial melting zones. Here, three-dimensional numerical models are used to investigate the onset of ‘static’ yield strength in a zero-shear environment. Crystals are positioned randomly in space and can be approximated as convex polyhedra of any shape, size, and orientation. I determine the critical crystal volume fraction, ϕ_c , at which a crystal network first forms. The value of ϕ_c is a function of object shape and orientation distribution, and decreases with increasing randomness in object orientation and increasing shape anisotropy. For example, while parallel-aligned convex objects yield $\phi_c = 0.29$, randomly oriented cubes exhibit a maximum ϕ_c of 0.22 as discussed in Chapter 2. Approximations of plagioclase crystals as randomly oriented elongated and flattened prisms (tablets) with aspect ratios between 1:4:16 and 1:1:2 yield $0.08 < \phi_c < 0.20$, respectively. The dependence of ϕ_c on particle orientation implies that the flow regime and resulting particle ordering may affect the onset of yield strength. ϕ_c in zero-shear environments is a lower bound for ϕ_c . Finally the average total excluded volume is used, within its limitation of being a “quasi-invariant” (Chapter 2), to develop a scaling relation between τ_y and ϕ for suspensions of different particle shapes.

7.3 Hydroseismicity

Groundwater recharge at Mt. Hood, Oregon, is dominated by spring snow melt which provides a natural large-amplitude and narrow-width pore-fluid pressure signal. Time delays between this seasonal groundwater recharge and seismicity triggered by groundwater recharge can thus be used to estimate large-scale hydraulic diffusivities and the state of stress in the crust. I approximate seasonal variations in groundwater recharge with discharge in runoff-dominated streams at high elevations. I interpolate

the time series of number of earthquakes, N , seismic moment, M_o , and stream discharge, Q , and determine cross correlation coefficients at equivalent frequency bands between Q and both N and M_o . I find statistically significant correlation coefficients at a mean time lag of about 151 days. This time lag and a mean earthquake depth of about 4.5 km are used in the solution to the pressure diffusion equation, under periodic (1 year) boundary conditions, to estimate a hydraulic diffusivity of $\kappa \approx 10^{-1} \text{ m}^2/\text{s}$, a hydraulic conductivity of about $K_h \approx 10^{-7} \text{ m/s}$, and a permeability of about $k \approx 10^{-15} \text{ m}^2$. Periodic boundary conditions also allow me to determine a critical pore-fluid pressure fraction, $P'/P_0 \approx 0.1$, of the applied near-surface pore-fluid pressure perturbation, $P_0 \approx 0.1 \text{ MPa}$, that has to be reached at the mean earthquake depth to cause hydroseismicity. The low magnitude of $P' \approx 0.01 \text{ MPa}$ is consistent with other studies that propose $0.01 \leq P' \leq 0.1 \text{ MPa}$ and suggests that the state of stress in the crust near Mt. Hood could be near critical for failure. Therefore, I conclude that, while earthquakes occur throughout the year at Mt. Hood, elevated seismicity levels along preexisting faults south of Mt. Hood during summer months are hydrologically induced by a reduction in effective stress.

7.4 Permeability-depth curve

Permeability is often considered the most important parameter in geological porous media flow, largely determining fluid fluxes. Here, I investigate the decrease in 1-dimensional permeability, k (in square meters), with depth, z (in kilometers), in the tectonically and volcanically active Oregon Cascades employing four different techniques. Each technique provides insight into the overall average permeability applicable to a different depth scale. Spring discharge models are used to infer shallow ($z < 0.1 \text{ km}$) horizontal permeability values. Coupled heat and groundwater flow

simulations provide vertical k for $z < 1$ km. Statistical investigations of the occurrences of earthquakes that are probably triggered by seasonal groundwater recharge yield vertical k for $z < 5$ km. Finally, considerations of magma intrusion rates and devolatilization of water from the magma provide estimates of vertical k for $z < 15$ km. For depths greater than about 0.8 km, my results agree with the power-law permeability-depth relationship, $k = 10^{-14} \text{ m}^2 (z/1 \text{ km})^{-3.2}$, suggested by Manning and Ingebritsen (Rev. Geophys., 1999) for continental crust in general. However, for shallower depths ($z \leq 0.8$ km) I propose an exponential relationship, $k = 5 \times 10^{-13} \text{ m}^2 \exp(-z/0.25 \text{ km})$, that both fits data better (at least for the Cascades) and allows for a finite permeability near the surface and no singularity at zero depth. In addition, the two suggested functions yield a relatively smooth transition at $z = 0.8$ km, where their permeabilities and their permeability gradients are similar. Permeability values inferred from the hydroseismicity model at Mt. Hood are about one order of magnitude larger than expected from the above $k(z)$ -relationship. However, higher permeabilities in this region may be consistent with advective heat transfer along active faults causing observed hot springs. The coupled heat and groundwater transfer models suggest mean background heat-flow values of about $H_b \approx 0.080$ to $H_b \approx 0.134 \text{ W/m}^2$ for the investigated region in the Oregon Cascades.

7.5 Glacier-induced volcanism

A comparison of time series of basaltic and silicic eruptions in eastern California over the last 400 kyr with the contemporaneous global record of glaciation suggests that this volcanism is influenced by the growth and retreat of glaciers occurring over periods of about 40 kyr. In addition, statistically significant cross correlations between eruption data and the first derivative of the glacial time series imply that

the temporal pattern of volcanism is influenced by the rate of change in ice volume. Moreover, calculated time lags for the effects of glacial unloading on basaltic and rhyolitic volcanism are distinctive and are 11.3 and 3.0 kyr, respectively. A theoretical model is developed to investigate whether the increase in eruption frequency following periods of glacial unloading is a response ultimately controlled by the dynamics of dike formation. Applying results from the time series analysis leads, in turn, to estimates for the critical magma chamber overpressure required for eruption as well as constraints on the average mechanical properties of the wall rocks governing dike propagation.

Appendix A

Appendix to Chapter 4: Hydroseismicity

A.1 Seismometer information

The following information about the short-period vertical-motion seismometers in the vicinity of Mt. Hood was provided by the Pacific Northwest Seismograph Network. The date-column refers to the seismometer installation date.

key	latitude (° ' ")	longitude (° ' ")	elevation (km)	date (mm/yy)
KMO	45 38 07.80	-123 29 22.20	0.975	09/82
SSO	44 51 21.60	-122 27 37.80	1.242	09/91
TDH	45 17 23.40	-121 47 25.20	1.541	09/82
VBE	45 03 37.20	-121 35 12.60	1.544	10/79
VCR	44 58 58.18	-120 59 17.35	1.015	08/83
VFP	45 19 05.00	-121 27 54.30	1.716	10/80
VG2	45 09 20.00	-122 16 15.00	0.823	09/85
VGB	45 30 56.40	-120 46 39.00	0.729	04/80
VLL	45 27 48.00	-121 40 45.00	1.195	10/80
VLM	45 32 18.60	-122 02 21.00	1.150	06/80
PGO	45 27 42.60	-122 27 11.50	0.253	06/82
AUG	45 44 10.00	-121 40 50.00	0.865	10/81
GUL	45 55 27.00	-121 35 44.00	1.189	07/86
MTM	46 01 31.80	-122 12 42.00	1.121	03/80

A.2 Box-Jenkins method

The stream discharge of Salmon River is predicted beyond its last measurement by employing a transfer function between Hood River and Salmon River. The transfer function is determined using a Box-Jenkins [21] method. In the case of a single input channel, X_t , investigated here, the output (or lag) channel, Y_t , can depend on both current ($t = 0$) and previous ($t < 0$) input, X_t , as well as on previous output, Y_t . Thus, input and output are related by

$$Y_t = \frac{\omega(B)}{\delta(B)} X_{t-b} + N_t, \quad (\text{A.1})$$

where

$$\frac{\omega(B)}{\delta(B)} = \frac{\omega_0 + \omega_1 B + \omega_2 B^2 + \dots + \omega_n B^\eta}{\delta_0 + \delta_1 B + \delta_2 B^2 + \dots + \delta_n B^\gamma} \quad (\text{A.2})$$

is the transfer function with coefficients ω and δ . Because coefficients in ω act on current and previous input and coefficients in γ act on previous output, they may be denoted as moving average (MA) and auto-regressive (AR) processes and the transfer function as a so-called ARMA model. In the previous equations, t is a time index, B is the backshift operator such that $B^b X_t = X_{t-b}$, η and γ are the number of delays for input and output, respectively, and N_t is noise assumed unrelated to the input. Therefore, if the noise, N_t , is neglected and (in my case) $\eta = 4$ and $\gamma = 1$ is selected then the output, Y_t , at time, t , is given by

$$\delta_0 Y_t = \delta_1 Y_{t-1} + \omega_0 X_t + \omega_1 X_{t-1} + \omega_2 X_{t-2} + \omega_3 X_{t-3} + \omega_4 X_{t-4}, \quad (\text{A.3})$$

where $\delta_0 = 1$ is commonly assumed (or else Eq. (A.3) is divided by δ_0). Therefore, in this example, the current output depends on one ($b = 1$) previous output (Salmon River discharge) as well as on the current ($b = 0$) and previous four ($1 \leq b \leq 4$) inputs (Hood River discharge).

A.3 Moving polynomial interpolation

The daily binned seismic data has to be interpolated so that continuous time series are obtained on which standard spectral analyses can be performed. I apply a moving polynomial interpolation, rather than convolution of the data with a Gaussian normal curve, so that no artificial frequency is introduced by a convolution kernel. In addition, the moving polynomial approach allows interpolation with low-order (≤ 5) polynomials while assuring that the data is optimally matched in a least squares sense. For all three series, Q , N , and M_o , the width of the moving window is $1/12^{\text{th}}$ of the total series length and the step width is $1/10^{\text{th}}$ of the window width. The polynomial coefficients, m_{LS} , are found using the standard least-squares solution from inverse

theory given as $m_{LS} = [G^T G]^{-1} G^T d$, where G is the (up to) 5th order polynomial model matrix and d is the data vector. Multiple interpolation values for a given time step result from the overlap of the moving window and are averaged.

A.4 Correlation coefficients

I determine auto ($f = g$) and cross ($f \neq g$) correlation coefficients for time series f and g as described in principal by Eqs. (4.3) and (4.4). In practice, correlation coefficients, ϕ_{fg} , for positive time lags, l , are calculated by

$$\phi_{fg}(l) = \frac{1}{M-l} \sum_{m=0}^{M-l-1} f_{m+l} g_m, \quad (\text{A.4})$$

where m and M are the index and the length of the (zero-padded) time series, respectively. Dividing by $(M-l)$ provides so-called unbiased cross correlations where the reduced overlap length of the series for large time lags is accounted for. Correlation coefficients are then normalized as described by Eq. (4.3).

I determine confidence intervals for the case where one of the two time series is assigned random phases for each frequency so that its auto-correlation is unaffected. Typically 500 iterations (each assigning new random phases for each frequency) of cross correlations, $\phi_{fg}(t)$, at lag t , are performed by spectral multiplication directly in the frequency domain as

$$\phi_{fg}(t) = F^{-1} \{ F\{f\} F^* \{g\} \}, \quad (\text{A.5})$$

where F , F^{-1} , and F^* denote the Fourier transform, its inverse, and its complex conjugate, respectively. The range of values that contain 90% of the data for a given time lag is the 90%-confidence interval for that time lag.

To reduce the effect of years with unusually high seismicity, moving cross correlation coefficients within overlapping subsections (windows) of the time series are also determined. Here, based on all windows that provide output for a given time lag, the mean coefficient per time lag is determined. Each window has to be short enough so that the years with dominant seismicity do not fall in all windows but large enough so that cross correlations are performed over several periods (I chose 3 years). Furthermore, the time lags of coefficients that are distinct from the confidence interval for random phase distributions, are used to calculate a mean and a standard deviation for the (positive) time lag around the first local maximum coefficient.

Appendix B

Appendix to Chapter 5: Permeability-depth curve

B.1 Definition of symbols

The following table provides definitions for symbols used in Chapter 5. Also shown are units and typical values used where appropriate.

Symbol	Units	Value	Definition
α	(m ² /N)	10^{-10}	vertical compressibility of bulk aquifer
β	(m ² /N)	4.8×10^{-10}	compressibility of water
b	(m)		thickness of aquifer or saturated zone
c_w	(J/kg/°C)	4180	specific heat of water
c_r	(J/kg/°C)	1000	specific heat of rock
d	(m)		magma intrusion depth
δ	(m)		characteristic depth scale (skin depth)
ϵ	(°C)		mean absolute temperature error
g	(m/s ²)	9.81	gravitational constant
H	(W/m ²)		heat-flow
h	(m)		hydraulic head
\mathbf{k}	(m ²)		permeability tensor
\mathbf{K}	(m/s)		hydraulic conductivity tensor
$\mathbf{\kappa}$	(m ² /s)		hydraulic diffusivity tensor
$\mathbf{\kappa}_m$	(m ² /s)		mixed thermal diffusivity (as scalar)
k_{T_w}	(W/m/°C)	0.6	thermal conductivity of water
k_{T_r}	(W/m/°C)	2	thermal conductivity of rock (as scalar)
L	(m)		length of aquifer or volcanic arc

Table is continued on next page.

Symbol	Units	Value	Definition
μ	(Pa·s)		dynamic viscosity
ν	(m ² /s)		kinematic viscosity
n	(–)	0.01	connected pore fraction
P	(Pa)		pressure
Ψ	(m/s)		precipitation rate
ψ	(s)		period
ϕ	(–)		weight fraction
Q	(m ³ /s)		volumetric flux
q	(m ² /s)		volumetric flux per unit width or length
ρ_w	(kg/m ³)	1000	density of water
ρ_r	(kg/m ³)	2700	density of rock
S_S	(1/m)		specific storage
S_Y	(–)		specific yield
T	(°C)		temperature
t	(s)		time
\mathcal{T}	(s)		diffusion time scale
\mathbf{u}	(m/s)		Darcy velocity vector
\mathbf{v}	(m/s)		interstitial or seepage velocity vector
W	(m)		width of aquifer or volcanic arc

Subscripts	Definition	Subscripts	Definition
e	elevation	s	(near) surface or spring
M	magma	T	thermal
m	mixed	w	water
p	pressure	$\mathbf{x} = (x, y)$	horizontal dimensions
r	rock or radial distance	z	vertical dimension
R	recharge		

B.2 Derivation of the equation for a $T(z)$ -profile with an exponential decrease in permeability

Substituting Eq. (5.10) into Eq. (5.14) yields

$$\frac{\gamma K_s}{\kappa_m R} (b - z) e^{-z/\delta} \frac{\partial T}{\partial z} = \frac{\partial^2 T}{\partial z^2}. \quad (\text{B.1})$$

In Eq. (B.1), set $A = (\gamma K_s)/(\kappa_m R)$, $D = \partial T/\partial z$, and $D' = \partial^2 T/\partial z^2$, so that it becomes

$$D' + A(z - b)e^{-z/\delta} D = 0, \quad (\text{B.2})$$

where the integration factor is now given as

$$D = \exp \left[\int A(z-b) e^{-z/\delta} dz \right] = \exp [Ae^{-z/\delta} (\delta b - \delta^2 - \delta z)] . \quad (\text{B.3})$$

Eq. (B.2) times the integration factor (Eq. B.3),

$$[D' + A(z-b)e^{-z/\delta} D] \exp [Ae^{-z/\delta} (\delta b - \delta^2 - \delta z)] = 0, \quad (\text{B.4})$$

is rewritten as

$$\frac{d}{dz} \{ D \exp [Ae^{-z/\delta} (\delta b - \delta^2 - \delta z)] \} = 0. \quad (\text{B.5})$$

Integration of Eq. (B.5) with respect to z results in

$$\frac{\partial T}{\partial z} \exp [Ae^{-z/\delta} (\delta b - \delta^2 - \delta z)] = c, \quad (\text{B.6})$$

where c is the integration constant and $D = \partial T / \partial z$ has been resubstituted. For the boundary condition

$$\frac{\partial T}{\partial z} = -\frac{q_b}{k_{Tr}} \quad \text{at } z = b \quad (\text{B.7})$$

and after resubstituting $A = (\gamma K_s) / (\kappa_m R)$, Eq. (B.6) becomes Eq. (5.15) which has to be integrated numerically to yield temperature as a function of depth, $T(z)$.

B.3 Derivation of the equation for a $T(z)$ -profile with constant hydraulic conductivity

Substituting Eq. (5.12) into Eq. (5.14) yields

$$\frac{\gamma K_s}{\kappa_m R} (b-z) \frac{\partial T}{\partial z} = \frac{\partial^2 T}{\partial z^2}. \quad (\text{B.8})$$

In Eq. (B.8), set $A = (\gamma K_s) / (\kappa_m R)$, $D = \partial T / \partial z$, and $D' = \partial^2 T / \partial z^2$, so that it becomes

$$D' + A(z-b)D = 0, \quad (\text{B.9})$$

where the integration factor is now given as

$$D = \exp \left[\int A(z-b) dz \right] = \exp \left(\frac{A}{2} z^2 - Abz \right). \quad (\text{B.10})$$

Eq. (B.9) times the integration factor (Eq. B.10),

$$[D' + A(z-b)D] \exp \left(\frac{A}{2} z^2 - Abz \right) = 0, \quad (\text{B.11})$$

is rewritten as

$$\frac{d}{dz} \left[D \exp \left(\frac{A}{2} z^2 - Abz \right) \right] = 0. \quad (\text{B.12})$$

Integration of Eq. (B.12) with respect to z results in

$$\frac{\partial T}{\partial z} = c \exp \left(Abz - \frac{A}{2} z^2 \right), \quad (\text{B.13})$$

where c is the integration constant and $D = \partial T / \partial z$ has been resubstituted. Applying the boundary condition

$$\frac{\partial T}{\partial z} = -\frac{q_b}{k_{T_r}} \quad \text{at } z = b \quad (\text{B.14})$$

to Eq. (B.13) yields

$$c = - \left(\frac{\partial T}{\partial z} \right)_b \exp \left(\frac{A}{2} b^2 - Ab^2 \right) \quad (\text{B.15})$$

Integrating Eq. (B.13) with respect to z and with the boundary condition $T(z = 0) = T_R$, where T_R is the recharge temperature at the surface, yields

$$T(z) = T_R + c \sqrt{\frac{\pi}{2A}} \exp \left(\frac{Ab^2}{2} \right) \operatorname{erfc} \left[(b - z) \sqrt{\frac{A}{2}} \right]. \quad (\text{B.16})$$

Here, c is given by Eq. (B.15) and erfc is the complimentary error function. Substituting Eq. (B.15) into Eq. (B.16) and resubstituting $A = (\gamma K_s) / (\kappa_m R)$ results in Eq. (5.16).

B.4 Finite difference method

Eqs. (5.21) and (5.22) as well as Darcy's law are approximated by replacing the continuous partial derivatives with finite differences. The grid points are regularly spaced at distances of Δr and Δz in horizontal, r , and vertical, z , directions, respectively. Hydraulic conductivity can be anisotropic and heterogeneous so that $K_r(r, z) \neq K_z(r, z)$.

The solution to the groundwater flow equation (5.21) is determined by iterative methods and is given in finite difference form with successive over/under relaxation by

$$h_{ij}^{m+1} = (1 - \omega) h_{ij}^m + \omega h_{ij}^{m+1}, \quad (\text{B.17})$$

where i and j are the grid indices in horizontal and vertical directions, respectively, $m+1$ and m indicate results from the current and the previous iteration, respectively, and ω is the relaxation factor. For $\omega = 1$, $\omega > 1$, and $0 < \omega < 1$ the current hydraulic

head, h_{ij}^{m+1} , is given by a standard Gauss-Seidel method, is over relaxed, and is under relaxed, respectively [199]. I apply the chain rule

$$\frac{\partial}{\partial w} \left(K_w \frac{\partial h}{\partial w} \right) = \frac{\partial K_w}{\partial w} \frac{\partial h}{\partial w} + K_w \frac{\partial^2 h}{\partial w^2} \quad (\text{B.18})$$

to Eq. (5.21), where $w = r$ and $w = z$ for the first and the third terms, respectively. Then, for any ω I compute the hydraulic head by

$$h_{ij}^{m+1} = \frac{A_r + \frac{K_{rij}}{(\Delta r)^2} (h_{i-1,j}^{m+1} + h_{i+1,j}^m) + R_{hr} + A_z + \frac{K_{zij}}{(\Delta z)^2} (h_{i,j-1}^{m+1} + h_{i,j+1}^m)}{2 \left(\frac{K_{rij}}{(\Delta r)^2} + \frac{K_{zij}}{(\Delta z)^2} \right)}, \quad (\text{B.19})$$

where

$$A_r = \left(\frac{K_{ri+1,j} - K_{ri-1,j}}{2\Delta r} \right) \left(\frac{h_{i+1,j}^m - h_{i-1,j}^{m+1}}{2\Delta r} \right), \quad (\text{B.20})$$

$$A_z = \left(\frac{K_{zi,j+1} - K_{zi,j-1}}{2\Delta z} \right) \left(\frac{h_{i,j+1}^m - h_{i,j-1}^{m+1}}{2\Delta z} \right), \quad (\text{B.21})$$

and

$$R_{hr} = \frac{K_{rij}}{r} \left(\frac{h_{i+1,j}^m - h_{i-1,j}^{m+1}}{2\Delta r} \right). \quad (\text{B.22})$$

Here, $r = i\Delta r$ is the radial distance from the central axis in the cylindrical coordinate system. For a 2D-cartesian coordinate system, $R_{hr} = 0$.

The solution to the heat advection-diffusion equation (5.22) is computed analogously to Eq. (B.17) where h_{ij}^{m+1} and h_{ij}^m are replaced with T_{ij}^{m+1} and T_{ij}^m , respectively. I determine the temperature field iteratively on a grid with horizontal, i , and vertical, j , indices and horizontal, Δr , and vertical, Δz , grid point spacing by

$$T_{ij}^{m+1} = \frac{1}{2\kappa_m} \left(\frac{\kappa_m(B + R_{Tr}) - \gamma q_{rij} C_r - \gamma q_{zij} C_z}{(\Delta r)^{-2} + (\Delta z)^{-2}} \right), \quad (\text{B.23})$$

where

$$B = \frac{T_{i-1,j}^{m+1} + T_{i+1,j}^m}{(\Delta r)^2} + \frac{T_{i,j-1}^{m+1} + T_{i,j+1}^m}{(\Delta z)^2}, \quad (\text{B.24})$$

$$C_r = \frac{T_{i+1,j}^m - T_{i-1,j}^{m+1}}{2\Delta r}, \quad (\text{B.25})$$

$$C_z = \frac{T_{i,j+1}^m - T_{i,j-1}^{m+1}}{2\Delta z}, \quad (\text{B.26})$$

and

$$R_{Tr} = \frac{1}{r} \left(\frac{T_{i+1,j}^m - T_{i-1,j}^{m+1}}{2\Delta r} \right). \quad (\text{B.27})$$

As before, $r = i\Delta r$ is the radial distance from the central axis and $R_{T_r} = 0$ for a 2D-cartesian coordinate system.

Darcy's law in 2D finite difference form is given here as

$$\begin{aligned} q_{r_{ij}} &= -K_{r_{ij}} \left(\frac{h_{i+1,j} - h_{i-1,j}}{2\Delta r} \right) \\ q_{z_{ij}} &= -K_{z_{ij}} \left(\frac{h_{i,j+1} - h_{i,j-1}}{2\Delta z} \right), \end{aligned} \quad (\text{B.28})$$

where all $q_{i,j}$ are based on results for $h_{i,j}$ after the final iteration and thus no iteration index, m , is given here.

B.5 Axisymmetric flow

In Eq. (5.21), the horizontal radial distance, r , from the vertical axis, z , is related to the horizontal x and y dimensions in a cartesian coordinate system by $r = \sqrt{x^2 + y^2}$. I assume that hydraulic conductivity is constant in all horizontal directions but possibly different from the vertical direction, i.e., $K_r = K_x = K_y \neq K_z$. Eq. (5.21) describes a regime with 3-dimensional axisymmetric groundwater flow (or hydraulic head diffusion) where all radial 2D cross sections through the central vertical axis, z , have identical hydraulic head distributions and are symmetric with respect to the z -axis (Figure B.1). Therefore, no hydraulic head gradient exists with respect to circumferential distance, c , i.e., $\partial h / \partial c = 0$. The only difference between Eq. (5.21) and a steady-state groundwater flow equation in a 2D-cartesian coordinate system is the extra middle term, $(K_r/r)(\partial h / \partial r)$, which accounts for the radially diverging geometry.

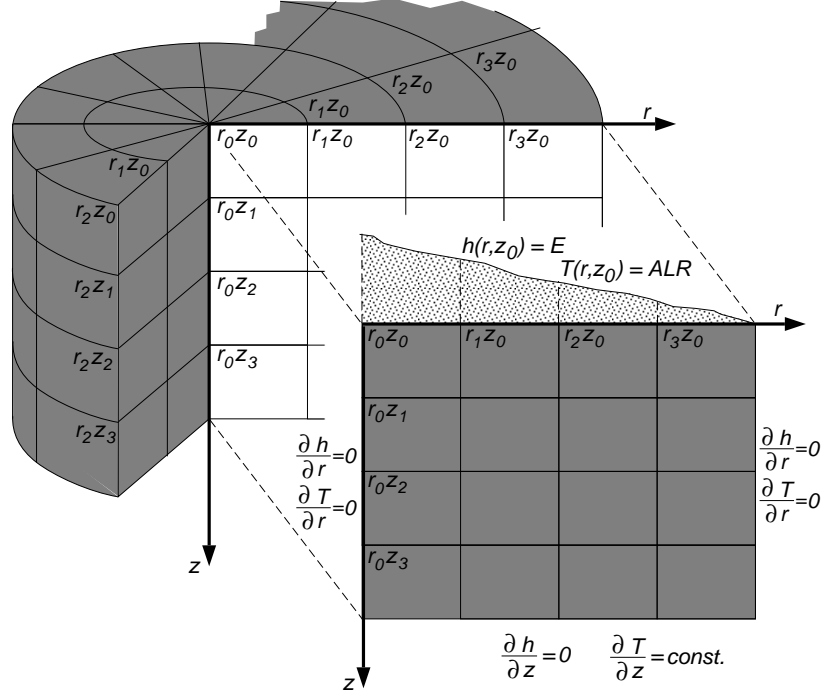


Figure B.1. Schematic illustration of the computational grid in cylindrical coordinates used for heat and groundwater transfer modeling. All cross sections through the central vertical axis, z , are identical and each cross section is symmetric with respect to the z -axis. Thus, while calculations are based on this 3D-cylindrical coordinate system, all information is given in the (pull-out) rectangle with coordinates $(0 \leq r \leq N_r, 0 \leq z \leq N_z)$, where N_r and N_z are the maximum number of grid points in the r - and z -direction, respectively. The symmetry axis, z , and the outer vertical boundary ($r = N_r$) are no-flow boundaries for both groundwater ($\partial h / \partial r = 0$) and heat ($\partial T / \partial r = 0$). The bottom boundary is a no-flow boundary for groundwater ($\partial h / \partial z = 0$) and a constant heat flux boundary ($\partial T / \partial z = \text{const.}$). Hydraulic head distribution at the surface, which is approximated as being horizontal, is given by mean radial elevation, E , and temperature is given by the mean adiabatic lapse rate, ALR .

Bibliography

- [1] H. Amit, V. Lyakhovsky, A. Katz, A. Starinsky, and A. Burg. Interpretation of spring recession curves. *Ground Water*, 40(5):543–551, 2002.
- [2] H.S. Carslaw and J.C. Jaeger. *Conduction of Heat in Solids*. Oxford Univ. Press, New York, 2nd edition, 1959.
- [3] A.T. Anderson, S. Newman, S.N. Williams, T.H. Druitt, C. Skirius, and E. Stolper. H₂O, CO₂, Cl, and gas in plinian and ash-flow Bishop rhyolite. *Geology*, 17(3):221–225, 1989.
- [4] L. Audin, J.-P. Avouac, M. Flouzat, and J.-L. Plantet. Fluid-driven seismicity in a stable tectonic context: The Remirmont fault zone, Vosges, France. *Geophys. Res. Lett.*, 29(6):art. no. 1091, 2002.
- [5] I. Balberg. “Universal” percolation-threshold limits in the continuum. *Phys. Rev. B*, 31(6):4053–4055, 1985.
- [6] I. Balberg. Excluded-volume explanation of Archie’s law. *Phys. Rev. B*, 33(5):3618–3620, 1986.
- [7] I. Balberg. Nonuniversal behavior of the cluster properties in continuum systems. *Phys. Rev. B*, 37(4):2391–2394, 1988.
- [8] I. Balberg, C.H. Anderson, S. Alexander, and N. Wagner. Excluded volume and its relation to the onset of percolation. *Phys. Rev. B*, 30(7):3933–3943, 1984.
- [9] I. Balberg, N. Binenbaum, and N. Wagner. Percolation thresholds. *Phys. Rev. Lett.*, 52(17):1465–1468, 1984.
- [10] H.A. Barnes and K. Walters. The yield strength myth. *Rheol. Acta*, 24(4):323–326, 1985.
- [11] G.A. Barth, M.C. Kleinrock, and R.T. Helz. The magma body at Kilauea Iki lava lake: Potential insights into mid-ocean ridge magma chambers. *J. Geophys. Res.*, 99:7199–7217, 1994.

- [12] J. Bear. *Dynamics of Fluids in Porous Media*. Dover, New York, 1988.
- [13] K. Becker and E. E. Davis. New evidence for age variation and scale effects of permeabilities of young oceanic crust from borehole thermal and pressure measurements. *Earth Planet. Sci. Lett.*, 210:499–508, May 2003.
- [14] K. Belitz and J.D. Bredehoeft. Hydrodynamics of the Denver basin - explanation of subnormal fluid pressures. *AAPG Bull.*, 72:1334–1359, 1988.
- [15] D.P. Bentz and E.J. Garboczi. Percolation of phases in a 3-dimensional cement paste microstructural model. *Cem. Concr. Res.*, 21(2–3):325–344, 1991.
- [16] D.D. Blackwell. Thermal results of the Santiam Pass 77-24 drill hole. In B.E. Hill, editor, *Geology and Geothermal Resources of the Santiam Pass Area of the Oregon Cascade Range, Deschutes, Jefferson, and Linn Counties, Oregon*, volume Open-File Report O-92-3, page 61. Oregon Department of Geology and Mineral Industries, 1992.
- [17] D.D. Blackwell and S.L. Baker. *Geology and Geothermal Resources of the Breitenbush-Austin Hot Springs Area, Clackamas and Marion Counties, Oregon*, volume O-88-5, chapter Thermal Analysis of the Austin and Breitenbush geothermal systems, Western Cascades, Oregon, pages 47–62. Oregon Department of Geology and Mineral Industries Open-File Report, 1988.
- [18] D.D. Blackwell, R.G. Bowen, D.A. Hull, J. Riccio, and J.L. Steele. Heat-flow, arc volcanism, and subduction in northern Oregon. *J. Geophys. Res.*, 87(10):8735–8754, 1982.
- [19] D.D. Blackwell, J.L. Steele, S. Kelley, and M.A. Korosec. Heat-flow in the state of Washington and thermal conditions in the Cascade range. *J. Geophys. Res.*, 95(B12):19,495–19,516, 1990.
- [20] W. Borchard and M. Lechtenfeld. Time dependent properties of thermoreversible gels. *Mater. Res. Innov.*, 4(5–6):381–387, 2001.
- [21] G.E.P. Box, G.M. Jenkins, and G.C. Reinsel. *Time Series Analysis : Forecasting and Control*. Prentice Hall, Englewood Cliffs, N. J., 1994.
- [22] W.F. Brace. Permeability of crystalline and argillaceous rocks. *Int. J. Rock. Mech. Min.*, 17(5):241–251, 1980.
- [23] W.F. Brace. Permeability of crystalline rocks - new in situ measurements. *J. Geophys. Res.*, 89(6):4327–4330, 1984.
- [24] R.N. Bracewell. *The Fourier Transform and its Applications*. McGraw Hill, New York, 3rd edition, 2000.

- [25] J. Bredehoeft and I.S. Papadopoulos. Rates of vertical groundwater movement estimated from the Earth's thermal profile. *Water Resour. Res.*, 1(2):325–328, 1965.
- [26] K.V. Cashman, C. Thornber, and J.P. Kauahikaua. Cooling and crystallization of lava in open channels, and the transition of pahoehoe lava to 'a'a. *Bull. Volcanol.*, 61(5):306–323, 1999.
- [27] A. Celzard, E. McRae, C. Deleuze, M. Dufort, G. Furdin, and J.F. Marêché. Critical concentration in percolating systems containing a high-aspect-ratio filler. *Phys. Rev. B*, 53(10):6209–6214, 1996.
- [28] C. Clauser. Permeability of crystalline rocks. *Eos Trans. AGU*, 73:233–238, 1992.
- [29] C. Clauser, E. Griesshaber, and H.J. Neugebauer. Decoupled thermal and mantle helium anomalies: Implications for the transport regime in continental rift zones. *J. Geophys. Res.*, 107:doi:10.1029/2001JB000675, 2002.
- [30] J.K. Costain, G.A. Bollinger, and J.A. Speer. Hydroseismicity: A hypothesis for the role of water in the generation of intraplate seismicity. *Seismological Res. Lett.*, 58:41–64, 1987.
- [31] J.-R. de Dreuzy, P. Davy, and O. Bour. Percolation parameter and percolation-threshold estimates for three-dimensional random ellipses with widely scattered distributions of eccentricity and size. *Phys. Rev. E*, 62(5):5948–5952, 2000.
- [32] J.G. de la Torre, S.E. Harding, and B. Carrasco. Calculation of NMR relaxation, covolume, and scattering-related properties of bead models using solpro computer program. *Eur. Biophys. J.*, 28(2):119–132, 1999.
- [33] D. Deming. Regional permeability estimates from investigations of coupled heat and groundwater flow, north slope of Alaska. *J. Geophys. Res.*, 98:16,271–16,286, 1993.
- [34] D.J. DePaolo and E.E. Daley. Neodymium isotopes in basalts of the southwest Basin and Range and lithospheric thinning during continental extension. *Chem. Geol.*, 169(1–2):157–185, 2000.
- [35] D.B. Dingwell. Volcanic dilemma: Flow or blow? *Science*, 273:1054–1055, 1996.
- [36] P.A. Domenico and V.V. Palciauskas. Theoretical analysis of forced convective heat transfer in regional ground-water flow. *Geol. Soc. Am. Bull.*, 84:3803–3814, 1973.
- [37] P.A. Domenico and F.W. Schwartz. *Physical and Chemical Hydrogeology*. John Wiley and Sons, New York, 2nd edition, 1998.

- [38] D.S. Dreger, H. Tkalčić, and M. Johnston. Dilational processes accompanying earthquakes in the Long Valley caldera. *Science*, 288(5463):122–125, 2000.
- [39] A. Drory. Theory of continuum percolation. I. general formalism. *Phys. Rev. E*, 54(6):5992–6002, 1996.
- [40] A. Drory. Theory of continuum percolation. II. mean field theory. *Phys. Rev. E*, 54(6):6003–6013, 1996.
- [41] A. Drory, B. Berkowitz, G. Parisi, and I. Balberg. Theory of continuum percolation. III. low-density expansion. *Phys. Rev. E*, 56(2):1379–1395, 1997.
- [42] A. Einstein. Eine neue Bestimmung der Moleküldimensionen. *Ann. Phys.*, 19:289–306, 1906.
- [43] C.W. Fetter. *Applied Hydrogeology*. Prentice Hall, Upper Saddle River, N. J., 3rd edition, 1994.
- [44] A. Fizazi, J. Moulton, K. Pakbaz, S.D. Rughooputh, P. Smith, and A.J. Heeger. Percolation on a self-assembled network-decoration of polyethylene gels with conducting polymer. *Phys. Rev. Lett.*, 64(18):2180–2183, 1990.
- [45] F. Jh. Fontaine, M. Rabinowicz, and J. Boulègue. Permeability changes due to mineral diagenesis in fractured crust: Implications for hydrothermal circulation at mid-ocean ridges. *Earth Planet. Sci. Lett.*, 184:407–425, 2001.
- [46] C. Forster and L. Smith. The influence of groundwater flow on thermal regimes in mountainous terrain: A model study. *J. Geophys. Res.*, 94:9439–9451, 1989.
- [47] R.A. Freeze and J.A. Cherry. *Groundwater*. Prentice Hall, Englewood Cliffs, N. J., 1979.
- [48] A.F. Gangi. Variation of whole and fractured porous rock permeability with confining pressure. *Int. J. Rock Mech. Min.*, 15(5):249–257, 1978.
- [49] S.S. Gao, P.G. Silver, A.T. Linde, and I.S. Sacks. Annual modulation of triggered seismicity following the 1992 Landers earthquake in California. *Nature*, 406:500–504, 2000.
- [50] E.J. Garboczi, K.A. Snyder, J.F. Douglas, and M.F. Thorpe. Geometrical percolation threshold of overlapping ellipsoids. *Phys. Rev. E*, 52:819–828, 1995.
- [51] E.J. Garboczi, M.F. Thorpe, M. DeVries, and A.R. Day. Universal conductivity curve for a plane containing random holes. *Phys. Rev. A*, 43(12):6473–6482, 1991.
- [52] S. Ge. Estimation of groundwater velocity in localized fracture zones from well temperature profiles. *J. Volcanol. Geotherm. Res.*, 84:93–101, 1998.

- [53] L.N. Germanovich, R.P. Lowell, and D.K. Astakhov. Stress-dependent permeability and the formation of seafloor event plumes. *J. Geophys. Res.*, 105:8341–8354, 2000.
- [54] L.N. Germanovich, R.P. Lowell, and D.K. Astakhov. Temperature-dependent permeability and bifurcations in hydrothermal flow. *J. Geophys. Res.*, 106:473–495, 2001.
- [55] A.F. Glazner. Volcanic eruption ages in eastern California. unpublished.
- [56] A.F. Glazner, C.R. Manley, and J.S. Marron. Fire or ice: Anticorrelation of volcanism and glaciation in California over the past 800,000 years. *Geophys. Res. Lett.*, 26(12):1759–1762, 1999.
- [57] U. Grigull, J. Straub, and P. Schiebener. *Steam Tables in SI-Units*. Springer-Verlag, Berlin, New York, 3rd edition, 1990.
- [58] T.L. Grove, S.W. Parman, S.A. Bowring, R.C. Price, and M.B. Baker. The role of an H₂O-rich fluid component in the generation of primitive basaltic andesites and andesites from the Mt. Shasta region, N. California. *Contrib. Mineral. Petr.*, 142(4):375–396, 2002.
- [59] Y. Guéguen, Chelidze T, and M. Le Ravalec. Microstructures, percolation thresholds, and rock physical properties. *Tectonophysics*, 279:23–35, 1997.
- [60] H.K. Gupta. *Reservoir-Induced Earthquakes*. Elsevier Science, New York, 1992.
- [61] S.W. Haan and R. Zwanzig. Series expansion in a continuum percolation problem. *J. Phys. A*, 10:1547–1555, 1977.
- [62] F.R. Hall. Base-flow recessions - a review. *Water Resour. Res.*, 4(5):973–983, 1968.
- [63] K. Hall. Rapid deglaciation as an initiator of volcanic activity - an hypothesis. *Earth Surf. Proc. Land*, 7(1):45–51, 1982.
- [64] W.L. Hamilton. Tidal cycles of volcanic eruptions - fortnightly to 19 yearly periods. *J. Geophys. Res.*, 78(17):3363–3375, 1973.
- [65] R.A. Harris. Introduction to special section: Stress triggers, stress shadows, and implications for seismic hazards. *J. Geophys. Res.*, 103(B10):24,347–24,358, 1998.
- [66] D.O. Hayba and S.E. Ingebritsen. Multiphase groundwater flow near cooling plutons. *J. Geophys. Res.*, 102:12,235–12,252, 1997.
- [67] J.H. Healy, W.W. Rubey, D.T. Griggs, and C.B. Raleigh. The Denver earthquakes. *Science*, 161:1301–1310, 1968.

- [68] K. Heki. Snow load and seasonal variation of earthquake occurrence in Japan. *Earth Planet. Sci. Lett.*, 207:159–164, 2003.
- [69] W. Hildreth. Gradients in silicic magma chambers: Implications for lithospheric magmatism. *J. Geophys. Res.*, 86:10,153–10,192, 1981.
- [70] S. Hoover, K.V. Cashman, and M. Manga. The yield strength of subliquidus basalts - experimental results. *J. Volc. and Geoth. Res.*, 107:1–18, 2001.
- [71] P.A. Hsieh and J.D. Bredehoeft. A reservoir analysis of the Denver earthquakes: A case of induced seismicity. *J. Geophys. Res.*, 86:903–920, 1981.
- [72] K.W. Hudnut, L. Seeber, and J. Pacheco. Cross-fault triggering in the November 1987 Superstition Hills earthquake sequence, southern California. *Geophys. Res. Lett.*, 16:199–202, 1989.
- [73] E. Huenges, J. Erzinger, J. Kück, B. Engeser, and W. Kessels. The permeable crust: Geohydraulic properties down to 9101 m depth. *J. Geophys. Res.*, 102:18,255–18,265, 1997.
- [74] H.E. Huppert. The intrusion of fluid mechanics into geology. *J. Fluid Mech.*, 173:557–594, 1986.
- [75] H.E. Huppert, R.S.J. Sparks, J.S. Turner, and N.T. Arndt. Emplacement and cooling of komatiite lavas. *Nature*, 309(5963):19–22, 1984.
- [76] S. Hurwitz, S.E. Ingebritsen, and M.L. Sorey. Episodic thermal perturbations associated with groundwater flow: An example from Kilauea volcano, Hawaii. *J. Geophys. Res.*, 107:art. no. 2297, 2002.
- [77] S. Hurwitz, K.L. Kipp, S.E. Ingebritsen, and M.E. Reid. Groundwater flow, heat transport, and water table position within volcanic edifices: Implications for volcanic processes in the Cascade range. *J. Geophys. Res.*, 108:doi:10.1029/2003JB002565, 2003.
- [78] O. Huseby, J.-F. Thovert, and P. M. Adler. Geometry and topology of fracture systems. *J. Phys. A*, 30:1415–1444, 1997.
- [79] Y. Hyun, S.P. Neuman, V.V. Vesselinov, W.A. Illman, D.M. Tartakovsky, and V. Di Federico. Theoretical interpretation of a pronounced permeability scale effect in unsaturated fractured tuff. *Water Resour. Res.*, 38(6):art. no. 1092, 2002.
- [80] S.E. Ingebritsen, R.H. Mariner, D.E. Cassidy, L.D. Shepherd, T.S. Presser, M.K. Pringle, and L.D. White. Heat-flow and water-chemistry data from the Cascade range and adjacent areas in north-central Oregon. *Open-File Report 88-702*, page 205, 1988.

- [81] S.E. Ingebritsen, R.H. Mariner, and D.R. Sherrod. Hydrothermal systems of the Cascades range, north-central Oregon. *U.S. Geological Survey Professional Paper 1044-L*, 1994.
- [82] S.E. Ingebritsen and W.E. Sanford. *Groundwater in Geologic Processes*. Cambridge University Press, Cambridge, New York, 1st edition, 1998.
- [83] S.E. Ingebritsen, M.A. Scholl, and D.R. Sherrod. Heat flow from four new research drill holes in the western Cascades, Oregon, U.S.A. *Geothermics*, 22(3):151–163, 1993.
- [84] S.E. Ingebritsen, D.R. Sherrod, and R.H. Mariner. Heat-flow and hydrothermal circulation in the Cascade range, north-central Oregon. *Science*, 243(4897):1458–1462, 1989.
- [85] S.E. Ingebritsen, D.R. Sherrod, and R.H. Mariner. Rates and patterns of groundwater flow in the Cascade range volcanic arc, and the effect of subsurface temperatures. *J. Geophys. Res.*, 97:4599–4627, 1992.
- [86] A. Isihara. Determination of molecular shape by osmotic measurement. *J. Chem. Phys.*, 18(11):1446–1449, 1950.
- [87] E.W. James, M. Manga, T.P. Rose, and G.B. Hudson. The use of temperature and the isotopes of O, H, C, and noble gases to determine the pattern and spatial extent of groundwater flow. *J. Hydrol.*, 237:100–112, 2000.
- [88] D.J. Jeffrey and A. Acrivos. The rheological properties of suspensions of rigid particles. *AIChE J.*, 22:417–432, 1976.
- [89] A.M. Jellinek and D.J. DePaolo. A model for the origin of large silicic magma chambers: Precursors of caldera-forming eruptions. *Bull. of Volcanol.*, published online, May 6, 2003.
- [90] M.-J. Jiménez and M. García-Fernández. Occurrence of shallow earthquakes following periods of intense rainfall in Tenerife, Canary Islands. *J. Volc. and Geoth. Res.*, 103:463–468, 2000.
- [91] M.J. Johnston and F.J. Mauk. Earth tides and triggering of eruptions from Mt. Stromboli, Italy. *Nature*, 239(5370):266, 1972.
- [92] J. Jones and S.D. Malone. Mount Hood earthquake activity: Volcanic or tectonic origins? *Eos. Trans. AGU*, 83(47), *Fall Meet. Suppl.*, Abstract S12A-1179, 2002.
- [93] M. Jull and D. McKenzie. The effect of deglaciation on mantle melting beneath Iceland. *J. Geophys. Res.*, 101(B10):21,815–21,828, 1996.

- [94] J. Kasahara. Tides, earthquakes, and volcanoes. *Science*, 297:348–349, 2002.
- [95] R.C. Kerr and J.R. Lister. The effects of shape on crystal settling and on the rheology of magmas. *J. Geology*, 99:457–467, 1991.
- [96] R.C. Kerr and J.R. Lister. Comment on ”on the relationship between dike width and magma viscosity” by Yutaka Wada. *J. Geophys. Res.*, 100:15,541, 1995.
- [97] L. Keszthelyi and R. Denlinger. The initial cooling of pahoehoe flow lobes. *Bull. Volcanol.*, 58(1):5–18, 1996.
- [98] G.C.P. King, R.S. Stein, and J. Lin. Static stress changes and the triggering of earthquakes. *Bull. Seismol. Soc. Am.*, 84:935–953, 1994.
- [99] S.H. Kirby. Rock mechanics observations pertinent to the rheology of the continental lithosphere and the localization of strain along shear zones. *Tectonophysics*, 119(1–4):1–27, 1985.
- [100] V. Léonardi, F. Arthaud, A. Tovmassian, and A. Karakhanian. Tectonic and seismic conditions for changes in spring discharge along the Garni right lateral strike slip fault (Armenian upland). *Geodinamica Acta*, 11(2-3):85–103, 1998.
- [101] R.G. Larson. *The Structure and Rheology of Complex Fluids*. Oxford University Press, Oxford, New York, 1999.
- [102] T. Lay and T.C. Wallace. *Modern Global Seismology*. Academic Press, San Diego, 1995.
- [103] A.-M. Lejeune and P. Richet. Rheology of crystal-bearing silicate melts: An experimental study at high viscosities. *J. Geophys. Res.*, 100:4215–4229, 1995.
- [104] D.A. Lockner and N.M. Beeler. Premonitory slip and tidal triggering of earthquakes. *J. Geophys. Res.*, 104(B9):20,133–20,151, 1999.
- [105] C.D. Lorenz and R.M. Ziff. Precise determination of the critical percolation threshold for the three-dimensional ”swiss cheese” model using a growth algorithm. *J. Chem. Phys.*, 114(8):3659–3661, 2001.
- [106] M. Maasland. *Drainage of Agricultural Lands, in Soil Anisotropy and Soil Drainage*, pages 216–285. Am. Soc. of Agron., Madison, Wis., 1957.
- [107] J. Maclean, M. Jull, D. McKenzie, L. Slater, and K. Gronvold. The link between volcanism and deglaciation in Iceland. *Geochem. Geophys. Geosys.*, 3:art. no. 1062, 2002.
- [108] M. Manga. Hydrology of spring-dominated streams in the Oregon Cascades. *Water Resour. Res.*, 32:2435–2439, 1996.

- [109] M. Manga. A model for discharge in spring-dominated streams and implications for the transmissivity and recharge of Quaternary volcanics in the Oregon Cascades. *Water Resour. Res.*, 33:1813–1822, 1997.
- [110] M. Manga. Orientation distribution of microlites in obsidian. *J. Volc. and Geoth. Res.*, 86:107–115, 1998.
- [111] M. Manga. On the timescales characterizing groundwater discharge at springs. *J. Hydrol.*, 219:56–69, 1999.
- [112] M. Manga. Using springs to study groundwater flow and active geologic processes. *Annu. Rev. Earth Planet. Sci.*, 29:201–28, 2001.
- [113] C.E. Manning and S.E. Ingebritsen. Missing mineral zones in contact metamorphosed basalts. *Amer. J. Sci.*, 293:894–938, 1993.
- [114] C.E. Manning and S.E. Ingebritsen. Permeability of the continental crust: Implications of geothermal data and metamorphic systems. *Rev. Geophys.*, 37:127–150, 1999.
- [115] B. Marsh. On the crystallinity, probability of occurrence, and rheology of lava and magma. *Contrib. Min. Pet.*, 78:85–98, 1981.
- [116] B.D. Marsh. On the mechanism of igneous diapirism, stoping, and zone melting. *Am. J. Sci.*, 282:808–855, 1982.
- [117] L.G. Mastin. Explosive tephra emissions at Mount St.-Helens, 1989-1991 - the violent escape of magmatic gas following storms. *Geol. Soc. Am. Bull.*, 106(2):175–185, 1994.
- [118] F.J. Mauk and M.J. Johnston. Triggering of volcanic eruptions by Earth tides. *J. Geophys. Res.*, 78(17):3356–3362, 1973.
- [119] W.J. McGuire, R.J. Howarth, C.R. Firth, A.R. Solow, A.D. Pullen, S.J. Saunders, I.S. Stewart, and C. VitaFinzi. Correlation between rate of sea-level change and frequency of explosive volcanism in the Mediterranean. *Nature*, 389(6650):473–476, 1997.
- [120] A. McIntyre, W.F. Ruddiman, K. Karlin, and A.C. Mix. Surface water response of the equatorial Atlantic ocean to orbital forcing. *Paleoceanography*, 4:19–55, 1989.
- [121] S.R. McNutt and R.J. Beavan. Eruptions of Pavlof volcano and their possible modulation by ocean load and tectonic stresses. *J. Geophys. Res.*, 92(B11):11,509–11,523, 1987.

- [122] O.E. Meinzer. Large springs in the United States. *U.S. Geol. Surv. Water Supp. Pap.*, 557:94, 1927.
- [123] C. Morrow, D. Lockner, S. Hickman, M. Rusanov, and T. Rockel. Effects of lithology and depth on the permeability of core samples from the Kola and KTB drill holes. *J. Geophys. Res.*, 99:7263–7274, 1994.
- [124] S. H. Munson-McGee. Estimation of the critical concentration in an anisotropic percolation network. *Phys. Rev. B*, 43(4):3331–3336, 1991.
- [125] M.D. Murphy, R.S.J. Sparks, J. Barclay, M.R. Carroll, and T.S. Brewer. Remobilization of andesite magma by intrusion of mafic magma at the Soufriere Hills volcano, Montserrat, West Indies. *J. Petrol.*, 41:21–42, 2000.
- [126] M. Nakada and H. Yokose. Ice-age as a trigger of active Quaternary volcanism and tectonism. *Tectonophysics*, 212(3–4):321–329, 1992.
- [127] M. Nathenson. Springs on and in the vicinity of Mount Hood, Oregon. *USGS Open-File Report*, in review, 2003.
- [128] J. Neuberg. External modulation of volcanic activity. *Geophys. J. Int.*, 142(1):232–240, 2000.
- [129] L.W. Nichol, P.D. Jeffrey, and D.J. Winzor. Molecular covolumes of sphere and ellipsoid of revolution combinations. *J. Phys. Chem.*, 80(6):648–649, 1976.
- [130] K. Nicholson. *Geothermal Fluids: Chemistry and Exploration Techniques*. Springer-Verlag, Berlin, Heidelberg, 1993.
- [131] G.M. Nielson. Scattered data modeling. *IEEE Comput. Graph.*, 13(1):60–70, 1993.
- [132] D. Norton and J.E. Knight. Transport phenomena in hydrothermal systems: Cooling plutons. *Amer. J. Science*, 277:937–981, 1977.
- [133] A. Nur and J.R. Booker. Aftershocks caused by pore fluid flow? *Science*, 175:885–887, 1972.
- [134] H. Ogasawara, K. Fujimori, N. Koizumi, N. Hirano, S. Fujiwara, S. Otsuka, S. Nakao, K. Nishigami, K. Taniguchi, Y. Iio, R. Nishida, K. Oike, and Y. Tanaka. Microseismicity induced by heavy rainfall around flooded vertical ore veins. *PAGEOPH*, 159:91–109, 2002.
- [135] L. Onsager. The effects of shapes on the interactions of colloidal particles. *Ann. N.Y. Acad. Sci.*, 51:627–659, 1949.
- [136] D. Patriarche, M.C. Castro, and P. Goblet. Manuscript in preparation, 2003.

- [137] A.P. Philipse. The random contact equation and its implications for (colloidal) rods in packings, suspensions, and anisotropic powders. *Langmuir*, 12:1127–1133, 1996.
- [138] O.M. Phillips. *Flow and Reactions in Permeable Rocks*. Cambridge University Press, Cambridge, New York, 1991.
- [139] A.R. Philpotts and L. D. Dickson. The formation of plagioclase chains during convective transfer in basaltic magma. *Nature*, 406:59–61, 2000.
- [140] A.R. Philpotts, J. Shi, and C. Brustman. Role of plagioclase crystal chains in the differentiation of partly crystallized basaltic magma. *Nature*, 395(6700):343–346, 1998.
- [141] G.E. Pike and C.H. Seager. Percolation and conductivity: A computer study. I. *Phys. Rev. B*, 10(4):1421–1434, 1974.
- [142] H. Pinkerton and R.J. Stevenson. Methods of determining the rheological properties of magmas at sub-liquidus temperatures. *J. Volc. and Geoth. Res.*, 56:108–120, 1992.
- [143] H.N. Pollack, S.J. Hurter, and J.R. Johnson. Heat-flow from the Earth’s interior - analysis of the global data set. *Rev. Geophys.*, 31(3):267–280, 1993.
- [144] C.B. Raleigh, J.H. Healy, and J.D. Bredehoeft. Faulting and crustal stress at Rangely, Colorado, in Flow and Fracture of Rocks. *Geophys. Monogr. Ser.*, 16:275–284, 1972.
- [145] C.B. Raleigh, J.H. Healy, and J.D. Bredehoeft. An experiment in earthquake control at Rangely, Colorado. *Science*, 191:1230–1237, 1976.
- [146] M.R. Rampino and S. Self. Can rapid climate change cause volcanic eruptions? *Science*, 106(4420):826–829, 1979.
- [147] J. Renner, B. Evans, and G. Hirth. On the rheologically critical melt fraction. *Earth Planet. Sci. Lett.*, 181:585–594, 2000.
- [148] C. E. Renshaw. Sample bias and the scaling of hydraulic conductivity in fractured rock. *Geophys. Res. Lett.*, 25:121–124, January 1998.
- [149] E. Roeloffs. Poroelastic techniques in the study of earthquake-related hydrologic phenomena. *Adv. Geophys.*, 37:135–195, 1996.
- [150] E. A. Roeloffs. Fault stability changes induced beneath a reservoir with cyclic variations in water level. *J. Geophys. Res.*, 93:2107–2124, 1988.

- [151] S. Rojstaczer and S. Wolf. Permeability changes associated with large earthquakes - an example from Loma-Prieta, California. *Geology*, 20(3):211–214, 1992.
- [152] R. Roscoe. Suspensions. In *Flow Properties of Disperse Systems*. J.J. Hermans, North Holland, Amsterdam, Netherlands, 1953.
- [153] P. Roth, N. Pavoni, and N. Deichmann. Seismotectonics of the eastern Swiss Alps and evidence for precipitation-induced variations of seismic activity. *Tectonophysics*, 207:183–197, 1992.
- [154] C.W. Rovey. Digital simulation of the scale effect in hydraulic conductivity. *Hydrogeology Journal*, 6(2):216–225, 1998.
- [155] F.J. Ryerson, H.C. Weed, and A.J. Piwinski. Rheology of subliquidus magmas, 1, picritic compositions. *J. Geophys. Res.*, 93:3421–3436, 1988.
- [156] M.O. Saar. The relationship between permeability, porosity and microstructure in vesicular basalts. Master’s thesis, University of Oregon, 1998.
- [157] M.O. Saar and M. Manga. Permeability-porosity relationship in vesicular basalts. *Geophys. Res. Lett.*, 26(1):111–114, 1999.
- [158] M.O. Saar and M. Manga. Continuum percolation for randomly oriented soft-core prisms. *Phys. Rev. E*, 65(5):art. no. 056131, 2002.
- [159] M.O. Saar and M. Manga. Seismicity induced by seasonal groundwater recharge at Mt. Hood, Oregon. *Earth Planet. Sci. Lett.*, 214:605–618, 2003.
- [160] M.O. Saar, M. Manga, K.V. Cashman, and S. Fremouw. Numerical models of the onset of yield strength in crystal- melt suspensions. *Earth Planet. Sci. Lett.*, 187:367–379, 2001.
- [161] M. Sahimi and S. Arabi. Mechanics of disorderd solids II. *Phys. Rev. B*, 47:703–712, 1993.
- [162] X. Sánchez-Vila, J. Carrera, and J.P. Girardi. Scale effects in transmissivity. *Journal of Hydrology*, 183:1–22, 1996.
- [163] P. Segall. Stress and subsidence resulting from subsurface fluid withdrawal in the epicentral region of the 1983 Coalinga earthquake. *J. Geophys. Res.*, 90:6801–6816, 1985.
- [164] P. Segall. Earthquakes triggered by fluid extraction. *Geology*, 17(10):942–946, 1989.
- [165] Spatial Climate Analysis Service. Average annual precipitation of Oregon. Online, 2002.

- [166] N.J. Shackleton. Oxygen isotopes, ice volume and sea-level. *Quaternary Sci. Rev.*, 6(3–4):183–190, 1987.
- [167] K.S. Shante and S. Kirkpatrick. An introduction to percolation theory. *Adv. Phys.*, 20:325–367, 1971.
- [168] H.R. Shaw. Comments on viscosity, crystal settling, and convection in granitic magmas. *Am. J. Sci.*, 263:120–152, 1965.
- [169] K. Shimazaki and T. Nakata. Time-predictable recurrence model for large earthquakes. *Geophys. Res. Lett.*, 7(4):279–282, 1980.
- [170] V.M. Shmonov, V.M. Vitiovtova, A.V. Zharikov, and A.A. Grafchikov. Permeability of the continental crust: Implications of experimental data. *J. Geochem. Explor.*, 78–79:697–699, 2003.
- [171] V.M. Shmonov, V.M. Vitovtova, A.V. Zharikov, and A.A. Grafchikov. Fluid permeability of the continental crust: Estimation from experimental data. *Geochem. Int.*, 40, Suppl. 1:S3–S13, 2002.
- [172] G.E. Sigvaldason, K. Annertz, and M. Nilsson. Effect of glacier loading/deloading on volcanism - postglacial volcanic production-rate of the Dynjufjoll area, central Iceland. *B. Volcanol.*, 54(5):385–392, 1992.
- [173] D.W. Simpson, W.S. Leith, and C.H. Scholz. Two types of reservoir-induced seismicity. *Bull. Seismol. Soc. Am.*, 78:2025–2040, 1988.
- [174] K.P. Singh and J.B. Stall. Derivation of base flow recession curves and parameters. *Water Resour. Res.*, 7(2):292–303, 1971.
- [175] T.W. Sisson and G.D. Layne. H₂O in basalt and basaltic andesite glass inclusions from 4 subduction-related volcanos. *Earth Planet. Sci. Lett.*, 117:619–635, 1993.
- [176] A.S. Skal and B.I. Shklovskii. Influence of the impurity concentration on the hopping conduction in semiconductors. *Sov. Phys. Semicond.*, 7(8):1058–1061, 1974.
- [177] L. Slater, M. Jull, D. McKenzie, and K. Gronvold. Deglaciation effects on mantle melting under Iceland: Results from the northern volcanic zone. *Earth Planet. Sci. Lett.*, 164(1–2):151–164, 1998.
- [178] L. Smith and D.S. Chapman. On the thermal effects of groundwater flow. *J. Geophys. Res.*, 88:593–608, 1983.
- [179] M.L. Sorey. Measurement of vertical groundwater velocity from temperature profiles in wells. *Water Resour. Res.*, 7(4):963–970, 1971.

- [180] R.S.J. Sparks. Triggering of volcanic eruptions by Earth tides. *Nature*, 290(5806):448–448, 1981.
- [181] D. Stauffer and A. Aharony. *Introduction to Percolation Theory*. Taylor and Francis, London, Washington D.C., 1992.
- [182] D.J. Stein and F.J. Spera. Rheology and microstructure of magmatic emulsions: Theory and experiments. *J. Volcanol. Geotherm. Res.*, 49:157–174, 1992.
- [183] R.S. Stein. The role of stress transfer in earthquake occurrence. *Nature*, 402:605–609, 1999.
- [184] R.S. Stein, G.C.P. King, and J. Lin. Change in failure stress on the southern San Andreas fault system caused by the 1992 magnitude = 7.4 Landers earthquake. *Science*, 258:1328–1332, 1992.
- [185] R.S. Stein, G.C.P. King, and J. Lin. Stress triggering of the 1994 M = 6.7 Northridge, California, earthquake by its predecessors. *Science*, 265:1432–1435, 1994.
- [186] L.M. Tallaksen. A review of baseflow recession analysis. *J. Hydrol.*, 165:349–370, 1995.
- [187] P. Talwani and S. Acree. Pore pressure diffusion and the mechanism of reservoir-induced seismicity. *PAGEOPH*, 122:947–965, 1984/85.
- [188] S. Tanaka, M. Ohtake, and H. Sato. Spatio-temporal variation of the tidal triggering effect on earthquake occurrence associated with the 1982 South Tonga earthquake of M_w 7.5. *Geophys. Res. Lett.*, 29(16):art. no. 1756, 2002.
- [189] S. Timoshenko and J.N. Goodier. *Theory of Elasticity*. McGraw Hill, New York, 1970.
- [190] J. Townend and M.D. Zoback. How faulting keeps the crust strong. *Geology*, 28(5):399–402, 2000.
- [191] D.L. Turcotte. Self-organized criticality. *Rep. Prog. Phys.*, 62:1377–1429, 1999.
- [192] D.L. Turcotte and G. Schubert. *Geodynamics*. Cambridge University Press, Cambridge, New York, 2nd edition, 2002.
- [193] J.S. Turner, H.E. Huppert, and R.S.J. Sparks. Komatiites II; experimental and theoretical investigations of post-emplacement cooling and crystallization. *J. Petrol.*, 27(2):397–437, 1986.
- [194] Y. Wada. Magma flow directions inferred from preferred orientations of phynocrysts in a composite feeder dike, Mikaye-Jima, Japan. *J. Volcanol. Geotherm. Res.*, 49:119–126, 1992.

- [195] Y. Wada. On the relationship between dike width and magma viscosity. *J. Geophys. Res.*, 99:17,743–17,755, 1994.
- [196] P.J. Wallace, A.T. Anderson, and A.M. Davis. Quantification of pre-eruptive exsolved gas contents in silicic magmas. *Nature*, 377(6550):612–616, 1995.
- [197] P.C. Wallmann, G.A. Mahood, and D.D. Pollard. Mechanical models for correlation of ring-fracture eruptions at Pantelleria, strait of Sicily, with glacial sea-level drawdown. *B. Volcanol.*, 50(5):327–339, 1988.
- [198] H.F. Wang. *Theory of Linear Poroelasticity*. Princeton University Press, Princeton, 2000.
- [199] H.F. Wang and M.P. Anderson. *Introduction to Groundwater Modeling : Finite Difference and Finite Element Methods*. Academic Press, San Francisco, 1982.
- [200] C.S. Weaver, R.D. Norris, and C. Trisler-Jonientz. Results of seismological monitoring in the Cascades range 1962-1989: Earthquakes, eruptions, avalanches, and other curiosities. *Geosci. Can.*, 17:158–162, 1990.
- [201] W.S.D. Wilcock. Tidal triggering of micro earthquakes on the Juan de Fuca ridge. *Geophys. Res. Lett.*, 28(20):3999–4002, 2001.
- [202] C.R. Wildemuth and M.C. Williams. Viscosity of suspensions modeled with a shear-dependent maximum packing fraction. *Rheol. Acta*, 23:627–635, 1984.
- [203] C.R. Wildemuth and M.C. Williams. A new interpretation of viscosity and yield stress in dense slurries: Coal and other irregular particles. *Rheol. Acta*, 24:75–91, 1985.
- [204] C.F. Williams and T.N. Narasimhan. Hydrogeologic constraints on heat-flow along the San-Andreas fault - a testing of hypotheses. *Earth Planet. Sci. Lett.*, 92(2):131–143, 1989.
- [205] L.W. Wolf, C.A. Rowe, and R.B. Horner. Periodic seismicity near Mt. Ogden on the Alaska - British Columbia border: A case for hydrologically triggered earthquakes? *Bull. Seismol. Soc. Am.*, 87:1473–1483, 1997.
- [206] A.D. Woodbury and L. Smith. Simultaneous inversion of hydrogeologic and thermal data: 2. incorporation of thermal data. *Water Resour. Res.*, 24(3):356–372, 1988.
- [207] A.D. Woodbury, L. Smith, and W.S. Dunbar. Simultaneous inversion of hydrogeologic and thermal data: 1. theory and application using hydraulic head data. *Water Resour. Res.*, 23(8):1586–1606, 1987.

- [208] T.L. Wright and R.T. Okamura. Cooling and crystallization of tholeiitic basalt, 1965 Makaopuhi lava lake, Hawai'i. *U.S. Geological Survey Prof. Paper 1004*, page 77, 1977.
- [209] J.Y. Yi and G.M. Choi. Percolation behavior of conductor-insulator composites with varying aspect ratio of conductive fiber. *J. Electroceram.*, 3(4):361–369, 1999.
- [210] Z.Q. Zhou, F. Tunman, G. Luo, and P.H.T. Uhlherr. Yield stress and maximum packing fraction of concentrated suspensions. *Rheol. Acta*, 34:544–561, 1995.
- [211] G. Zimmermann, H. Burkhardt, and L. Engelhard. Scale dependence of hydraulic and structural parameters in the crystalline rock of the KTB. *Pure and Appl. Geophys.*, 160:1067–1085, 2003.
- [212] M.D. Zoback and J.H. Healy. Friction, faulting, and in-situ stress. *Ann. Geophys.*, 2:689–698, 1984.
- [213] M.D. Zoback and J.C. Zinke. Production-induced normal faulting in the Valhall and Ekofisk oil fields. *Pure and Appl. Geophys.*, 159(1–3):403–420, 2002.